DYNAMIC TEMPERATURE ESTIMATION OF POWER ELECTRONICS SYSTEMS

BY

PAMELA JOSEPH TANNOUS

THESIS

Submitted in partial fulfillment of the requirements
for the degree of Master of Science in Mechanical Engineering
in the Graduate College of the
University of Illinois at Urbana-Champaign, 2017

Urbana, Illinois

Adviser:

Professor Andrew Alleyne

Abstract

This thesis proposes a method for accurate temperature estimation of thermally-aware power electronics systems. The duality between electrical systems and thermal systems was considered for thermal modeling. High dimensional thermal models present a challenge for online estimation. RC (resistor-capacitor) circuits that create a tradeoff between accuracy and complexity were used to simulate the dynamic thermal behavior of power electronics. The complexity of the thermal network was further reduced by applying a structure-preserving model order reduction technique. The reduced order thermal model was an RC circuit with fewer capacitors. Preserving the physical correspondence between the reduced order model and the physical system allows the user to use the reduced order thermal model in the sensor placement optimization process. The accuracy of the thermal estimates can be easily increased by increasing the number of sensors in the system. However, a large number of sensors increases the cost and complexity of the system. It might also interfere with the circuit design and create packaging problems. An optimal number and optimal placement of temperature sensors was found. The optimal sensor placement problem was solved by maximizing the trace of observability Gramian. The optimal number of temperature sensors was based on the state estimation error obtained from a Kalman filter. The dynamic thermal behavior of the power electronics systems was represented by a linear state space model by applying the conservation of energy principle. Therefore, assuming Gaussian noise, it is well-known that a Kalman filter is an optimal estimator for such systems. A continuous-discrete Kalman filter was used to estimate the dynamic thermal behavior of power electronics systems using an optimal number of temperature sensors placed at optimal locations. The proposed method was applied on 2-D and 3-D power electronics systems. Theoretical results were validated experimentally using IR thermal imaging and thermocouples. It was shown that the proposed method can accurately

reconstruct the dynamic temperature profile of power electronics systems using a small number of temperature sensors.

To my family, friends, and teachers.

Acknowledgements

First, I would like to thank my advisor, Dr. Andrew Alleyne, for his invaluable guidance and encouragement during the last two years. Without him, this work would not have been possible. He helped me become a better researcher. I am very honored to have the opportunity to learn more from him as I work for a Ph.D. under his guidance.

I would also like to thank my parents for letting me pursue my dreams in life. They believed in me and taught me how to work hard. I would not have been able to make it this far without their continual love and support.

I should also thank the Alleyne Research Group (ARG) for making my graduate school experience enjoyable. I would especially like to thank Justin, Matt, Herschel, Bryan, Malia, Ashley, Oyouna, Nate, Spencer, Xavier, Sarah, Spencer, and Sunny. I learned a lot from working with them.

Finally, I want to aknowledge the support of the Engineering Research Center (ERC) for Power Optimization of Electro-Thermal Systems (POETS). I feel so lucky to be part of this multidisciplinary research center that gave me the opportunity to work with extraordinary people from different disciplines and different institutions.

Table of Contents

List of Figures

List of Tables

Nomenclature

C	Thermal capacitance
ρ	Density
c	Specific heat capacity
v	Volume
R_{cond}	Conduction resistance
L	Length
K	Thermal conductivity
A_c	Cross-sectional area
R_{conv}	Convection resistance
h	Convective heat transfer coefficient
A_s	Surface area
$K_{in-plane}$	In-plane effective thermal conductivity
t	Thickness
$R_{t,0}$	Overall effective resistance
η_0	Overall efficiency of an array of fins
A_t	Total surface area of an extended surface
N	Number of fins
A_f	Surface area of a single fin
η_f	Efficiency of a single fin
A_b	Surface area of the exposed part of the base of an extended surface

l_c	Corrected length of a fin
T	Temperature
q	Net heat flow
x	State vector
u	Input vector
d	Disturbance vector
Q_s	Heat input
i	Index
j	Index
y	Output vector
$\hat{x}$	State estimate vector
$\hat{y}$	Output estimate vector
η_t	Moment of a linear system at the expansion point
G	Transfer function
$\hat{G}$	Reduced order transfer function
π	Stationary distribution of the Markov chain
$P(t)$	Markov chain transition matrix
e	State estimation error
L	Observer gain
Ω	Observability matrix
H	Mapping from true states to observed states
$v(m)$	Sensor noise
R_k	Covariance matrix
$\hat{x}_m^-$	A priori at instant m
$\hat{x}_m^+$	A posteriori at instant m
$\phi(t_m, t_{m-1})$	State transition matrix
K_m	Kalman gain matrix

$W_{o,linear}$	Linear observability Gramian
C_o	Condition number
$C_{multilayered}$	Effective thermal capacitance of a multilayered structure
T_a	Ambient temperature
Q_{conv}	Convective heat transfer

Chapter 1
Introduction

Power electronics systems are used for the conversion and control of electric power. Rectifiers are used to convert electric power from AC to DC. Inverters are used to convert electric power from DC to AC. Also, DC-DC converters can be used to control the voltage magnitude. AC-AC converters can be used to change the magnitude and frequency of the voltage. Power electronics have a wide range of applicability. They are used in industrial applications, transportation, domestic applications, telecommunication, power transmission, etc. Also, power electronics systems operate in a wide power range. For example, less than 1 W converters are found in portable equipments. 10-1000 W converters are found in computers. kW to MW converters are found in variable-speed motor drives. And 1000 MW converters are found in energy transmission applications [1].

However, power electronics systems are not ideal. They have dissipative elements, i.e. resistors. The nonideal behavior of power electronics is manifested as power loss converted into heat. The amount of heat dissipated into the system is related to the amount of power converted in the power electronics system. Furthermore, the new trend in the field of power electronics is the increase of power density. Smaller devices are used to convert higher power levels. Therefore, the amount of heat dissipated in these systems increases and creates localized hotspots that might lead to the failure of the power electronics system.

This thesis proposes a method for accurate dynamic thermal estimation of power electronics systems. A dynamic thermal estimation scheme composed of dynamic thermal modeling, model order reduction, sensor optimization, and filtering will be presented. The

method is applied on a heterogeneous highly-complex thermally coupled power electronics system.

1.1 Motivation

With the emerging trend of increasing the power density of power electronics comes the limitation of the power dissipation in the system. Power dissipation is transformed into heat in the power electronics systems. Therefore, the increase of power dissipation leads to an increase in temperature [2] that has negative effects on the performance and lifetime of the components operating in the power electronics system. Also, higher temperature increases the cooling cost which is a major problem in the current power electronics field [2]–[7].

Dynamic thermal management (DTM) was proven to be an effective solution to control the temperature of power electronics by guaranteeing that the temperature of the hotspots in the system will not violate a specific threshold. However, this technique typically relies on thermal measurements obtained from on-board sensors. Therefore, accurate temperature readings of the system are essential for a successful DTM [8]–[10].

Power electronics systems that estimate their own temperature to apply thermal management techniques, possibly by reducing their power flow, are known by thermally-aware power electronics [6]. Increasing the power density becomes safer in this new breed of power electronics systems since the availability of the accurate dynamic temperature profiles in these systems activates the DTM at the right time.

Accurate thermal readings can be obtained easily by increasing the number of sensors in the system. However, a large number of sensors influences the reliability and packaging of the power electronics system, increases its cost, and interferes with its circuit design [8]. Furthermore, the locations of the temperature sensors in the system affect the accuracy of the estimated parameters. Placing temperature sensors at random locations might lead to large thermal estimation errors. Therefore, finding the optimal number and optimal placement of temperature sensors is an essential task for the success of the dynamic thermal estimation process.

The objective of this research is to obtain an accurate estimation of the spatial dynamic thermal profile of thermally-aware power electronics systems using the smallest number of

temperature sensors in the system. Current power electronics systems do not have the ability to extract their dynamic spatial temperature distribution. Some work has been done on temperature estimation of a single chip [8]. However, the method proposed in this thesis provides a methodology for accurate thermal estimation of highly complex and heterogeneous systems using an online model-based estimator and compact thermal models.

In practice, some power electronics systems are open to the ambient atmosphere. Convective heat transfer in these systems happens directly between the components of the system and the ambient atmosphere. Those systems are treated as 2-dimensional (2-D) systems in this work since it is assumed that there is conduction only along the x and y directions in the plane of the system. Therefore, the dynamic thermal behavior of these systems is simulated using 2-dimensional thermal models.

In some other cases, the power electronics systems are enclosed by a heat sink that enhances heat transfer by convection from the system to the environment. In this case, convective heat transfer happens between the heat sink and the ambient atmosphere, i.e. there is no direct convective heat transfer between the components of the system and the ambient atmosphere. Heat is transferred by conduction from the components of the power electronics systems to the heat sink in the z-direction. Furthermore, there is conductive heat transfer along the x and y directions in the plane of the power electronics system. Therefore, enclosed power electronics systems will be treated as 3-dimensional (3-D) systems in this work because there is conduction along 3 dimensions in the system. The dynamic thermal behavior of these systems is simulated using 3-dimensional thermal models.

1.2 Thesis organization

The rest of this thesis is organized as follows. Chapter 2 describes the thermal network modeling procedure used in this work to simulate the dynamic thermal behavior of power electronics systems. In Chapter 3, a brief literature review of some well-known model order reduction techniques is presented. Also, the algorithm of the structure-preserving aggregation-based model order reduction technique used in this work to reduce the complexity, i.e. number of states, of the dynamic thermal models of power electronics systems is presented. In Chapter 4, a brief review of some well-known filters is presented. The continuous-discrete Kalman

filter used in this work to estimate the dynamic thermal behavior of power electronics systems is presented in some detail. In addition, the analysis used to find the optimal number and optimal placement of temperature sensors is presented in this chapter. In Chapter 5, the 2-dimensional dynamic thermal profile of an actual inverter is estimated using the proposed method. In Chapter 6, the 3-dimensional dynamic thermal profile of an inverter enclosed with a heat sink is estimated. The summary of research contributions and future work are presented in Chapter 7.

Chapter 2
Network Modeling

2.1 RC modeling

The dynamic physical systems of interest have temporally and spatially varying temperature profiles. Detailed modeling of thermal interaction in these systems results in high dimensional complex models that are inappropriate for estimation and control design purposes. The appropriate modeling approach needs to balance complexity versus accuracy. The thermal models should to be simple enough for on-line implementation and detailed enough to simulate the dynamic thermal behavior of the systems at an acceptable level of accuracy. Also, the number of powerful analysis tools drops significantly for non-linear systems compared to linear systems [11] leading to a strong preference for linear models. Therefore, the physical systems analyzed were approximated by lumped parameter models by deriving an equivalent thermal circuit [7]. Collecting these models results in a directed connected graph of linear systems. Model order reduction techniques can be used to further reduce the dimension of the lumped parameters models making them more suitable for estimation and control purposes.

The first step towards getting an accurate temperature estimation of thermally-aware power electronics systems is to create a thermal model that provides an accurate representation of the dynamic thermal behavior of the system. In order to account for all the thermal effects in the system in full detail, numerical thermal analysis methods such as the finite element method must be used in the modeling procedure. However, these techniques result in complex high-dimensional models that are not suitable for estimation and control design purposes. Therefore, a tradeoff between accuracy and complexity must be done in order to obtain a

thermal model that generates the dynamic thermal behavior of the system at an acceptable level of accuracy with low computational efforts [3].

As shown in the literature, a resistor-capacitor (RC) thermal model can successfully simulate the spatial dynamic temperature distribution of the system with a reasonable accuracy and complexity tradeoff [3], [10], [12]–[14]. Also, another advantage of RC thermal models is that they have a physical correspondence with the physical system. In other words, each capacitor in the RC thermal model represents the thermal capacitance of a specific part of the physical system. RC thermal models are created by considering the similarity between an electric circuit and a thermal circuit since current and heat flow are described with the same differential equations. This similarity converts the heat conduction problem into an electric problem where the voltage in the RC circuit represents the temperature in a thermal problem, the current represents the heat transfer or the power flow, and the electrical resistances represent the thermal resistances. The capacitors used in the RC model simulate the transient behavior of the system by modeling the thermal lag that occurs before the temperature of the system reaches a steady state value following a step change in the heat input. The thermal-electrical analogy is shown in table 2.1

Table 2.1 Thermal-electric analogy used to model resistor-capacitor thermal models.

	THERMAL	ELECTRICAL
THROUGH VARIABLE	heat transfer rate, q watts	current, I amps
ACROSS VARIABLE	Temperature, T degrees C	voltage, v volts
DISSIPATION ELEMENT	thermal resistance, R_{th} degC/watt	electrical resistance, R_{el} ohms
STORAGE ELEMENT	Thermal capacitance, C_{th} joules/degC	electrical capacitance, C_{el} farads

The heat conduction problem can be solved as a 1 dimensional (1-D) problem, 2 dimensional (2-D) problem, or 3 dimensional (3-D) problem [15]. For a 1-D heat conduction problem, the system is divided into blocks along just one direction. It is assumed that conduction occurs along just one direction in the system. The blocks are connected to each other through a thermal resistance that represents conduction resistance along that direction in the system. For a 2-D heat conduction problem, the system is considered as a plate that is divided into pixels along its width and length with an assigned capacitor to each one of these elements and assigned resistors that connect each capacitor to one other in the x and y directions. In this system, it is assumed that conduction occurs along 2 directions in the system. For a 3-D heat conduction problem, the system is divided into small cubes, or voxels, with assigned resistors and capacitors that account for the conduction along three dimensions. The 1-D, 2-D, and 3-D RC thermal models will be explained in more details in the next subsections.

2.1.1 1-D RC thermal models

Dynamic thermal estimation requires computationally efficient thermal models. The desired thermal models should simulate the offline dynamic thermal behavior of the power electronics system using a small number of states. In a 1-D RC thermal model, it is assumed that there is conduction only along the x direction in the system. It can also be assumed that there is convective heat transfer from the system to the environment. In order to design a 1-D RC thermal model, the system is discretized along its length into pixels. Each pixel is represented by a capacitor in the RC thermal model. Each capacitor represents the ability of the corresponding part of the system to store heat in it. Adjacent capacitors are connected to each other through conduction resistances. Since the temperature in a thermal model is represented by the voltage in an electric model, the ambient temperature is represented by a voltage source in the RC thermal model. Each capacitor in the RC thermal model is connected to the voltage source through a resistor that represents the convective heat transfer resistance from that specific part of the system to the ambient atmosphere. Figure 2.1 shows an example of the discretization and the modeling of a 1-D RC thermal model. The system was discretized into 2 pixels. Each pixel was represented by a capacitor in the RC thermal model. R_{cd} represents the conduction resistance along the x direction between the two pixels. Q represents a heat

source. It was shown in table 2.1 that the heat flow in a thermal system is represented by the current in an electric system. Therefore, the heat source Q that exists in the first pixel of the physical system is represented by the current source connected to C_1 in the RC thermal model. Each of the capacitors is connected to the voltage source through a R_{cv} that represents the convection resistance from that part of the system to the ambient atmosphere. The voltage source represents the ambient atmosphere. Therefore, it can be seen that there is a physical correspondence between the RC thermal model and the physical system. Each capacitor in the RC thermal model represents the heat storage capacitance of a specific part of the physical system. This physical correspondence between the RC thermal models and the physical systems is a feature of the 3 versions of the RC thermal models, i.e. 1-D, 2-D, and 3-D RC thermal models.

It should be noted that the type of heat transfer from a surface of a system depends on whether that surface is a free surface or a connected surface. A free surface experiences convective heat transfer to the ambient atmosphere. A connected surface experiences conductive heat transfer to the surface connected to it as shown in Figure 2.2. Therefore, spatially adjacent pixels will be connected through conduction resistances. And every pixel that is exposed to the ambient atmosphere will be connected to a voltage source through a convection resistance.

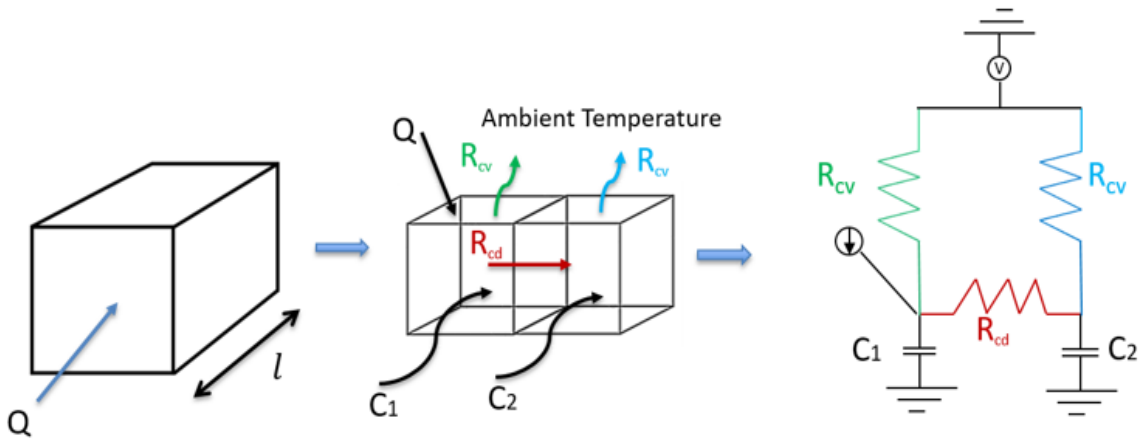

Figure 2.1 An example of a 1-D RC thermal model that was discretized into 2 pixels. Conduction was assumed along the x direction only.

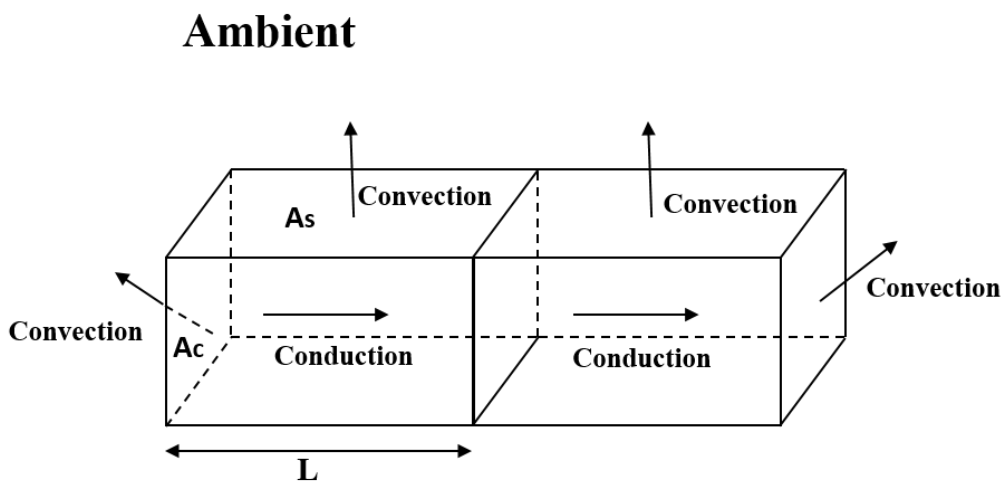

Figure 2.2 Heat transfer modes from a system with 2 functional elements.

The thermal capacitance is a function of the density of the material ρ, the specific heat capacity of the material c, and the volume of the corresponding part of the system v. The thermal capacitance is given by

$$C = \rho cv. \tag{2.1}$$

The conduction resistance is a function of the length through which the heat is conducted L, the thermal conductivity of the material K, and the cross-sectional area through which the heat is conducted A_c. The conduction resistance is given by

$$R_{cond} = \frac{L}{KA_c}. \tag{2.2}$$

The convection resistance is a function of the heat transfer coefficient h, and the surface area from which the heat is transferred to the ambient atmosphere A_s. The convection resistance is given by

$$R_{conv} = \frac{1}{hA_s}. \tag{2.3}$$

In general, printed circuit boards of power electronics are composed of several layers of varied materials. If the system is composed of multiple layers of different materials, it is

convenient to treat the multilayered structure as a homogeneous material and use an in-plane effective thermal conductivity to calculate the conduction resistance R_{cond}. The in-plane effective thermal conductivity is given by

$$K_{in-plane} = \frac{\sum_{i=1}^{N} K_i t_i}{\sum_{i=1}^{N} t_i}, \tag{2.4}$$

where k_i is the thermal conductivity of a specific layer, t_i is the thickness of the corresponding layer, N and is the total number of layers. The effective thermal capacitance of the multilayered structure is the sum of the thermal capacitance (2.1) of each layer

$$C = \sum_{i=1}^{N} C_i. \tag{2.5}$$

2.1.2 2-D RC thermal models

2-D RC thermal models account for conduction along the x and y directions in the plane of the system in addition to the convective heat transfer from the system to the ambient atmosphere. 2-D RC thermal models are used to simulate the dynamic thermal behavior of the power electronics systems that are open to the ambient atmosphere. In other words, 2-D RC thermal models can be used to simulate the dynamic thermal behavior of power electronics systems that are not enclosed by a heat sink and do not experience conductive heat transfer along the z direction. In these systems, convective heat transfer occurs directly between the components of the system and the environment. The first step in designing a RC thermal model is to discretize the system into pixels. For a 2-D RC thermal model, the system is discretized along its width and length into pixels or nodes. To reduce the complexity of the thermal model, the level of granularity chosen can be done at the level of the functional elements [3]. Therefore, each functional block in the power electronics system, i.e. the inverter, is represented by a single node and assigned a capacitor in the 2-D RC thermal model. The resulting RC model is characterized by a spatial correspondence with the physical system. Each capacitor in the RC model refers to a specific functional block in the physical system. The heat generated from the functional blocks is modeled as current sources connected to the corresponding capacitors in the 2-D RC model. The convective heat transfer from each

functional block or each part of the system to the ambient atmosphere is represented in the 2-D RC thermal model by a resistor that connects each capacitor of a free surface to the ambient atmosphere. The ambient atmosphere is represented in the 2-D RC model by a voltage source that allows the user to specify the specific ambient temperature that the system is subjected to. Figure 2.3 shows an example of a 2-D RC circuit for a system divided into 4 elements. The heat generated in the first functional element was modeled by the current source connected to the first capacitor. R12 and R34 represent the conduction resistance along the x direction. R24 and R13 represent the conduction resistance along the y direction. Rc1, Rc2, Rc3, and Rc4 represent the convection resistance between every pixel and the ambient atmosphere. The thermal capacitances, the conduction resistances, and the convection resistances are found using (2.1), (2.2), and (2.3).

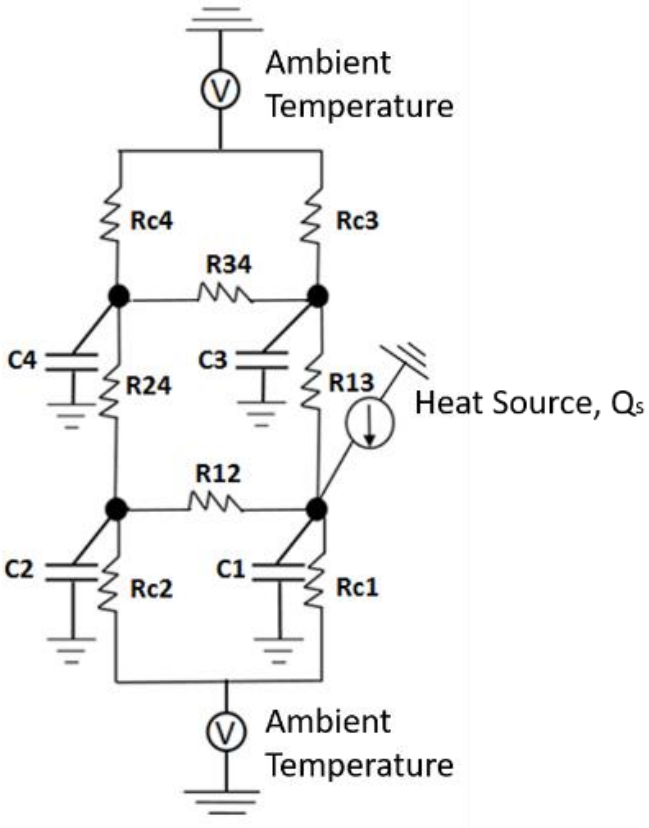

Figure 2.3 Example of a 2-D RC thermal model that was partitioned into 4 pixels.

2.1.3 3-D RC thermal models

Some power electronics systems are enclosed with heat sinks. Since the convection resistance is inversely proportional to the surface area from which the heat is transferred to the atmosphere, increasing that surface area decreases the convection resistance and hence enhances the heat transfer by convection from the system to the atmosphere. Therefore, heat sinks enhance the convective heat transfer from the power electronics system to the ambient temperature by increasing the surface area of the system exposed to the ambient temperature. In the case of enclosed power electronics systems, there is no direct convective heat transfer between the components of the system and the ambient atmosphere. In these systems, the components of the system experience conductive heat transfer with the heat sink. Convective heat transfer occurs between the heat sink and the atmosphere. A heat sink is usually referred to as an extended surface [16].

Extended surfaces or fins can have different configurations. Fins can be straight with a uniform cross section, straight with a nonuniform cross section, annular, or pin fins. Figure 2.4 shows different fin configurations [16]. Furthermore, fins can operate with a longitudinal air flow or a lateral air flow. Figure 2.5 shows an example of a DC-DC converter enclosed with a longitudinal air flow heat sink and an example of a DC-DC converter enclosed with a lateral air flow heat sink [17].

In the case of enclosed power electronics systems, conduction occurs in the x, y, and z directions. More specifically, it is assumed that conduction exits in the x and y directions along the plane of the power electronics system, in addition to conduction in the z direction from the power electronics system to the heat sink.

Similar to the 1-D and 2-D RC thermal models, the first step in designing 3-D RC thermal models is to discretize the system. In the case of 3-D systems, the system is discretized into voxels. Each voxel is assigned a capacitance value. For simplicity, the discretization can be done at the level of the functional element. Each functional element in the 3-D system is represented by a voxel and is assigned a capacitance value. Adjacent voxels that do not have an exposed surface to the ambient conditions are connected to each other along the x, y, and z directions through conduction resistances only. However, the voxels that are exposed to the ambient conditions have an additional resistance that connects them to a voltage source in the

3-D RC thermal model. The additional resistance represents the convective heat transfer from the corresponding part of the overall system to the ambient conditions. The conduction resistances along the x, y, and z directions are calculated using (2.2). However, L and A_c depend on the direction along which the heat is being conducted. The convection resistances cannot be calculated using (2.3). To calculate the convection resistances from the voxels of the finned structure to the ambient conditions, the equations of heat transfer from extended surfaces must be used [16]. The effective resistance that accounts for convection in extended surfaces can be found using

$$R_{t,0} = \frac{1}{\eta_0 h A_t}, \tag{2.6}$$

where $R_{t,0}$ is the overall effective resistance, η_0 is the overall efficiency of an array of fins, h is the convective heat transfer coefficient, and A_t is the total surface area of the extended surface. The overall efficiency for an array of fins is found using

$$\eta_0 = 1 - \frac{NA_f}{A_t}(1 - \eta_f), \tag{2.7}$$

where N is the number of fins in an array, A_f is the surface area of a single fin, and η_f is the efficiency of a single fin. The total surface area A_t for N fins in an array is found using

$$A_t = NA_f + A_b, \tag{2.8}$$

where A_b is the surface area of the exposed part of the base of the extended surface. For straight rectangular fins with active tip, the efficiency of every fin in the array can be found using

$$\eta_f = \frac{\tanh ml_c}{ml_c}, \tag{2.9}$$

where l_c is a corrected length found using

$$L_c = L + \frac{t}{2}. \tag{2.10}$$

Here L is the length of the fin, and t is the thickness of the fin. If the width of a rectangular fin is much larger than its thickness, the parameter m can be found using

$$m = \sqrt{\frac{2h}{kt}}, \tag{2.11}$$

where k is the thermal conductivity of the material of the extended surface, and h is the heat transfer coefficient.

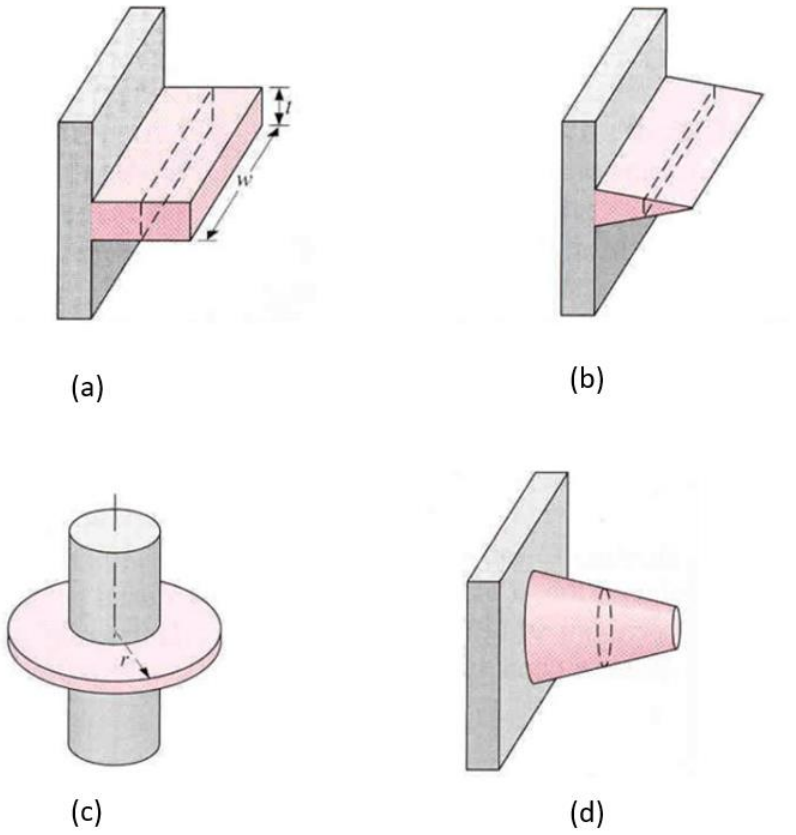

Figure 2.4 Different fin configurations. (a) Straight fin of uniform cross section. (b) Straight fin of nonuniform cross section. (c) Annular fin. (d) Pin fin.

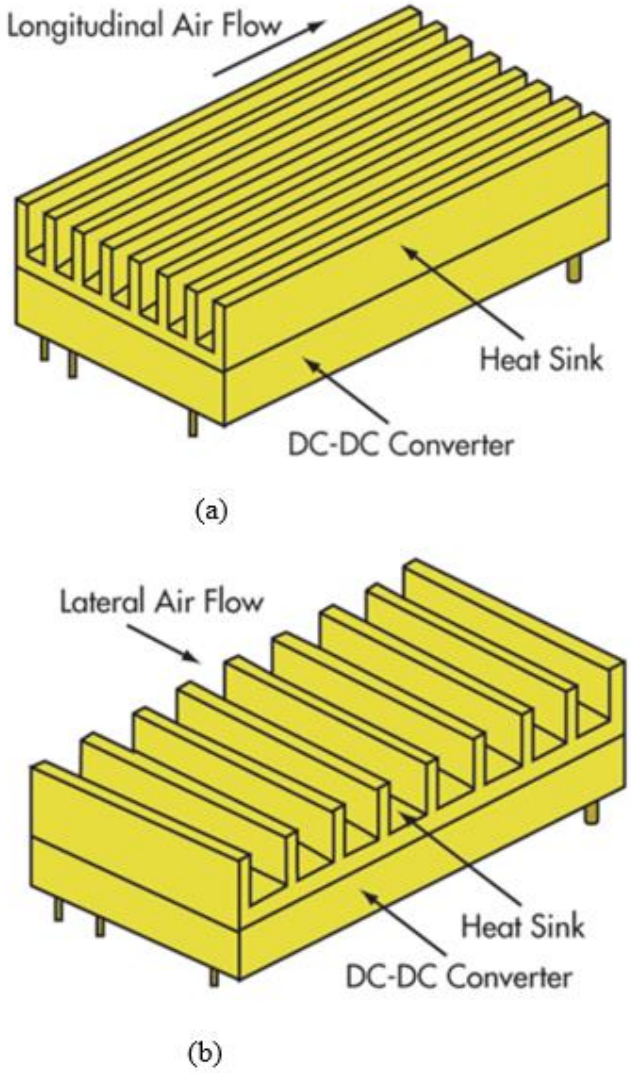

Figure 2.5 Enclosed DC-DC converter. (a) Enclosed DC-DC converter with longitudinal air flow heat sink. (b) Enclosed DC-DC converter with lateral air flow heat sink.

2.2 Network modeling

2.2.1 Thermal network representation

In order to design a filter that provides an accurate dynamic spatial thermal estimation of power electronics systems, a state space representation of the thermal model is needed [8].

The state space is derived from a directed weighted graph $G = (V, E, W)$ that can represent the interconnected RC thermal model, where $V = \{1, 2, ..., n\}$ denotes the set of vertices of a graph of n nodes, E denotes the set of edges that connect adjacent vertices, and W denotes the weights of the edges which represent the thermal resistance values between the capacitances of the thermal model in the case of RC models. Graph-based modeling has been used in the literature in different areas. It was found to be a useful tool for modeling of power electronics systems [18], thermal modeling of buildings [19][20][21], among many other applications. The main advantage of this modeling technique is that it captures the structure of the conservation of mass and energy laws in these systems [22].

The RC thermal models described in the previous subsections can be represented by directed weighted graphs in which each vertex represents a capacitor of the RC thermal model, each directed weighted edge represents a conduction or a convection resistance of the RC thermal model, and each weight represents the value of the corresponding resistance of the RC thermal model. The ambient atmosphere is modeled by a single node or vertex with an infinite capacitance in the graph-based themal model. The direction of the edges represents the direction of positive heat flow between the corresponding adjacent nodes. The resistance values of the edges are equal in both directions, i.e. $R_{ij} = R_{ji}$ on the edge (i, j). However, since the heat can flow only in one direction (from the higher temperature node to the lower temperature node), a direction was assigned to every node in the graph. This makes the graph directed. Graph-based model can be used to represent 1-D, 2-D, or 3-D RC thermal models. Figure 2.6 shows the 2D graph-based model representation of the 2-D RC thermal model of Figure 2.3. The edges in Figure 2.6 represent the conduction along the x and y direction between adjacent nodes, in addition to convection from each node to the ambient atmosphere. The ambient atmosphere is modeled by the center node Ta.

The state space thermal models for power electronics systems that are enclosed with a heat sink are derived from 3-D RC thermal models. The thermal networks for those systems can also be represented by directed weighted graphs $G = (V, E, W)$. However, in this case the edges of the thermal networks represent conduction in the x, y, and z directions. Figure 2.7 shows an example of a 3-D graph-based thermal model. The first vertical layer that contains the first 4 nodes represents the power electronics system, i.e. the inverter of a power electronics

system that is enclosed with a heat sink. The current source connecting to the first node in the inverter layer represents a source of heat that exists in the corresponding location of the inverter. The second vertical layer that contains the second 4 nodes represents the nodes of the heat sink. The edges in each of the two vertical layers represent conduction resistances in the x and y directions between adjacent nodes. The edges that connect the two vertical layers represent the conduction resistances in the z direction between the inverter and the heat sink. Furthermore, the layer that represents the heat sink contains additional edges connected to the ambient atmosphere node. Those additional edges represent the convection resistances from the heat sink to the ambient atmosphere.

The dynamic thermal behavior of the power electronics systems is then obtained by applying the conservation of energy law on every vertex in the graph-based model. The same strategy can be applied on 1-D, 2-D and 3-D graph-based thermal models. The energy balance equation states that the thermal energy stored in each node is a function of the thermal energy entering the node, the thermal energy leaving the node, and the thermal energy generated in that node. Therefore, the dynamics of the system are represented by a system of coupled first order differential equations given by

$$C_i \frac{dT_i}{dt} = q_i, \tag{2.12}$$

where C_i denotes the thermal capacitance of node i, T_i denotes the temperature of node i, and q_i denotes the net heat flow into node i.

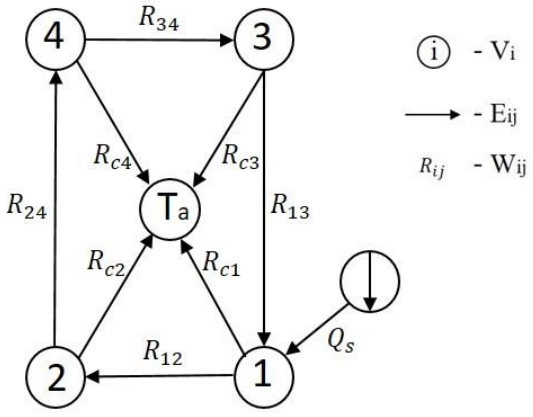

Figure 2.6 Example of a 2-D graph-based thermal model.

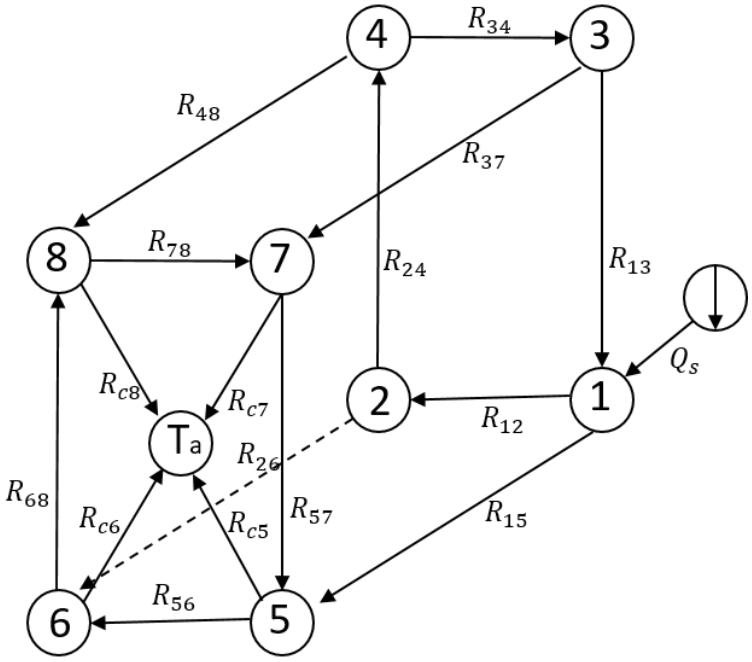

Figure 2.7 Example of a 3-D RC graph-based thermal model.

The net heat flow q_i into node i is the difference between the heat flow entering into node i and the heat flow leaving from node i. The heat flow entering into a node can be through conduction from adjacent nodes or through heat generation Q_s from the active component represented by the corresponding node in the graph-based thermal model. The heat flow leaving from a node can be through conduction from that node to the adjacent nodes or through convection from that node to the ambient atmosphere. The heat flow from node i to node j is calculated as $(T_i - T_j)/R_{ij}$, where R_{ij} can be the conduction resistance or the convection resistance. The set of the coupled differential equations can be expressed in a state space form as

$$\dot{\vec{x}} = A\vec{x} + B\vec{u} + V\vec{d}, \tag{2.13}$$

where the state vector $\vec{x}$ represents the temperature of each node or vertex of the graph-based model, the matrix $A = [a_{ij}]$ represents the system dynamics, the vector $\vec{u}$ represents the heat input from the heat generating components in the system, and $\vec{d}$ represents the disturbance to

the system which is the ambient atmosphere in this case. The state space derivation from the graph-based thermal model will be explained in more detail in the following subsection.

2.2.2 State space model

By applying the conservation of energy on every vertex in the graph-based thermal model of the power electronics system, the linear state space thermal model (2.13) can be obtained. The state space thermal model of the 2-D graph-based model shown in Figure 2.6 will be obtained as an example of this concept. The graph-based thermal model has 4 nodes. Therefore, the state space thermal model will have 4 states. By applying the conservation of energy equation on each vertex of the 2-D graph-based thermal model, the system of 4 first order coupled differential equations shown below will be obtained.

$$C_1\dot{T}_1 = \frac{T_2 - T_1}{R_{12}} + \frac{T_3 - T_1}{R_{13}} - \frac{T_1 - T_a}{R_{c1}} + Q_s \tag{2.14}$$

$$C_2\dot{T}_2 = \frac{T_1 - T_2}{R_{12}} - \frac{T_2 - T_4}{R_{24}} - \frac{T_2 - T_a}{R_{c2}} \tag{2.15}$$

$$C_3\dot{T}_3 = \frac{T_4 - T_3}{R_{34}} - \frac{T_3 - T_1}{R_{13}} - \frac{T_3 - T_a}{R_{c3}} \tag{2.16}$$

$$C_4\dot{T}_4 = \frac{T_2 - T_4}{R_{24}} - \frac{T_4 - T_3}{R_{34}} - \frac{T_4 - T_a}{R_{c4}} \tag{2.17}$$

Rearranging these 4 differential equations, the linear state space model (2.13) can be obtained, where

$$A = \begin{bmatrix} -\frac{1}{R_{12}C_1} - \frac{1}{R_{13}C_1} - \frac{1}{R_{c1}C_1} & \frac{1}{R_{12}C_1} & \frac{1}{R_{13}C_1} & 0 \\ \frac{1}{R_{12}C_2} & -\frac{1}{R_{12}C_2} - \frac{1}{R_{24}C_2} - \frac{1}{R_{c2}C_2} & 0 & \frac{1}{R_{24}C_2} \\ \frac{1}{R_{13}C_3} & 0 & -\frac{1}{R_{13}C_3} - \frac{1}{R_{34}C_3} - \frac{1}{R_{c3}C_3} & \frac{1}{R_{34}C_3} \\ 0 & \frac{1}{R_{24}C_4} & \frac{1}{R_{34}C_4} & -\frac{1}{R_{24}C_4} - \frac{1}{R_{34}C_4} - \frac{1}{R_{c4}C_4} \end{bmatrix},$$

$$B = \begin{bmatrix} \frac{1}{C_1} \\ 0 \\ 0 \\ 0 \end{bmatrix},$$

and

$$V = \begin{bmatrix} \frac{1}{R_{c1}C_1} \\ \frac{1}{R_{c2}C_2} \\ \frac{1}{R_{c3}C_3} \\ \frac{1}{R_{c4}C_4} \end{bmatrix}.$$

Therefore, it can be seen that the system dynamics matrix $A = [a_{ij}]$ is given by

$$a_{ij} = \begin{cases} 0, i \neq j, (i, j) \notin E \\ \frac{1}{C_i R_{ij}}, i \neq j, (i, j) \in E \\ -\sum_{k \neq i} a_{ik} + \frac{1}{C_i R_{ci}}, i = j, (i, j) \in E \end{cases} \tag{2.18}$$

The previous example shows how to derive the linear state space thermal models of 2-D systems. However, the dynamic thermal behavior of 3-D systems is obtained using (2.12) also which results in a system of coupled first order differential equations that can be rearranged in the same form as that of the 2-D state space thermal models. Hence, the state space model structure of 3-D systems is similar to that of 2-D systems.

It will be shown in Chapters 5 and 6 that an actual power electronics system usually has many components. Discretizing the system at the level of the functional elements will result in a large number of capacitors in the RC thermal model which means a large number of nodes in the graph-based thermal model. Therefore, the resulting state space thermal model of an

actual power electronics system will have a large number of states which imposes a high computational cost. Also, it will be problematic to implement such a complex system in an online estimator. Hence, a method that reduces the complexity of the thermal model while preserving its accuracy and structure is needed.

Chapter 3
Model Order Reduction

3.1 Literature review

The design, analysis, optimization, control and estimation of complex physical systems require the use of a virtual model that captures, as accurately as possible, the behavior and different interactions of the system. Virtual models or computer simulations are useful in reducing the time needed to obtain the output of a system that might take hours, weeks, or even days to get if the experiment was performed on the physical system directly. Furthermore, running the experiment on the physical system directly might be costly, dangerous, and even impossible in some cases. Therefore, the need of realistic computer simulations of complex systems is increasing [23].

In 1965, Moore predicted that computer speed will double every 18 months [24]. Figure 3.1 shows the increase in the number of transistors in typical Intel chips as a function of years [25]. The figure shows that there are 42 million transistors in the Pentium 4 chip compared to less than 10 thousand transistors in chips that were almost 30 years old at that time. This significant increase in the computational power made it possible for researchers to create more realistic models that include complex interactions of different domains of the physical system.

However, even with the increase of the computational power, the complexity of the highly realistic models can become problematic in some cases. Modeling all the interactions of physical systems in full detail increases significantly the dimensionality of the model and might require unrealistic storage capacity and computational power. Therefore, decreasing the

dimensionality or the complexity of the simulation model is crucial for the analysis or control of some physical phenomena [26].

It might be reasonable to think that decreasing the complexity of the model decreases its accuracy. However, it was shown that in most cases it is possible to neglect some details of the physical system and still be able to extract the output or the information needed from the model. Figure 3.2 shows a graphical representation of the model order reduction concept [27]. It can be seen that many details of the model can be neglected, but the final result can still be captured. Operational model order reduction depends on the intuition of the researcher in order to neglect some details in the model and hence obtain a relatively low dimensional model. This approach is used for example to model the blood flow in the entire human body [27].

In some other applications, it is not possible to reduce the complexity of the model a priori, and a high dimensional model that requires huge storage capacity and computational power is obtained. Therefore, control design and filtering become computationally expensive or even impossible. In such cases, model order reduction (MOR) techniques are used.

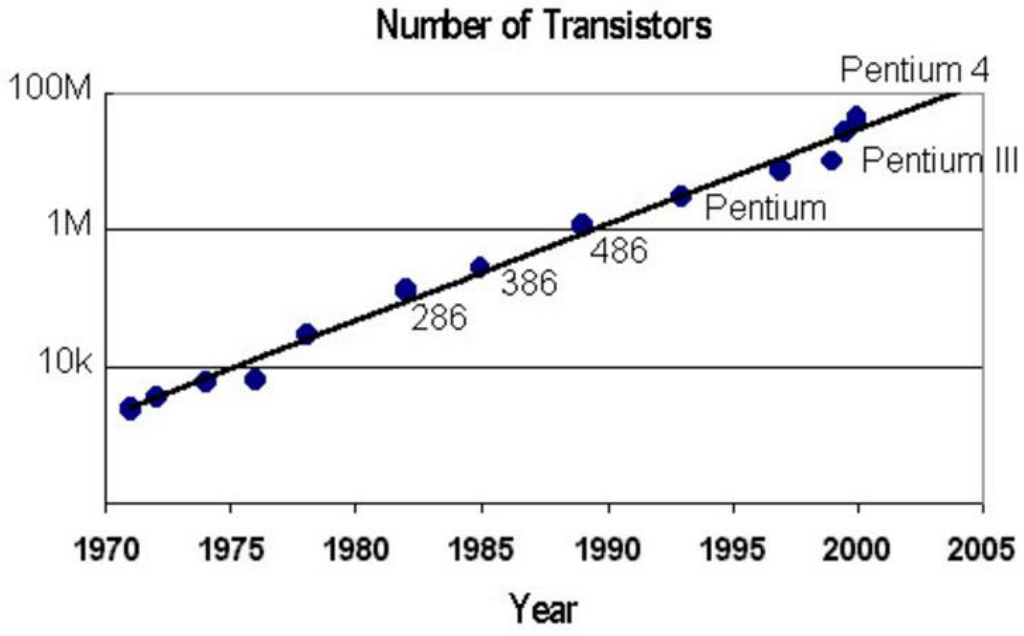

Figure 3.1 The increase in the number of transistors in typical Intel chips as a function of years. There are 42 million transistors in the Pentium 4 chip [25]**.**

MOR is a huge research field. Researchers have already developed many methods to reduce the complexity of a model while preserving its input-ouput behavior. Every MOR technique is useful for a certain application but the main objective of all the MOR techniques is to obtain a simpler model while preserving, as much as possible, the details of the original model.

Besides the significant decrease of the dimensionality of the original highly complex large-scale model, MOR techniques should have some other properties such as having a good representation of the physical system, preserving some system properties like stability and passivity, having a small approximation error, having a global error bound, and being numerically stable, and efficient [26].

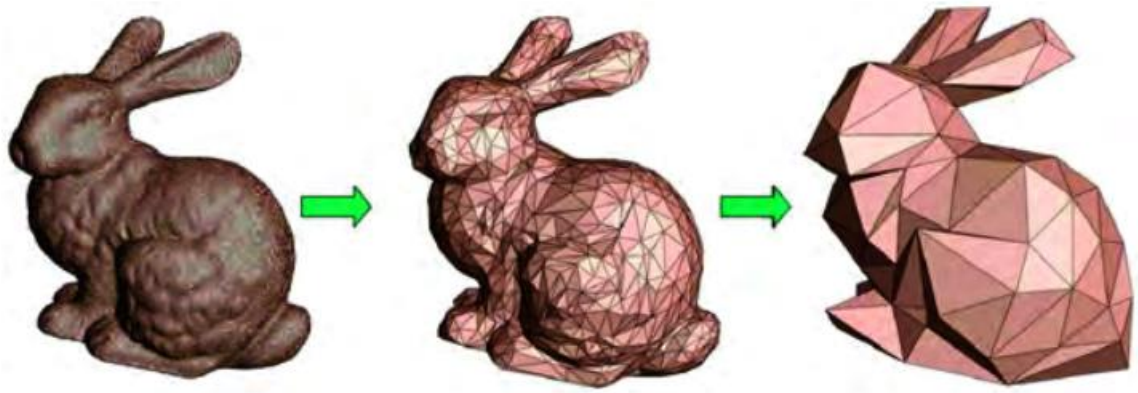

Figure 3.2 Graphical representation of the model order reduction concept [27]**.**

Research has been done for developing MOR techniques for linear systems and nonlinear systems. Hence, MOR techniques can be classified under methods suitable for linear systems and methods suitable for nonlinear systems. Figure 3.3 shows that singular value decomposition (SVD) based methods, moment matching methods, modal based reduction methods, and hybrid methods can be classified under MOR techniques used for linear systems. On the other hand, proper orthogonal decomposition (POD) methods, and the trajectory piecewise linear method can be used for MOR of nonlinear systems.

The problem formulation of MOR is as follows. Given the following dynamical system

$$\begin{aligned} \dot{x} &= f(x,u) \\ y &= g(x,u), \end{aligned} \tag{3.1}$$

where $x \in R^n$. Find a lower dimensional system

$$\begin{aligned} \dot{\hat{x}} &= \hat{f}(\hat{x},u) \\ \hat{y} &= \hat{g}(\hat{x},u) \end{aligned} \tag{3.2}$$

where $\hat{x} \in R^m$, with $m < n$, while preserving the input-output relationship.

There are many MOR methods based on the singular value decomposition approach. The Hankel norm approximation method is a well known MOR technique based on SVD [28][29]. This method was introduced in 1971 and is based on minimizing a certain norm of the error between the full order model and the reduced order model. Balanced truncation, introduced by Moore in 1981, is another famous MOR technique based on SVD. Balanced truncation is a projection based method in which the system is transformed into a basis in which the states that are difficult to reach are also difficult to observe. The reachability and the controllability grammians are diagonalized. Then the method is applied by truncating the states that are hard to reach and simultaneously hard to observe [30][31] . Another method that falls under SVD based methods is the singular perturbation method [32]. The main difference between the singular perturbation method and the direct truncation method is that the latter method tends to have small errors at high frequencies and larger errors at low frequencies, while the former method tends to have large errors at high frequencies and smaller errors at low frequencies.

Another set of methods that can be used for the model order reduction of linear systems is the moment matching methods, known as the Krylov subspace methods [33], or Pade approximation methods [34]. These methods are projection based methods. In these methods, the transfer function is expanded using a Laurant series around a given point s_0 in the complex plane [26] as shown below.

$$G(s_0 + \sigma) = \eta_0 + \eta_1\sigma + \eta_2\sigma^2 + ... \tag{3.3}$$

η_t are the moments of the linear system at the expansion point. The Laurant series of the reduced order model is given as

$$\hat{G}(s_0+\sigma)=\hat{\eta}_0+\hat{\eta}_1\sigma+\hat{\eta}_2\sigma^2+.... \tag{3.4}$$

The method is applied by matching k moments such that

$$\eta_i=\hat{\eta}_i, i=1,2,...,k \tag{3.4}$$

where $k<n$.

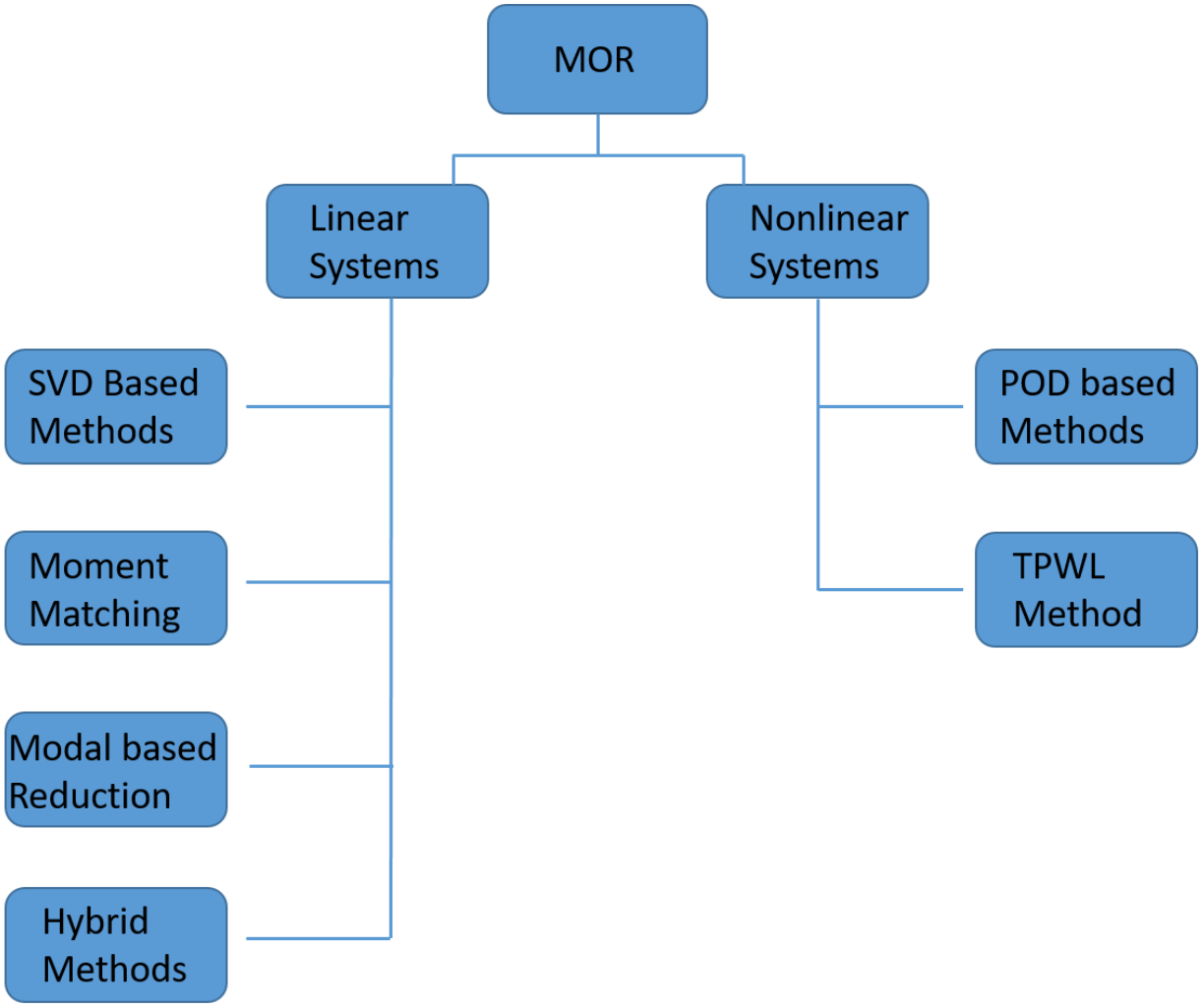

Figure 3.3 Classification of model order reduction techniques.

Using modal techniques, a closed-form formulation can be obtained in the reduction of linear systems. Before deciding on the modal technique used to reduce the complexity of the large-scale model, the user needs to determine the order of the reduced order model, the dominant modes, and the most sensitive state variables that should be kept in the reduced order model. There are many methods that fall under modal techniques. However, the main concept behind all these methods consists of neglecting the dynamics of the fast nodes in the large-scale model. [35] reviews six commonly-used modal based model order reduction techniques.

Furthermore, reducing the complexity of large-scale models can be done using a combination of several model order reduction techniques methods. This approach is known as a hybrid method. For example, Krylov subspace methods can be combined with other MOR techniques to reduce the number of states of the model [36]. Using hybrid methods, the user can take advantage of the benefits of each model order reduction technique used which makes hybrid MOR methods suitable for various applications.

Some model order reduction techniques can be applied to nonlinear systems. Proper orthogonal decomposition (POD) is an example of a MOR technique that can be used to reduce the complexity of large-scale nonlinear systems. POD can be seen as a MOR technique or as a data analysis tool. POD is also known as Principal Component Analysis or the Karhunen-Loeve Decomposition [37]. It should be noted that the discrete version of the POD is the SVD. This method consists of approximating a time-varying function over some domain of interest as the sum of some special ordered orthonormal functions called the proper orthogonal nodes of the time-varying function. The large-scale model is then reduced by representing it with its most energetic nodes.

Another MOR technique that can be applied to large-scale nonlinear models is the trajectory piecewise linear MOR technique. In this technique, the large-scale nonlinear system is represented by a piecewise linear system and then the reduction of these pieces is done with a Krylov projection [38].

A lot of research is being conducted in the MOR field as the need to analyse and control highly complex physical systems involves the use of low dimensional models that do not require huge storage capacity and computational cost. Hence, there is a huge number of MOR techniques that were developed. Each method is useful for a specific application. It should be

noted that many of the MOR techniques that were originally created for reducing the complexity of linear systems were extended to be applied on nonlinear systems as the need to use more realistic models requires including nonlinearities in the system. For instance, a lot of research has been done to extend the balanced truncation MOR technique towards nonlinear systems [39], [40], [41], [42].

In the next section, a MOR technique that reduces the complexity of large-scale models while preserving the structure or the physical meaning of the states in the reduced order model will be presented. The importance of this property in the MOR techniques will become clear in the 2-dimensional and 3-dimensional case studies presented in the upcoming chapters.

3.2 A structure-preserving model order reduction technique

3.2.1 Advantage of a structure-preserving MOR technique

A very brief overview of some commonly used MOR techniques was presented in the previous section. The focus of these MOR techniques was to reduce the complexity of the large-scale models while preserving the input-output behavior of the system in addition to some other properties like passivity and stability. However, preserving the structure of the full order model was not presented as an important property that should be found in these MOR techniques.

In chapter 2, it was shown that RC models can be used to simulate the dynamic thermal behavior of power electronics systems with good accuracy and relatively small computational cost compared to other numerical thermal analysis methods such as finite element analysis, for example. However, the RC thermal models of actual power electronics systems, i.e. an inverter or a set of coupled inverters, result in a large number of capacitors. This will result in a large number of states when the RC model is converted to its state space form. Therefore, a MOR technique that reduces the complexity of the RC thermal model, or the number of states of the state space thermal model, is needed especially when 3-dimensional RC thermal modeling is used.

MOR of RLC (resistor-inductor-capacitor) circuits have been extensively studied in the literature in order to generate reduced order macroscale models [43], [44], [45], [46]. However,

an ideal MOR technique for RLC circuits would result in a reduced order model in the form of a RLC circuit [47], [48]. This is the objective of structure-preserving MOR techniques. This feature in the structure-preserving MOR techniques is known by reciprocity.

The dynamic thermal estimation of power electronics systems requires the use of the less general from of RLC ciruits. More specifically only RC circuits will be used to model the dynamic thermal behavior of the power electronics systems. Hence, a structure-preserving MOR technique for RC circuits will be used in order to obtain a lower dimensional RC circuit that is easier to work with in a filter or a controller.

This reciprocity between the full order RC thermal model and the reduced order RC thermal model will allow the user to analyze the reduced order model as a RC circuit. More specifically, the user will be able to analyze and monitor the dynamical thermal behavior of every component of the power electronics system using the reduced order RC thermal model. This is possible since, as it was shown in the RC modeling section, every component of the power electronics system is represented by a specific capacitor in the RC thermal model. Therefore, if the states of the reduced order RC thermal model still have their physical meaning, the user will be able to track the dynamical thermal behavior of every component of the power electronics system using the reduced order RC thermal model.

Furthermore, the dynamic thermal estimation of power electronics systems requires solving a sensor placement problem. The user needs to find an appropriate number and placement of temperature sensors that should be used with an observer in order to recreate the dynamical thermal behavior of all the states of the power electronics system. Having this reciprocity between the full order RC thermal model and the reduced order RC thermal model allows the user to use the reduced order RC thermal model to solve the sensor placement problem. More specifically, when there is a physical correspondence between the states of the reduced order RC thermal model and the power electronics system, the user will be able to identify the locations of the temperature sensors on the physical system using the reduced order RC thermal model to solve the sensor placement problem. Without this reciprocity, the physical locations of the temperature sensors on the power electronics system will be lost. This idea will become clear in the upcoming chapters where a 2-dimensional and a 3-dimensional case studies are presented.

In the next two subsections, a structure-presesrving model order reduction technique for RC circuits will be reviewed. This method was previously developed in the literature. The technique is based on Markov chain aggregation. The main idea behing this MOR technique is to aggregate the capacitors of the full order RC thermal model into “super-capacitors” that represent a larger portion of the power electronics system modeled, i.e. the inverter. The aggregation of the capacitors will reduce the number of states of the RC thermal model by applying a spectral algorithm. The computation steps needed to obtain the reduced order RC thermal model will be presented. This method will be applied to reduce the complexity or the number of states of the 2-dimensional RC thermal models and 3-dimensional RC thermal models. The reduced order RC thermal model will be then used in an observer in order estimate the dynamic thermal behavior of all states of the system.

3.2.2 An aggregation-based model order reduction technique

The MOR technique used in this work to reduce the complexity of the RC thermal models of the power electronics systems is based on the method developed in [48], [49],[50]. This method was developed for the reduction of linear systems and was extended for the reduction of nonlinear systems. This MOR method is based on the Markov chain aggregation. It was previously used to reduce the RC thermal models of buildings. In the linear version of the method, the thermal model of the building was represented by a RC thermal model that resulted in a linear state space model. To reduce the number of states of the linear state space model, the linear thermal model was connected to a Markov chain and was reduced by applying the aggregation of Markov chains. In the extended version of the method, the thermal models of the buildings were more sophisticated and resulted in a linear part that captures the nodal thermal interactions of the building thermal model and a bilinear part that resulted from the heat flux into the zone space. To reduce the nonlinear thermal models, their linear terms were connected to a continuous time Markov chain and the aggregation method of Markov chains was applied. Then the nonlinear term is aggregated based on some optimal coordination.

The main advantage of this aggregation-based MOR method is that it results in a reduced order thermal model that has the same structure as the full order thermal model without

computational difficulties. More specifically, the resulting reduced order thermal model has the structure of a RC thermal model.

It was shown that the thermal dynamics of the buildings are similar to a time-homogeneous Markov chain. However, since the thermal model used to simulate the dynamic thermal behavior of the power electronics systems is similar to the thermal model of buildings, it is clear that the thermal dynamics of the power electronics systems are also similar to a time-homogeneous Markov chain. Hence, the thermal model of the power electronics systems can be aggregated using Markov chains aggregation techniques.

It should be noted that this aggregation-based MOR technique is applied on the thermal networks that represent the RC thermal models of the power electronics systems. Developing a thermal network that represents a RC thermal model was presented in the previous chapter. It was shown that a thermal network is represented as $G = (V, E, W)$, which is a set of vertices, edges, and weights. Each vertex represents a capacitor, each edge represents a resistor, and each weight represents the value of that resistance.

The main idea behind this model order reduction technique is to find an optimal partition function $\vartheta : V \to M$, where $M = \{1, 2, ..., m\}$ with $m < n$. The partition function ϑ reduces the dimension of the state space from n nodes in the full order model into m nodes in the reduced order model. Each super node has a super capacitance $\bar{C}$ and a super-temperature $\bar{T}$. Super nodes are connected by super-resistances $\bar{R}$. The super-capacitance and the super- resistance are given by

$$\bar{C}_k = \sum_{i \in V} C_i, \tag{3.5}$$

$$\bar{R}_{kl} = \frac{1}{\sum_{i,j \in E} \frac{1}{R_{ij}}}. \tag{3.6}$$

In order to aggregate the nodes of the full order model, the optimal partition function ϑ has to be found. This function is difficult to get exactly when the order of the reduced order model is greater than 2 which is the general case in these applications. Instead, the reduced order model is obtained by applying a spectral algorithm on the second eigenvector of the symmetric matrix

$$\hat{P} = 0.5(\Delta^{\frac{1}{2}} P \Delta^{-\frac{1}{2}} + \Delta^{-\frac{1}{2}} P^T \Delta^{\frac{1}{2}}) \tag{3.7}$$

derived from the thermal network that represents the RC thermal model of the system. Here

$$\Delta = diag(\pi), \tag{3.9}$$

where π is the stationary distribution of the Markov chain, and $P(t)$ is the Markov transition matrix. It was also shown in the previous chapter that a linear state space model is derived from the thermal network of the power electronics systems. Therefore, the Markov transition matrix $P(t)$ is given by

$$P(t) := e^{At}. \tag{3.8}$$

The stationary distribution of the Markov chain is given in terms of the capacitances by

$$\pi_i = \frac{C_i}{\sum_{j \in V} C_j}, i \in V. \tag{3.9}$$

The computation steps performed to aggregate the capacitors of the full order RC thermal model into super-capacitors in the reduced order RC thermal model will be presented in the next subsection.

3.2.3 Computation steps of the reduced order thermal model

The reduction of the number of capacitors in the RC thermal model or the number of states in the state space form of the thermal model of the power electronics systems is done by aggregation in this work. A spectral partitioning algorithm is performed on the second eigenvector of (3.7). The computation steps of the algorithm used by this aggregation-based MOR technique are as follows.

1. Compute the symmetric matrix $\hat{P}$ using (3.7), (3.9), (3.8), and (3.9).
2. Check the sign of the second eigenvector of $\hat{P}$.
3. Aggregate the spatially adjacent nodes of the thermal network that share the same sign into super-nodes.

4. Calculate the super-capacitances of the super-nodes using (3.5), and the super-resistances that connect adjacent super-nodes using (3.6). Internal resistances in super-nodes are neglected.
5. Add the current sources that exist in the same super-nodes into a single current source.

An example of this aggregation-based MOR technique is illustrated in Figure 3.4 below. In this figure, a 2-D thermal network is shown. The network is composed of 10 nodes. Based on the sign structure of the second eigenvector of the matrix $\hat{P}$, every node in the thermal network was assigned a sign. The red nodes represent the nodes that share the positive sign according to $\hat{P}$. The blue nodes represent the nodes that share the negative sign. The aggregation algorithm states that the spatially adjacent nodes that share the same sign can be aggregated into super-nodes. Therefore, it was possible to aggregate the 10 nodes of the full order RC thermal model into 4 super-nodes in the reduced order RC thermal model. Each of the 4 super-nodes has a super-capacitance calculated using (3.5). The external resistances that connect super-nodes should be grouped together into super-resistances calculated using (3.6). The internal resistances that exist inside super-nodes are neglected.

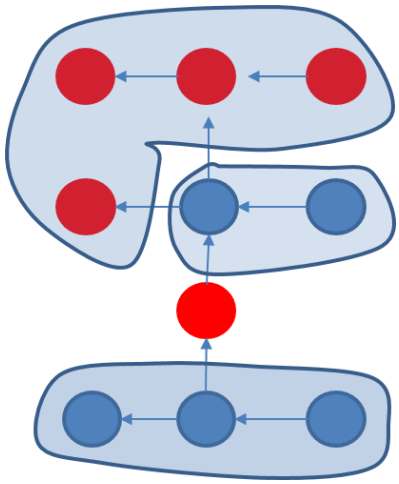

Figure 3.4 Graphical illustration of the aggregation-based MOR technique. The thermal network was reduced from 10 nodes in the full order thermal model into 4 nodes in the reduced order thermal model.

Chapter 4
Thermal Estimation

4.1 Filters

Measuring all the states of a dynamical system is essential to control the system, monitor its behavior and make sure it does not fail [51]. Using a sensor to measure every state in a system is usually expensive or even impossible. For example, using a temperature sensor to measure the dynamic thermal behavior of every component in an inverter increases the cost of the system significantly, reduces its reliability, and might cause packaging problems [8]. Hence, reconstructing the dynamic behavior of all the states of a dynamic system using a small number of sensors or a small number of state measurements is often desirable.

Observers, filters, or estimators, are dynamical systems that can reconstruct the entire state space of a system when some states cannot be measured directly. In most cases, measurements of the entire state vector are not available. However, using a state feedback control for example requires the knowledge of all the states of a system. In this case, an observer can be used to provide information about the missing internal states of the system that cannot be measured directly [52].

A lot of research has been done to develop observers and enhance their performance. The first attempt to develop an observer is presented in [53] where an observer that reconstructs the state vector of a linear state space model was developed. Observers were initially developed for linear systems and then extended towards nonlinear systems, nondeterministic systems, among many other forms of systems.

Observers can be grouped into two large categories. In the first category, a mathematical model of the plant is required to reconstruct the entire state vector. In the second category, the input output data is used to estimate the disturbance to the system [54]. A brief overview of some types of observers that require the use of a mathematical model to estimate the entire state vector will be presented. Two well known observers that belong to this category will be reviewed in some detail: the Luenburger observer, and the Kalman filter.

The Luenberger observer is a modification of the open-loop observer. The open-loop observer is one of the simplest forms of observers that can be used to estimate the state vector of a deterministic linear time-invariant system. In this type of observers, only the output of the plant is used by the observer to reconstruct the entire state vector. The problem formulation is as follows. Given the linear time-invariant system

$$\begin{aligned} \dot{x} &= Ax + Bu \\ y &= Cx, \end{aligned} \tag{4.1}$$

where the matrices A, B, and C are known and deterministic. The input vector u is known. y is the measurable output vector. The initial conditions $x(0)$ are usually unknown. The objective of the open loop observer is to estimate a state vector $\hat{x}$, such that $\hat{x} = x$, using the output vector y only. The dynamics of an open-loop observer are given by

$$\begin{aligned} \dot{\hat{x}} &= A\hat{x} + Bu \\ \hat{y} &= C\hat{x}. \end{aligned} \tag{4.2}$$

Since both the state space of the original system and the state space of the observer are using the same matrices, it can be seen that the estimated state vector converges to the actual state vector only if the initial condtions of the plant are known. However, this is usually not the case. Figure 4.1 shows a graphical illustration of an open loop observer. Since the observer is a dynamical system that has the same dynamics as the original system, it can be seen that the output of the observer $\hat{y}$ will be equal to the output of the original dynamical system, given that the initial conditions of the observer $\hat{x}(0)$ are equal to the initial conditions of the plant $x(0)$. If the initial conditions of the original system and the initial conditions of the observer are not equal, the estimated state vector will never converge to the actual state vector.

Furthermore, the performance of an observer can be studied in terms of the state estimation error. The state estimation error is the difference between the actual values of the states obtained from the state space model of the original system and the estimated values of the states obtained from the observer. The estimation error is defined as

$$e = x - \hat{x}. \tag{4.3}$$

The goal is to drive the estimation error of the observer to 0. The dynamics of the state estimation error of an open-loop observer are given by

$$\dot{e} = \dot{x} - \dot{\hat{x}} \tag{4.4}$$

$$\dot{e} = (Ax + Bu) - (A\hat{x} + Bu) \tag{4.5}$$

$$\dot{e} = Ae\,. \tag{4.6}$$

Therefore, the state estimation error of an open-loop observer converges to 0 only if the original system is stable. If the original system is not stable, the state estimation error of the open-loop observer diverges. Also, the user has no control over the rate of convergence of the estimated states to the actual states [55].

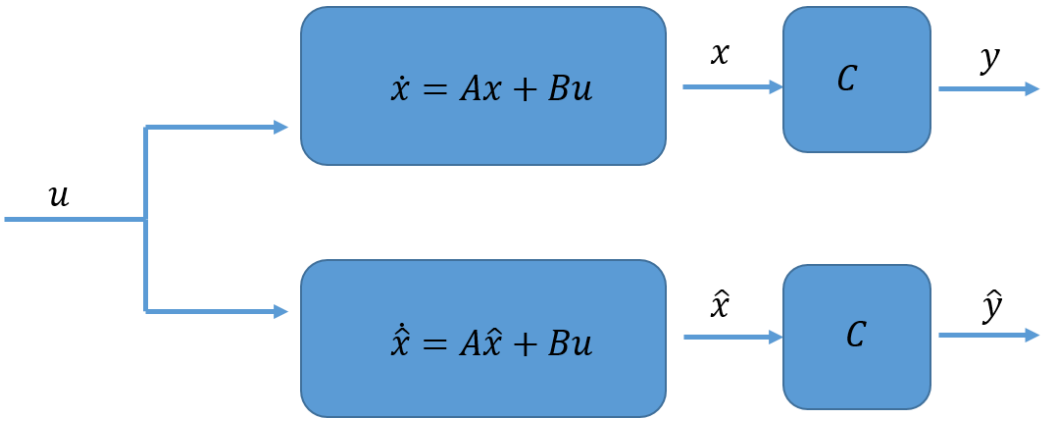

Figure 4.1 Graphical representation of an open-loop observer.

A well-known observer that can be used to recover the entire state vector of a system with unmeasurable states and unknown initial conditions is the Luenberger observer, also known by the closed-loop observer. The Luenberger observer was originally developed for deterministic linear time-invariant systems (4.1). Figure 4.2 shows a graphical representation

of the Luenberger observer. The main concept behind this closed-loop observer is that the difference between the estimated output vector and the actual/true output vector is fed back as an input to the observer.

The dynamics of the Luenberger observer are given by

$$\begin{aligned} \dot{\hat{x}} &= A\hat{x} + Bu + L(y - \hat{y}) \\ \hat{y} &= C\hat{x}, \end{aligned} \tag{4.7}$$

where L is the observer gain. The main difference between the open-loop observer and the Luenberger observer is the additional term in the observer dynamics equation that represents the difference between the actual output vector *y* and the estimated output vector $\hat{y}$ multiplied by the observer gain. The problem formulation of the Luenberger observer is follows. Given the deterministic linear time-invariant system (4.1), find the observer gain L such that the state estimation error (4.3) converges to 0, i.e. the estimated state vector converges to the actual state vector. The dynamics of the estimation error of the Luenberger observer are then given by

$$\dot{e} = \dot{x} - \dot{\hat{x}} \tag{4.8}$$

$$\dot{e} = (Ax + Bu) - (A\hat{x} + Bu + L(y - C\hat{x})) \tag{4.9}$$

$$\dot{e} = (A - LC)e \tag{4.10}$$

From (4.10), it can be seen that the state estimation error e tends to 0 as $t \to \infty$ when $(A - LC)$ is Hurwitz, i.e. all the eigenvalues of $A - LC$ have strictly negative real parts. Therefore, the observer gain L must be chosen such that $A - LC$ is Hurwitz. It should be noted that the eigenvalues of $(A - LC)$ can be placed arbitrarily iff the system is completely observable, i.e. the observability matrix is full rank. For the linear time-invariant system (4.1), the observability matrix is given by

$$\Omega = \begin{bmatrix} C \\ CA \\ \cdot \\ \cdot \\ \cdot \\ CA^{n-1} \end{bmatrix} \tag{4.11}$$

Therefore, it was shown that in the Luenberger observer the need for accurate initial conditions is eliminated by the process of feeding back the difference between the actual output of the system and the estimated output of the observer as an input to the observer.

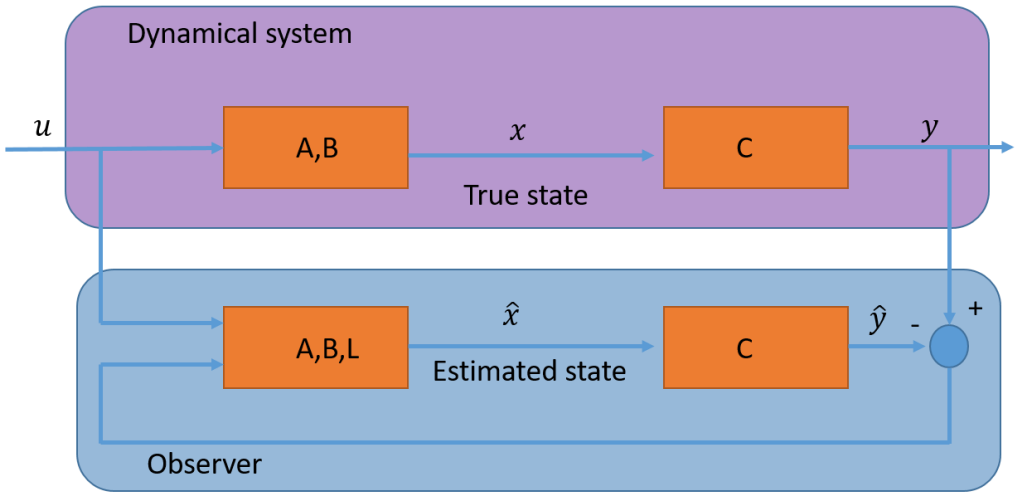

Figure 4.2 Graphical representation of the Luenberger observer.

It should be noted that the dynamic thermal models of the power electronics systems used in this work account for convective heat transfer from the system to the atmosphere. This heat transfer mode results in the additional vector d in the linear time-invariant thermal model of the system. The additional vector d represents the ambient temperature. Hence, the dynamics of the thermal model of the power electronics systems will be given by

$$\begin{aligned} \dot{x} &= Ax + Bu + Vd \\ y &= Cx \end{aligned} \tag{4.12}$$

In this case, the dynamics of the Luenberger observer are given by

$$\begin{aligned} \dot{\hat{x}} &= A\hat{x} + Bu + Vd + L(y - C\hat{x}) \\ \hat{y} &= C\hat{x} \end{aligned} \tag{4.13}$$

The dynamics of the state estimation error and the design of the observer gain L are the same as in the case with no disturbances in the system.

Many extensions have been performed on the original Luenberger observer. The observer was extended towards removing the steady state error. This extension of the Luenberger observer is known by the proportional integral observer (PIO). This observer has an additional integral gain used to reconstruct the disturbances and the unmodeled dynamics in addition to the state vector of the system. This observer has more robust estimation performance compared to the original Luenberger observer in the presence of unknown disturbances in the system [56]. The dynamics of the PIO are given by

$$\begin{aligned} \dot{\hat{x}} &= A\hat{x} + Bu + L(y - \hat{y}) + L_i \int L(y - \hat{y}) \\ \hat{y} &= C\hat{x}, \end{aligned} \tag{4.14}$$

where L_i is the integral gain of the PIO observer.

Furthermore, the Luenberger observer was extended towards nonlinear systems [57]. However, this form of the Luenberger observer is based on the assumption that knowledge about the nonlinear plant is available [54].

The dynamical systems estimated so far are deterministic, i.e. not stochastic. However, there is a type of observers that can be used to estimate the states of a stochastic system. In the next section, the well known Kalman filter that can be used to estimate the states of a dynamical system using noisy sensor measurements will be reviewed.

4.2 Kalman filter

The Kalman filter is a well-known optimal filter for linear systems in the case of Gaussian noise. This filter provides optimal estimates by minimizing their mean square error. It is a recursive procedure in which only the most recent sensor measurements are needed. Hence, it reduces the data storage capacity and the computation requirements needed. The

Kalman filter is a popular online processing form that provides very satisfying results in practice due to its optimality and ease of implementation.

The Kalman filter can be used to estimate the states of a discrete time plant with discrete time observations. This version of the Kalman filters is known as the discrete Kalman filter. Furthermore, the Kalman filter can be used to estimate the states of a continuous time plant with continuous time observations. This version of the Kalman filters is known as the continuous Kalman filter. Also, the Kalman filter can be used to estimate the states of a continuous time plant with discrete time observations. This version of the Kalman filters is known as the continuous-discrete Kalman filter [58].

In addition, many extensions and modifications were applied to the Kalman filter. The extended Kalman filter (EKF) is another version of the Kalman filters that was used to estimate the states of nonlinear systems [59]. It was shown later that the EKF might lead to sub-optimal estimates and in some cases, it might diverge. The Unscented Kalman filter (UKF) is a more recent version of the Kalman filters that can be applied to nonlinear systems and can address this issue in the EKF while having the same computational complexity [60]. Also, another version of the Kalman filters that deals with the state estimation of nonlinear systems in the Ensemble Kalman filter (EnKF). This version of the Kalman filters belongs to the class of particle filters [61],[62].

In this section, a brief overview of the most popular variations of the Kalman filters is presented. Next, the continuous-discrete version of the Kalman filters for linear systems will be reviewed in more details. This version of the Kalman filters will be used in this work to estimate the dynamic thermal behavior of the power electronics systems.

4.2.1 Continuous-discrete Kalman filter

In this section, the continuous-discrete Kalman filter will be presented. This version of the Kalman filter is a linear sequential continuous estimation from discrete observations. In a continuous-discrete Kalman filter, intermittent observations are easy to handle and sensor measurements can be taken at irregularly spaced instants of time. Another advantage of the continuous-discrete Kalman filter is that this approach provides optimal state estimates

continuously, including the instants between the observations [58]. The dynamics of the continuous- time plant are given by (4.1). The discrete-time observations are given by

$$y(m) = Hx(m) + v(m), \tag{4.15}$$

where $y(m)$ is the sensor output, H is a mapping from the true states into the observed states, and $v \in N(0, R_k)$ is the measurement noise which is assumed to be white noise with zero mean and covariance R_k. The computational cycle of the sequential estimation process of a continuous-discrete Kalman filter is shown in Figure 4.3. The Kalman filter can be seen as a predictor-corrector with a time update stage and a measurement update stage. In the time update stage, the state estimate is called a priori and represents a predicted value of the true state. In the measurement update stage, the state estimate is called a posteriori and represents a corrected version of that prediction. The a priori state estimate $\hat{x}_m^-$ is obtained by propagating the a posteriori state of the previous cycle $\hat{x}_{m-1}^+$ through the state transition matrix $\Phi(t_{m-1}, t_m)$. The a priori $\hat{x}_m^-$ is given by

$$\hat{x}_m^- = \phi(t_m, t_{m-1})\hat{x}_{m-1}^+ \tag{4.16}$$

where the state transition matrix is defined by

$$\frac{d\Phi(t,\tau)}{dt} = A\Phi(t,\tau). \tag{4.17}$$

The a posteriori $\hat{x}_m^+$ is then obtained by updating $\hat{x}_m^-$ by the observations at time T_m. The recursive updating procedure is given by

$$\hat{x}_m^+ = \hat{x}_m^- + K_m(y(m) - H\hat{x}_m^-). \tag{4.18}$$

The Kalman gain matrix K_m that results in the minimum variance estimate is given by

$$K_m = P_m^- H^T [HP_m^- H^T + R_m]^{-1}, \tag{4.19}$$

where the error covariance matrix P_m^- is the solution of

$$\dot{P} = AP + PA^T + Buu^T B^T . \tag{4.20}$$

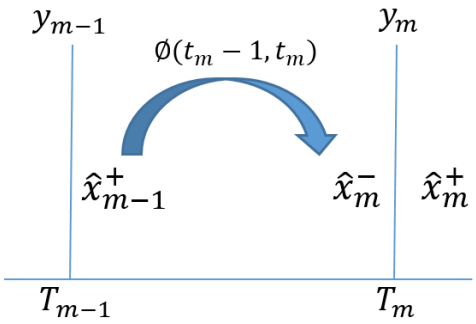

Figure 4.3 Graphical illustration of the computational cycle of the continuous-discrete Kalman filter.

A detailed derivation of the continuous-discrete Kalman filter is presented in [58]. This filter, along with an optimal number and optimal placement of temperature sensors, will be used in chapters 5 and 6 to obtain accurate dynamic temperature estimation of an actual power electronics system. It should be also noted that the continuous-discrete Kalman filter is the most intuitive version of the Kalman filters. In fact, the dynamics of the thermal model of the power electronics systems are continuously changing with time. Furthermore, the sensors measurements are obtained only at discrete instants in time. Hence, the dynamical estimation thermal problem of the power electronics system is a continuous- discrete problem by nature.

4.3 Optimal sensor placement

Increasing the number of sensors in a system increases the accuracy of the estimation process. However, it increases the cost of the system, interferes with its layouts, and might cause packaging problems. Therefore, optimizing the number of sensors is always desirable. Furthermore, the locations of the sensors in the system affect the accuracy of the estimation process as well. Placing the sensors at random locations might result in poor state estimates and consequently poor control designs. Therefore, finding the optimal locations of the sensors in a system is also crucial for the effectiveness and accuracy of the estimation process [63].

An optimization process with respect to the number and placement of temperature sensors was performed in this work. The optimization formulation has been done with the

underlying assumption that there be can a maximum of 1 sensor per each state. It means that a particular state may either have a sensor or not. Therefore, it is a binary condition.

There are many strategies that can be used to solve the optimal sensor placement problem. These strategies include integer programming methods, continuous relaxation methods, or even intuition-based methods [64]. The strategy adapted to solve the optimal sensor placement problem in this work is related to information-based performance metrics. More specifically, sensors can be placed based on the measure of the degree of observability of a dynamical system. The RC thermal model used in this work to model the dynamic thermal behavior of the power electronics systems is a linear time invariant model. Therefore, the linear observability Gramian can be used in solving the optimal sensor placement problem. The linear observability Gramian is given by

$$W_{o,linear} = \int_0^\infty e^{A^T t} H^T H e^{At} dt \tag{4.21}$$

There are many metrics by which one can determine the degree of observability of the states of a dynamic system [63], [65]–[68]. The trace analysis of the observability Gramian [69], [70] and the condition number of the observability Gramian have been considered as performance metrics in this work [71]. The trace of the observability Gramian refers to the sum of all Gramian eigenvalues. The trace of the observability Gramian is given by

$$Trace(W_{o,linear}) = \sum_{i=1}^{n} \sigma_i (W_{o,linear}). \tag{4.22}$$

Maximizing the trace of the observability Gramian increases the system observability.

On the other hand, smaller observability Gramian condition numbers correspond to improved observability [71]. The condition number of a matrix refers to the ratio of its largest and smallest magnitude eigenvalues. The condition number of the observability Gramian using logarithmic scaling is given by

$$C_o = \log_{10}[\frac{\sigma_{\max}(W_{o,linear})}{\sigma_{\min}(W_{o,linear})}]. \tag{4.23}$$

Maximizing the trace of the observability Gramian or minimizing the condition number of the observability Gramian result only in an optimal placement of a specific number of sensors. To find the optimal number of sensors, the state estimation error obtained from the continuous-discrete Kalman filter will be used. A comparison of the results of the optimal sensor placement problem obtained from the trace of observability Gramian and from the condition number of observability Gramian will be performed in chapter 5. Also, the analysis used to find the optimal number of temperature sensors will be presented in the case studies in chapter 5 and chapter 6.

Chapter 5
Dynamic Thermal Estimation of 2-D Power Electronics Systems

5.1 System description

The thermal estimation technique developed in this work was applied on a 2 kW, dc-ac, single-phase, 7-Level flying capacitor multilevel inverter [72] shown in Figure 5.1. This inverter is a highly power-dense device (216 W/in^3, input V_{max} = 400V). The main components of the circuit are Gallium Nitride (GaN) gate drivers, GaN transistors, ceramic capacitors, and Adum5210 digital isolators with integrated dc-to-dc converters. The Adum5210 devices are isolated level shifters that power the gate drivers. The ceramic capacitors help transfer electrical energy and reduce stress on switching devices. The main sources of heat in the board are the 12 GaN transistors. It should be noted that the temperature of the GaN transistors generally increases as power levels increase. In contrast, the temperature of the Adum5210 does not change significantly with the power level due to constant control losses.

The main printed circuit board (PCB) that represents the blue part of the board shown in Figure 5.1 is a 4-layer board composed of four layers of copper, three layers of a glass-reinforced epoxy laminate FR4, and two solder mask layers. The daughterboard that represents the red part of the board shown in Figure 5.1 is a 2-layer board composed of two copper layers, one FR4 layer, and two solder mask layers. The structure and thickness of the layers of the main board and the daughterboard are shown in Figure 5.2.

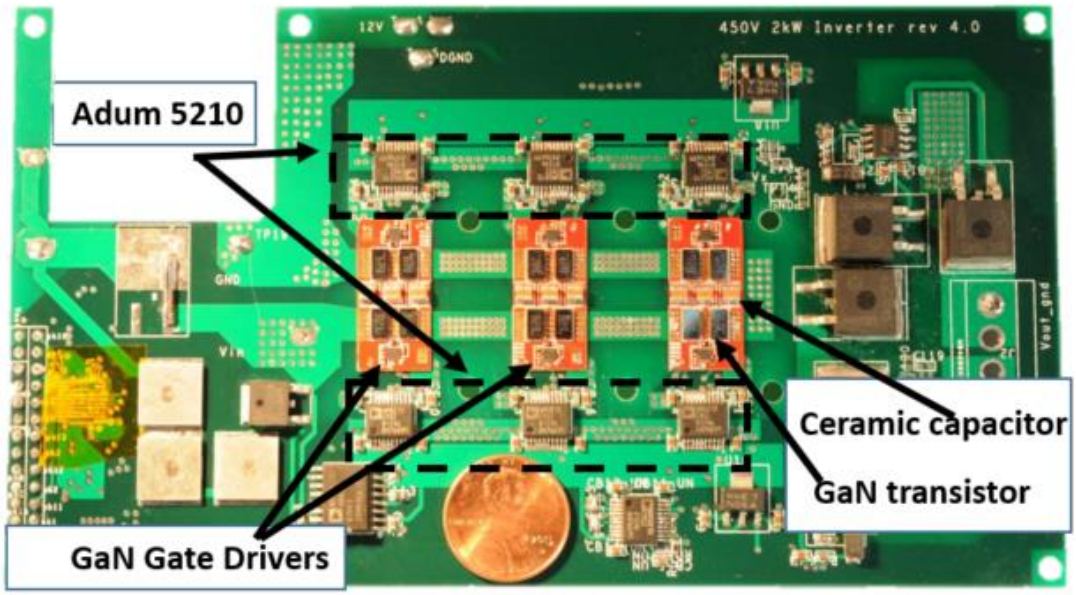

Figure 5.1 A 2 kW, dc-ac, single-phase, 7-level flying capacitor multilevel inverter [64]**.**

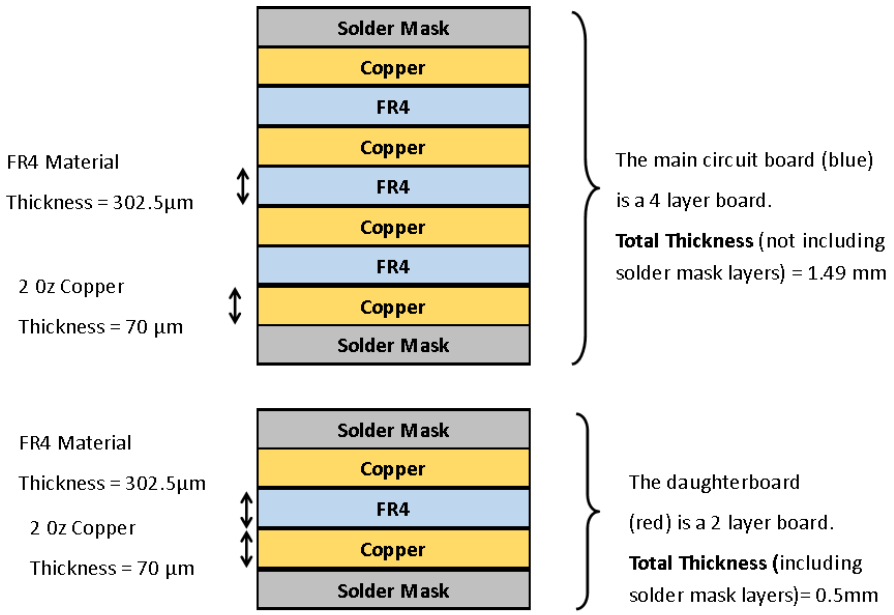

Figure 5.2 The structure and thickness of the layers of the main ciruit board (the blue part in Figure 5.1) and the daughterboard (the red part in Figure 5.1). The main circuit board is a 4-layer board and the daughterboard is a 2 layer-board.

5.2 2-D full order RC thermal model

The multilevel inverter shown in Figure 5.1 is open to the environment, i.e. not enclosed with a heat sink. Therefore, there is no conductive heat transfer in the z-direction in the system. However, there is conductive heat transfer in the x and y directions along the inverter. Hence, the thermal dynamics of the inverter shown in Figure 5.1 will be modeled using a 2-dimensional (2-D) RC thermal model. Using a 2-D RC thermal model, conduction along the x and y directions in the plane of the inverter, in addition to convection from the inverter to the environment, will be considered.

The first step in designing a RC thermal model is to discretize the inverter into pixels and assign a capacitance to each pixel. The thermal capacitance represents the ability of that corresponding part of the board to store heat in it. Also, the thermal capacitance models the thermal lag that occurs before the temperature of the system reaches a steady state value following a step change in the heat input. The discretization of the board is specified by the user. In this work, for the purpose of reducing the complexity of the full order thermal model, the discretization of the board was chosen at the level of the functional elements, i.e. each functional element of the board will be represented by capacitor in the RC thermal model. Adjacent capacitors will be connected to each other through resistances that represent the conduction resistances along the x and y direction since the RC thermal model is 2-dimensional. Figure 5.3 shows the discretization of the inverter.

The next step in designing a RC thermal model is to calculate the resistances and capacitors values. This step depends on the geometric properties and the material properties of the pixels. In particular, the length, the width, and the thickness of the pixels are required to calculate the capacitance and resistance values. The dimensions of an inverter sample have been enumerated. Numerical names were applied to the grid regions on the inverter as shown in Figure 5.4. The vertical (length) and horizontal (width) dimensions were acquired using electronic calipers. The dimensions for all the grid regions are shown in Table 5.1. Furthermore, the thermal conductivity, the specific heat coefficient, and the density of the material of the board are needed. As shown in Figure 5.2, the board is composed of copper and FR4. Table 5.2 shows the material properties for FR4 and copper. It should be noted that the

multilayered structure was treated as a homogeneous material with an in-plane effective thermal conductivity given by

$$K_{in-plane} = \frac{\sum_{i=1}^{N} K_i t_i}{\sum_{i=1}^{N} t_i}, \tag{5.1}$$

where K_i is the thermal conductivity of a single layer, t_i is the thickness of the corresponding layer, and N is the total number of layers. The effective thermal capacitance of the multilayered structure is the sum of the thermal capacitance of each layer,

$$C_{multilayered} = \sum_{i=1}^{N} C_i, \tag{5.2}$$

where C_i is the thermal capacitance of a single layer.

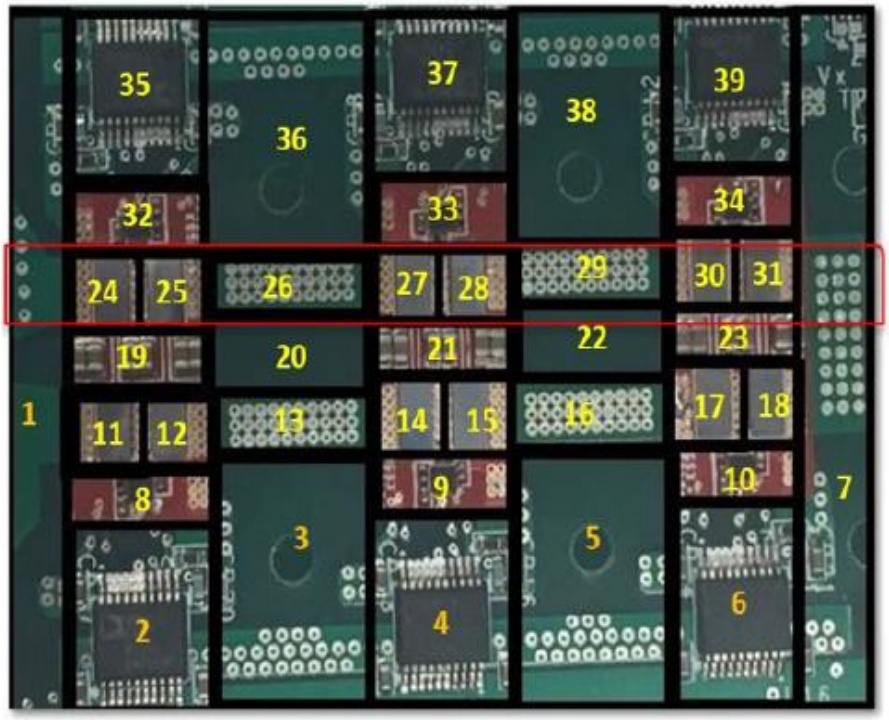

Figure 5.3 The discretization of the 2 kW multilevel inverter. The inverter was discretized at the level of the functional element. The discretization resulted in 39 capacitors in the 2-D RC thermal model.

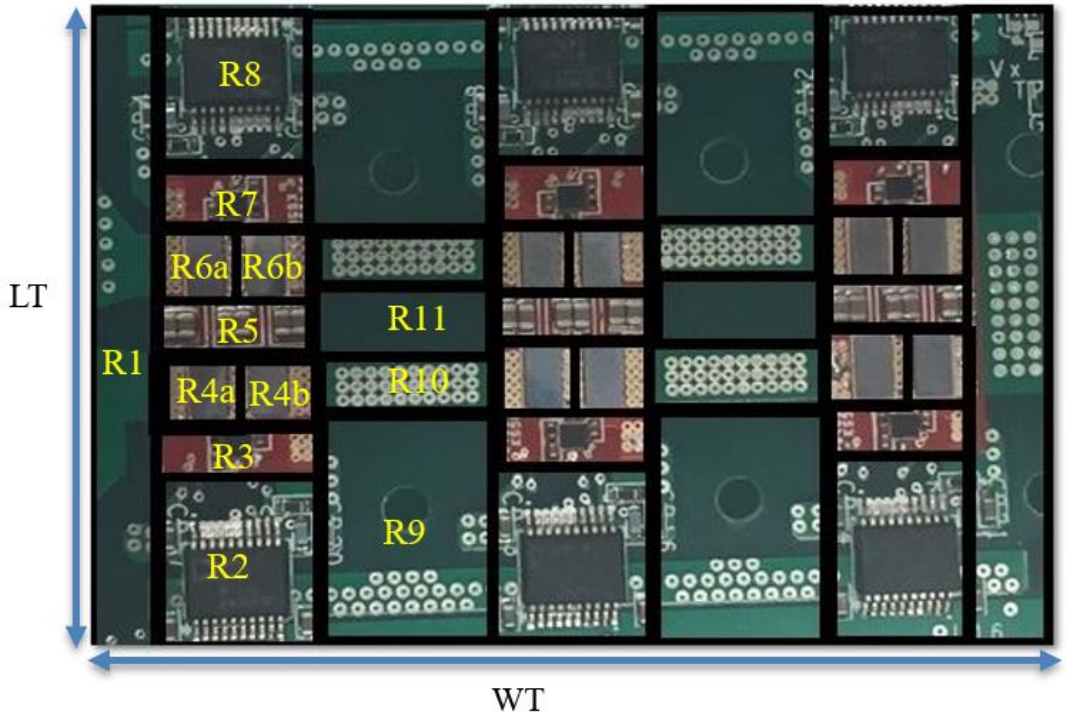

Figure 5.4 Applying labels R1 to R11 to the given inverter grid in order to extract the geometric properties of the pixels.

The conduction resistances along the x and y directions, the convection resistances and the capacitance values of each pixel are calculated according to the formulas presented in chapter 2. Using the 2-dimensional RC thermal model, the dynamic thermal behavior of the multilevel inverter can be modeled in Simscape in SIMULINK as a circuit of capacitors and resistors. Another strategy that can be used to obtain the dynamic thermal behavior of the multilevel inverter using the 2-dimensional RC thermal model is to derive the linear state space thermal model of the inverter by applying the conservation of energy principle on every vertex in the graph-based thermal model of the inverter. This strategy will be presented in the next section. The theoretical dynamic thermal behavior of the inverter obtained from the 2-dimensional RC thermal model will be presented. Furthermore, the Simscape model of the 2-D RC thermal model of the inverter will be shown. Both models, i.e. the Simscape model and the state space model, have the same exact results.

Table 5.1 Dimesions for the inverter regions defined in Figure 5.4.

	(mm)	(mm)
Region #	**Length** (Vertical Dimension)	**Width** (Horizontal Dimension)
Total Board	47.32	67.04
1	47.32	3.73
2	12.86	10.33
3	4.09	10.33
4a	4.60	10.33
4b	4.60	10.33
5	4.12	10.33
6a	4.60	10.33
6b	4.60	10.33
7	4.09	10.33
8	12.86	10.33
9	16.45	13.12
10	4.55	13.12
11	5.34	13.12

Table 5.2 Material properties for FR4 and Copper.

Material	Specific Heat (KJ/g*C)	Thermal Conductivity (W/m*K)	Density (g/cm^3)
Copper	0.385 to 0.4	385 to 390	8.9 to 8.96
FR4	0.6 to 0.95	0.25 to 0.3	1.85 to 1.91

5.2.1 2-D full order RC thermal model results

The dynamic thermal behavior of the multilever inverter shown in the previous section can be obtained by deriving a linear state space thermal model of the system. The linear state space model is derived from a graph-based model that represents the 2-dimensional RC thermal model of the multilevel inverter. Figure 5.5 shows the 2-dimensional graph-based mode of the multilevel inverter. As it is shown in Figure 5.3, the inverter was discretized into 39 pixels. Hence, the graph-based model has 39 vertices. Each vertex represents the thermal capacitance of the corresponding pixel of the inverter. The edges shown in Figure 5.5 represent the conduction resistances along the x and y directions. It should be noted that there is a convection resistance from every vertex of the graph to a voltage source that represents the ambient temperature. These convection resistances are not shown in Figure 5.5 for simplicity. The 12 GaN transistors are the main heat sources in the multilevel level. These components have additional current sources connected to the vertices that represent their thermal capacitance in the graph-based thermal model.

The linear state space model of the multilevel inverter will have 39 states. Each state represents the dynamic temperature profile of a pixel. To derive the state space thermal model of the multilevel inverter the conservation of energy principle is applied on every vertex of the 2-D graph-based thermal model. The conservation of energy principle is as follows.

$$Energy\_stored = Energy\_entering - Energy\_leaving. \tag{5.3}$$

The energy enters a node through conduction in the x or y directions from adjacent nodes or from the current source connected to it. The energy leaves a node either through conduction in the x or y direction to adjacent nodes or through convection to the environment. Equation (5.4) is an example of the conservation of energy applied on vertex 1 in the graph-based thermal model of the multilevel inverter.

$$C_1\dot{T}_1 = \frac{T_2 - T_1}{R_{1,2}} + \frac{T_8 - T_1}{R_{1,8}} + \frac{T_{11} - T_1}{R_{1,11}} + \frac{T_{19} - T_1}{R_{1,19}} + \frac{T_{24} - T_1}{R_{1,24}} + \frac{T_{32} - T_1}{R_{1,32}} + \frac{T_{35} - T_1}{R_{1,35}} - \frac{T_1 - T_a}{R_{c1}}, \tag{5.4}$$

where $R_{i,j}$ represents the conduction resistance between nodes i and j, C_1 represents the thermal capacitance of vertex 1, T_1 represents the temperature of vertex 1, and R_{c1} represents the convection resistance from vertex 1. The full set of equations for the 39 vertices is shown in the appendix.

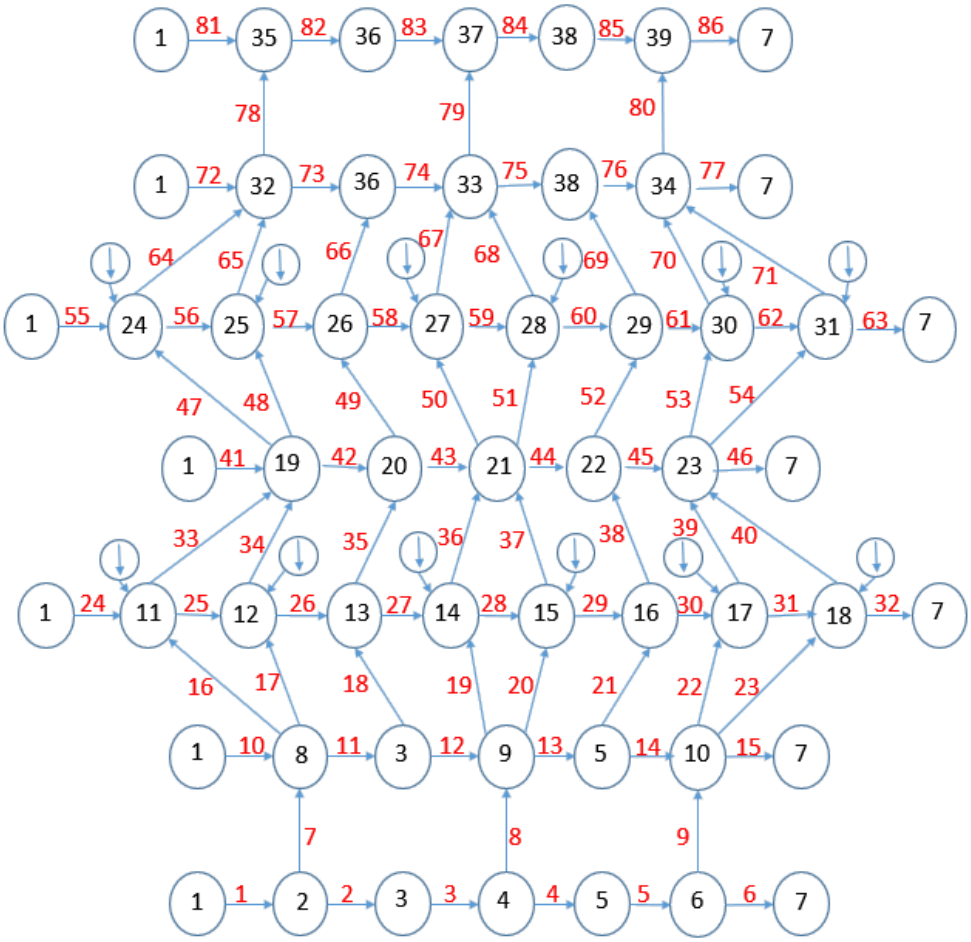

Figure 5.5 2-D graph-based thermal model of the multilevel inverter shown in Figure 5.3. The 39 vertices represent the thermal capacitances of the 39 pixels of the inverter. The edges that connect adjacent vertices represent the conduction resistances in the x and y directions. The convection resistances that connect every vertex of the graph to a voltage source that represents the ambient temperature are not shown in the figure for simplicity. The heat sources that represent the 12 GaN transistors are represented by the 12 current sources in the graph-based model.

Rearranging the terms in the 39 equations of the dynamic thermal behavior of the multilevel inverter, a linear state space model of the form

$$\dot{T} = AT + Bu + VT_a \tag{5.5}$$

is obtained. u represents the heat input generated from the current sources, T represents the temperature of every pixel, and T_a represents the ambient temperature. It should be noted that the ambient temperature represents a disturbance to the system. The dynamic thermal behavior of the full order (39 states) RC thermal model is shown in Figure 5.6. However, 39 is a large number of states if this model is used in a filter. Therefore, a structure-preserving aggregation-based model order reduction technique will be used to reduce the number of states of the full order RC thermal model while preserving its accuracy and structure. Also, it was mentioned in the previous section that the dynamic thermal behavior of the inverter can be obtained by modeling a circuit of capacitors and resistors in Simscape in Simulink. Figure 5.7 shows the 2-dimensional RC thermal model of the multilevel inverter modeled in Simscape in Simulink. The figure shows how the first row of the inverter that was discretized into 7 pixels is represented by 7 capacitors in the RC thermal model. The capacitors are connected in the x and y directions through conduction resistances. Also, every capacitor is connected to a voltage source through a resistor that represents the ambient temperature.

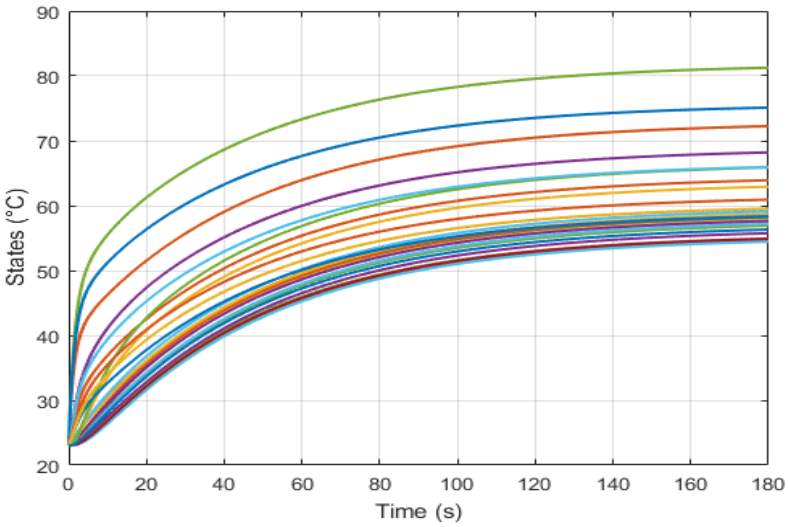

Figure 5.6 Dynamic thermal behavior of the full order RC thermal model (39 states).

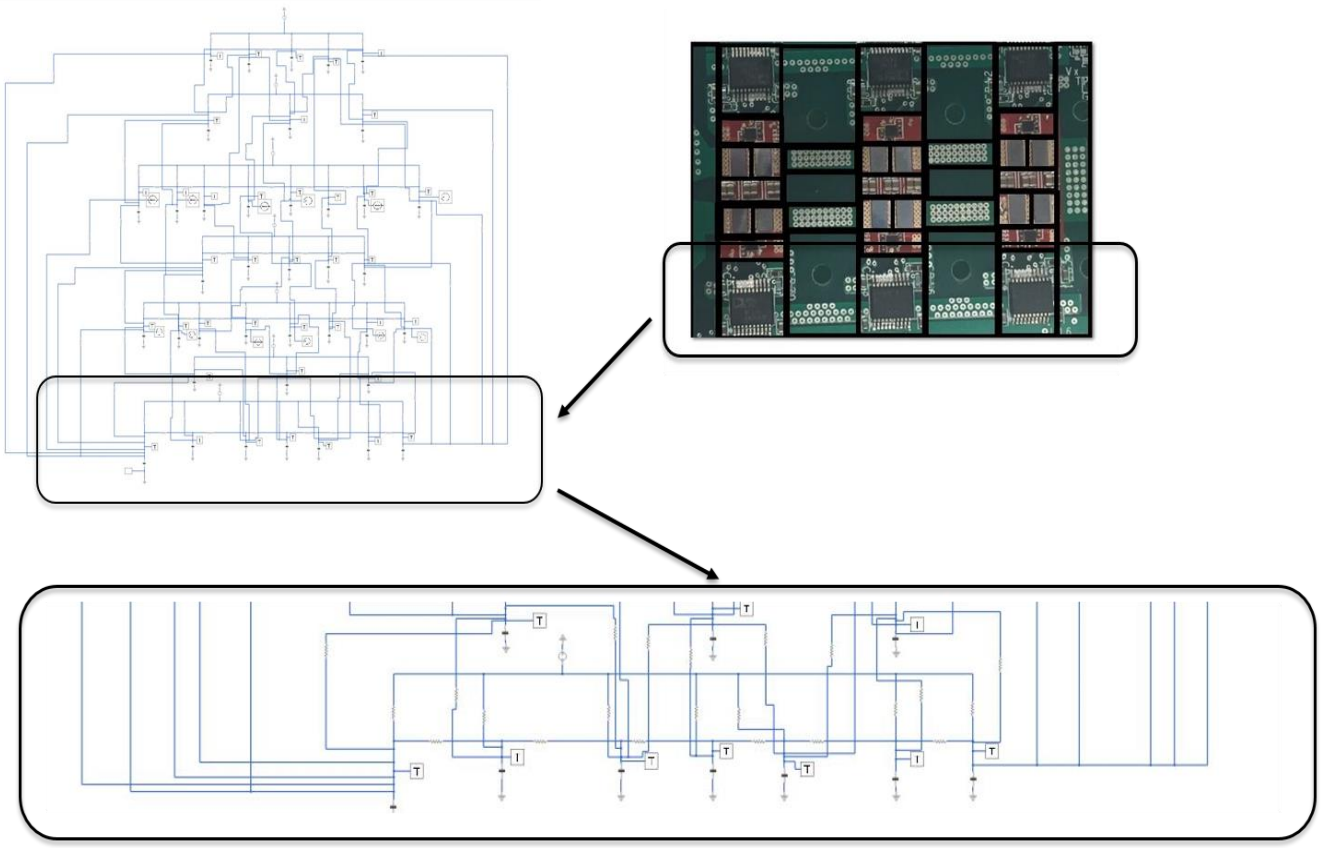

Figure 5.7 Modeling the 2-dimensional RC thermal model in Simscape in Simulink.The thermal model is modeled as a circuit of resistors and capacitors. The inverter is discretized into 39 pixels. Hence, the RC circuit is composed of 39 capacitors. The spatially adjacent capacitors are connected in the x directions through resistances that represent conduction resistance in the x directions. Also, the spatially adjacent capacitors are connected in the y direction through resistances that represent conduction resistance in the y direction. Every capacitor is connected to a voltage source that represents the ambient temperature through a convection resistance.

5.3 2-D reduced order RC thermal model

The model order reduction technique used to reduce the number of capacitors in the full order 2-dimensional RC thermal model is the structure preserving aggregation-based model order reduction technique presented in chapter 3. The first step of the algorithm of this method is to assign a sign to every vertex in the graph-based thermal model of the system according to the sign structure of the second eigenvector of the symmetric matrix $\hat{P}$. The spatially adjacent nodes that share the same sign can be aggregated together into super-nodes. The aggregation structure is specified by the user if the spatially adjacent nodes share the same sign. Table 5.3 shows the sign structure of the second eigenvector of the $\hat{P}$ matrix. Figure 5.8 shows the 2-dimensional full order graph-based thermal model of the multilevel inverter with a sign assigned to every vertex in the graph according to the sign structure of the second eigenvector of the $\hat{P}$ matrix. The red vertices share the negative sign and the white vertices share the positive sign. Figure 5.9 shows the 2-dimensional reduced order graph-based thermal model of the multilevel inverter. The 39 nodes of the full order RC thermal model were aggregated into 9 super-nodes in the reduced order RC thermal model. The main advantage of this aggregation-based model order reduction technique is that it preserves the physical correspondence between the original full order system and the reduced order model. More specifically, the reduced order model is still a RC thermal model. Each super-node represents the thermal capacitance of a specific portion of the multilevel inverter. Furthermore, the reduced order RC thermal model can still simulate the dynamic thermal behavior of the multilevel inverter with good accuracy. Figures 5.10-5.14 show the states of the reduced order RC thermal model (super-nodes) versus their corresponding states in the full order RC thermal model. It can be seen that, the error between the super-nodes of the reduced order thermal model and their corresponding nodes in the full order thermal model is less than 3^{o}C.

Therefore, using this aggregation-based model order reduction technique, the complexity of the RC thermal model was reduced from 39 states in the full order RC thermal model to 9 states in the reduced order RC thermal model while preserving the accuracy of the thermal model and the physical meaning of the states in the reduced order thermal model.

The next step is to estimate the dynamic thermal behavior of the multilevel inverter from the reduced order RC thermal model using an optimal number and an optimal placement of temperature sensors in a continuous-discrete Kalman filter.

Table 5.3 The sign structure of the second eigenvector of the $\hat{P}$ matrix. Each vertex of the 2-D full order thermal network will be assigned a sign accordingly.

1	-0.01086	21	0.311361
2	-0.0186	22	0.568512
3	-0.03063	23	0.113749
4	-0.05283	24	0.068634
5	-0.07079	25	0.068642
6	-0.08474	26	-0.02265
7	-0.08273	27	0.158162
8	0.069911	28	0.158157
9	0.160387	29	-0.06227
10	0.024707	30	0.009841
11	0.069924	31	0.009828
12	0.069933	32	0.068619
13	-0.01858	33	0.158127
14	0.160421	34	0.009812
15	0.160417	35	-0.02037
16	-0.05705	36	-0.0349
17	0.02473	37	-0.05814
18	0.024715	38	-0.0759
19	0.159179	39	-0.08709
20	0.555742		

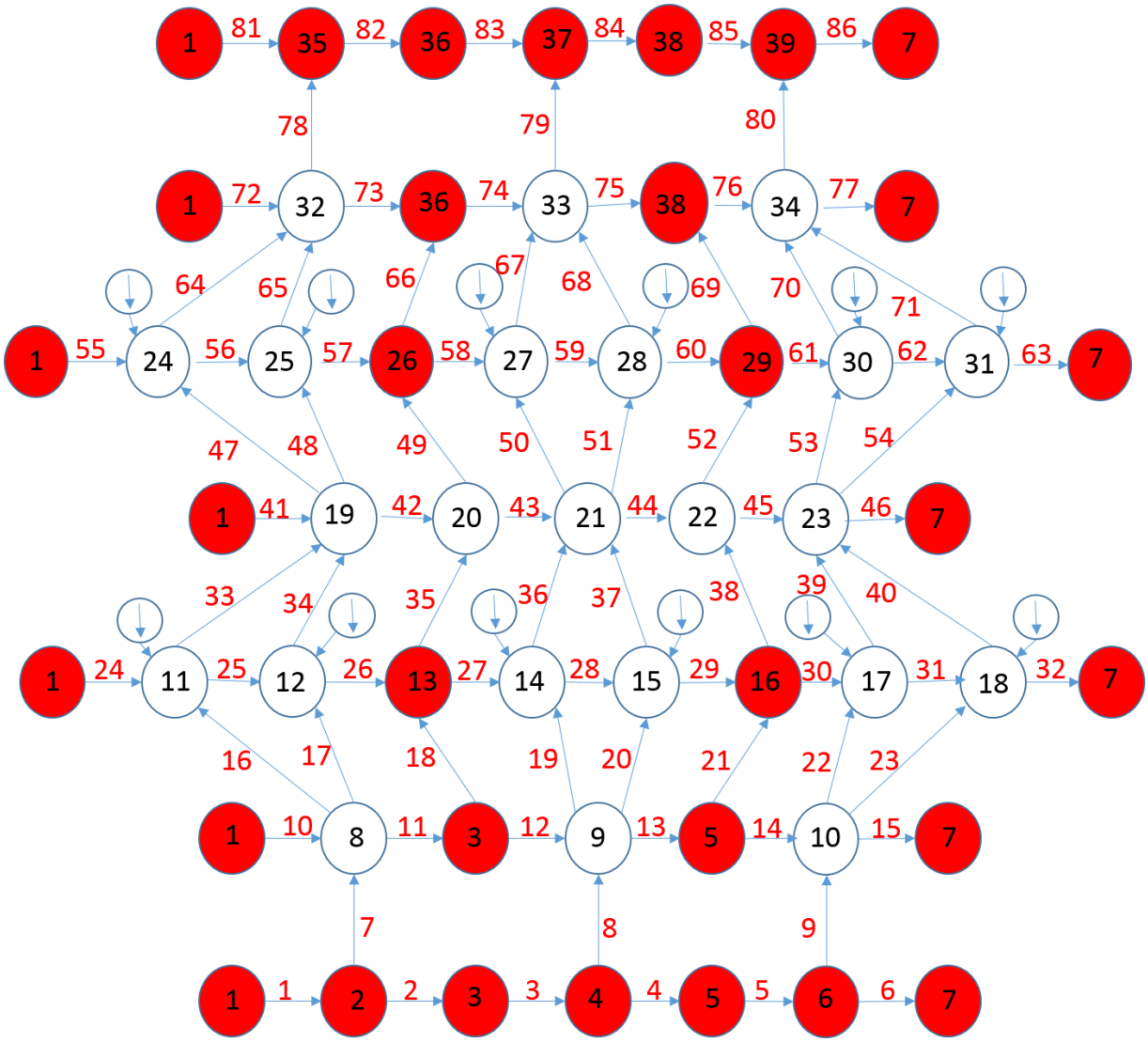

Figure 5.8 The 2-dimensional full order graph-based thermal model of the multilevel inverter with a sign assigned to every vertex according to the sign structure of the second eigenvector of the $\hat{P}$ matrix. The red vertices share a negative sign and the white vertices share a positive sign. The spatially adjacent nodes that share the same sign can be aggregated together into super-nodes.

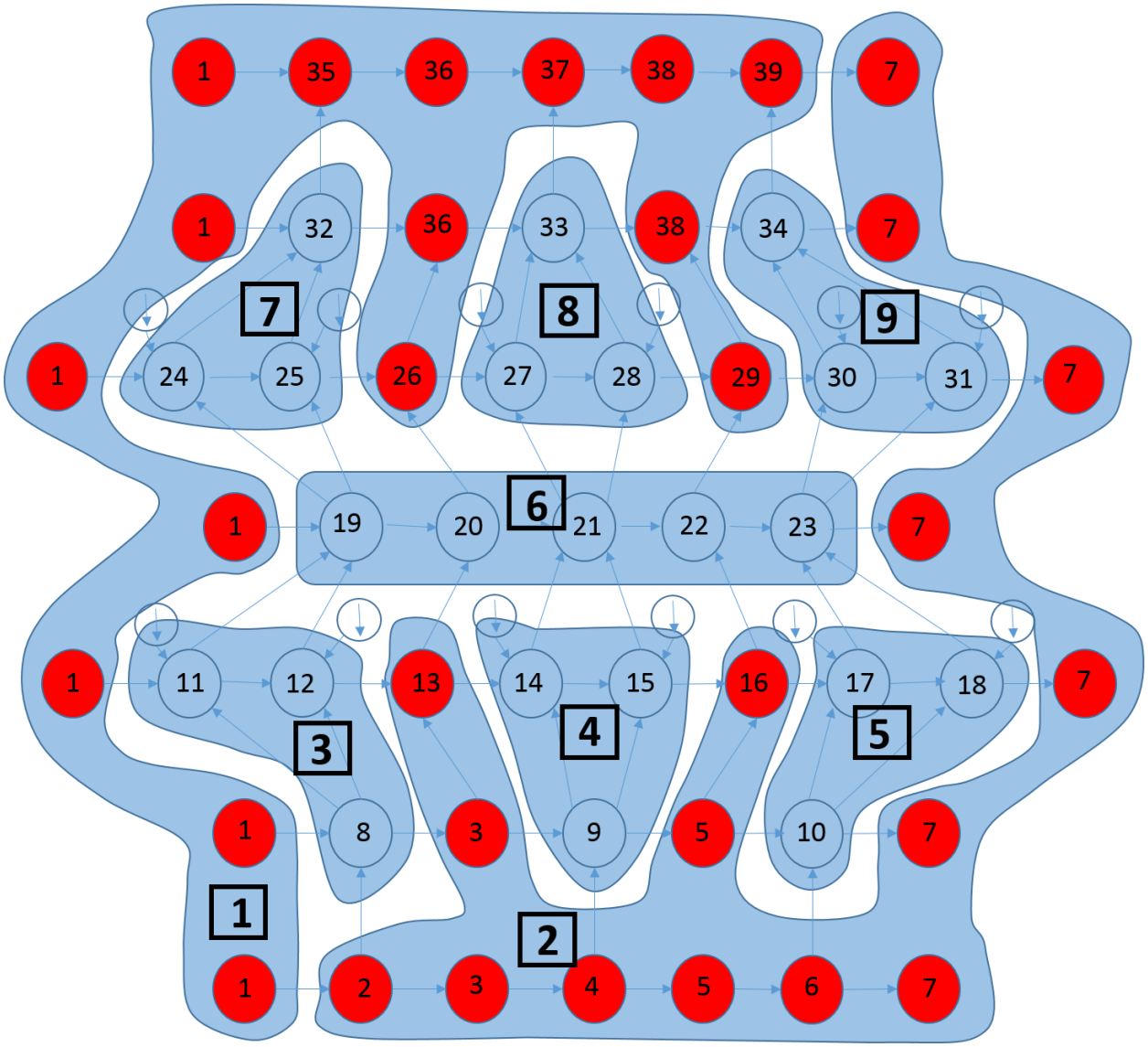

Figure 5.9 The 2-dimensional reduced order graph-based thermal model of the multilevel inverter. The 39 nodes of the full order RC thermal model were aggregated into 9 super-nodes in the reduced order RC thermal model. Each super-node represents a specific portion of the inverter.

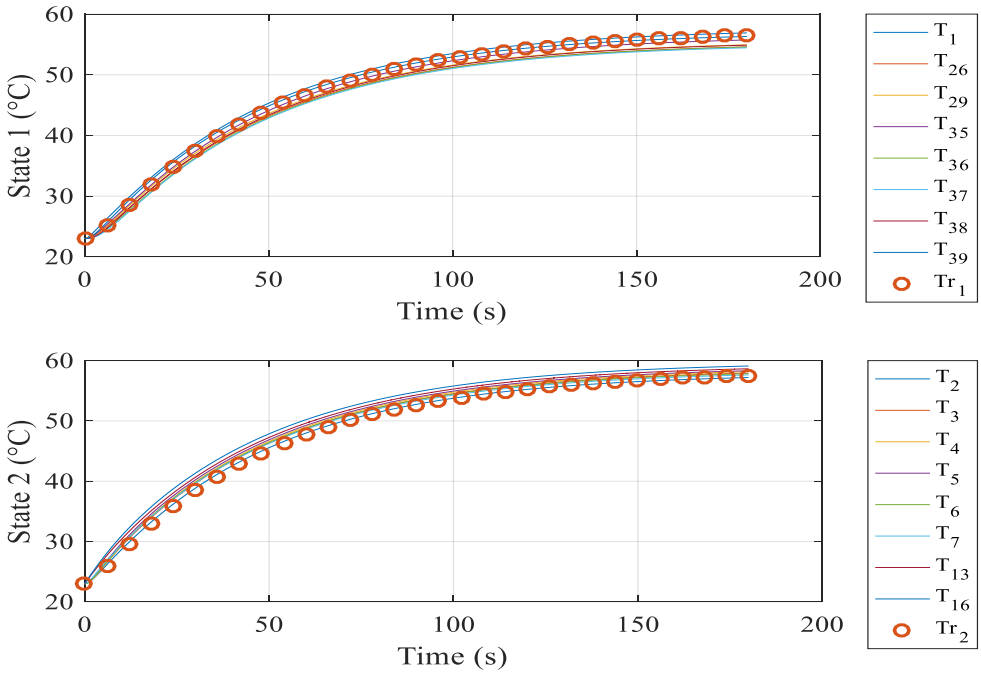

Figure 5.10 First and second states of the reduced order RC thermal model vs their corresponding states in the full order RC thermal model.

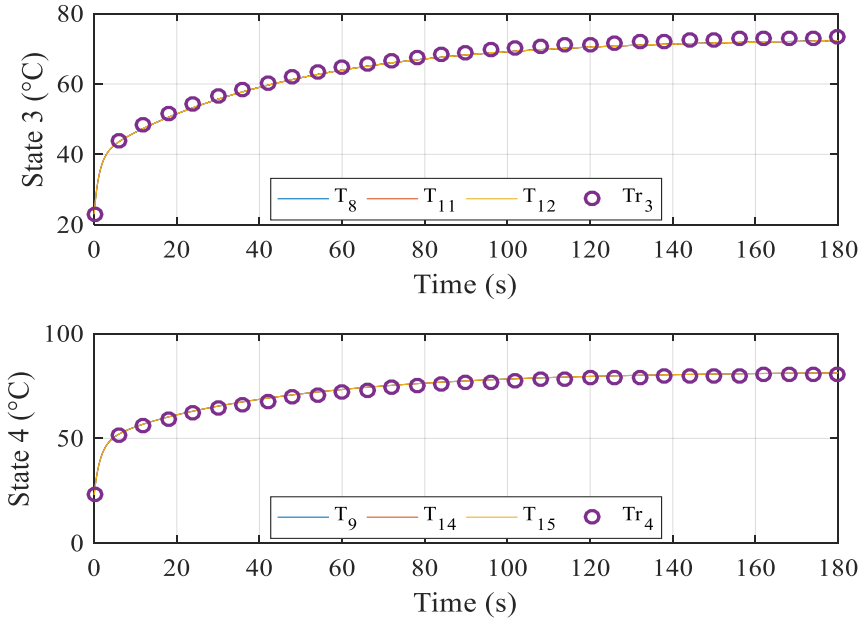

Figure 5.11 Third and fourth states of the reduced order RC thermal model vs their corresponding states in the full order RC thermal model.

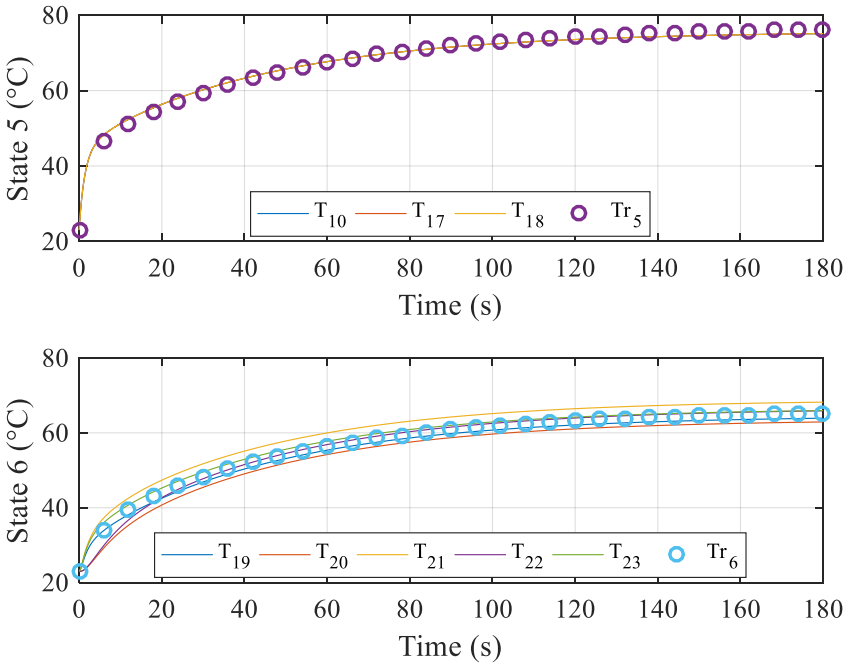

Figure 5.12 Fifth and sixth states of the reduced order RC thermal model vs their corresponding states in the full order RC thermal model.

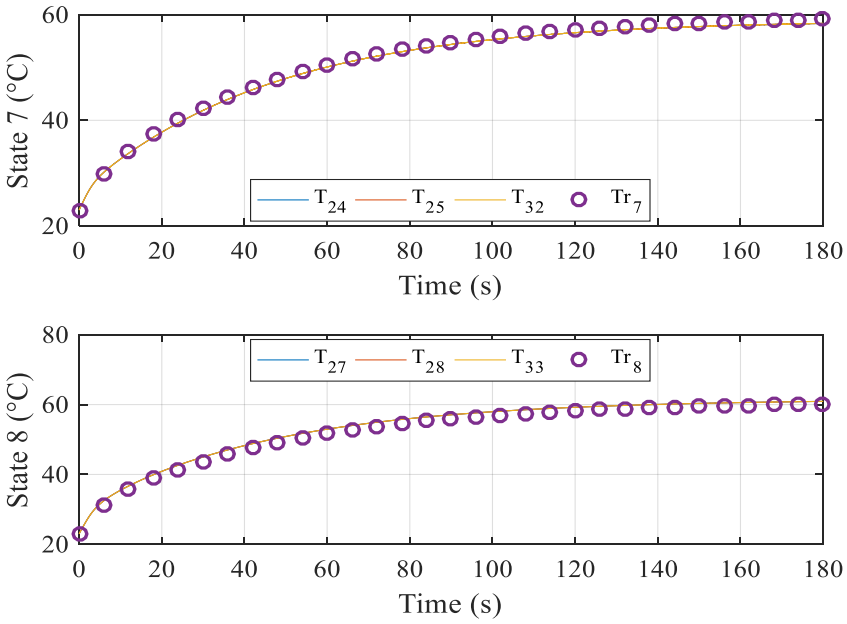

Figure 5.13 Seventh and eighth states of the reduced order RC thermal model vs their corresponding states in the full order RC thermal model.

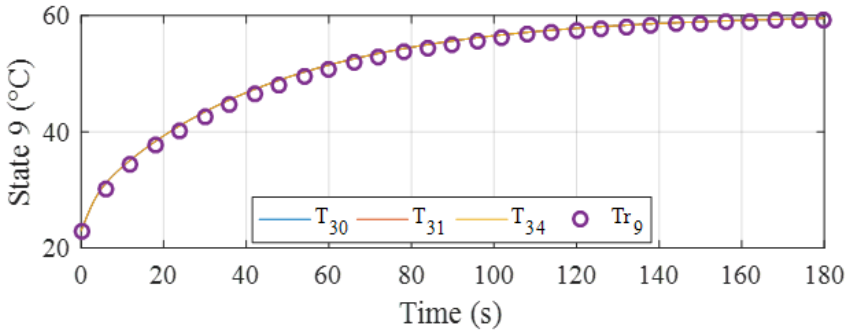

Figure 5.14 Ninth state of the reduced order RC thermal model vs its corresponding states in the full order RC thermal model.

5.4 Sensor placement optimization

Finding the optimal number and the optimal placement of the temperature sensors that should be used in the continuous-discrete Kalman filter is an essential task of the dynamic thermal estimation technique. Reducing the number of sensors in the power electronics system reduces its cost, increases its reliability, and prevents packaging problems.

The optimal placement of temperature sensors was found using two information-based performance metrics: the observability Gramian condition number and the observability Gramian trace. Maximizing the trace of the observability Gramian or minimizing the observability Gramian condition number result in the optimal placement for a specific number of temperature sensors. However, measures based on Gramian condition number are limited in their ability to get information from the entire range of states of the system. The trace of the observability Gramian metric does not have this limitation.

Since the super-nodes of the reduced order thermal model have a physical meaning, placing sensors on the states of the reduced order model is equivalent to placing sensors on specific components in the inverter. This is the main advantage of using a structure-preserving model order reduction technique. Tables 5.4 and 5.5 show the optimal sensor locations in the reduced order model using the trace of the observability Gramian and the logarithm of the condition number of the observability Gramian as a trade-off respectively.

Table 5.4 Optimal sensor locations for the reduced order RC thermal model using the trace of the observability Gramian as a trade-off.

Number of sensors	State Locations	Trace of Obs. Gramian Matrix
1	1	10.0148
2	1,2	20.029
3	1,2,6	27.1776
4	1,2,6,7	34.0721
5	1,2,5,6,7	40.9665
6	1,2,3,5,6,7	47.7939
7	1,2,3,5,6,7,9	54.6079
8	1,2,3,5,6,7,8,9	61.1881
9	1,2,3,4,5,6,7,8,9	67.7681

Table 5.5 Optimal sensor locations for the reduced order RC thermal model using the logarithm of the condition number of the observability Gramian matrix as trade-off.

Number of sensors	State Locations	Cond. Number of Obs. Gramian Matrix
1	9	41.8178
2	3,5,	22.8861
3	3,5,7	17.1946
4	3,5,8,9	15.7651
5	3,4,5,7,9	11.2315
6	3,4,5,7,8,9	5.8806
7	1,3,4,5,7,8,9	5.3285
8	2,3,4,5,6,7,8,9	4.8737
9	1,2,3,4,5,6,7,8,9	4.7171

The performance of these two metrics will be compared in the next section using the Kalman filter. The best metric will be used to place the sensors on the inverter. Furthermore, using these two metrics, only the optimal placement of the temperature sensors can be found. To find the optimal number of temperature sensors that should be used, the estimated states of the reduced order thermal model obtained from the Kalman filter will be compared to the actual states of the reduced order thermal model obtained from the reduced order RC model. This analysis will be shown in the next section.

5.5 Continuous-discrete Kalman filter

As it was shown in chapter 4, the Kalman filter is an optimal estimator for linear systems in the case of white noise. Also, the dynamic thermal model of the inverter is represented by a linear time-invariant state space model. Hence, a continuous-discrete Kalman filter in which the RC thermal model is continuously changing in time and the sensor measurements are obtained at discrete instants in time will be used to reconstruct the dynamic thermal behavior of the multilevel inverter using an optimal number of sensors placed at the optimal locations.

In the previous section, the optimal sensor placement was found using two metrics: the trace of the observability Gramian and the condition number of the observability Gramian. The performance of these two metrics is compared based on the estimation error obtained from the Kalman filter. Figures 5.15 and 5.16 show the estimation error of the 9 states of the reduced order RC thermal model using the trace of observability Gramian and the condition number of observability Gramian, respectively, to place 5 sensors at the optimal locations on the inverter. It can be seen that the absolute value of the maximum state estimation error is 1^{o}C using the trace of observability Gramian to place the sensors, whereas it is around 2^{o}C when the condition number of the observability Gramian is used to place the 5 sensors on the inverter. Hence, in this work the optimal locations of the temperature sensors will be found using the trace of the observability Gramian as an information-based performance metric.

Furthermore, the optimal number of temperature sensors is found based on the state estimation error obtained from the Kalman filter. Figure 5.17 shows the sum of the absolute value of the state estimation error of the reduced order thermal model versus the number of

temperature sensors used. It can be seen that adding more than 5 temperature sensors in the system does not reduce the estimation error further since it is only related to the sensor noise at this number of sensors. Hence, it can be deduced that 5 is the optimal number of temperature sensors that should be used in this power electronics system. The optimal placement of the 5 sensors is on super-nodes 1,2,5,6, and 7 according to the trace of the observability Gramian. However, each super-node represents a large area of the physical system, i.e. several components of the inverter. Therefore, in order to obtain the exact locations of the temperature sensors on the inverter, an optimal sensor placement problem for the full order RC thermal model using the trace of the observability Gramian as an information-based performance metric was solved. Table 5.6 shows the optimal sensor placement for the full order RC thermal model using the trace of the observability Gramian as a trade-off. Using that table, the optimal locations of the 5 sensors in the full order thermal model can be found by checking the redundancy of the states of the full order RC thermal model that correspond to the optimal locations in the reduced order RC thermal model in that table [64].

Using 5 sensors at the optimal locations in the inverter, the dynamic thermal behavior of the power electronics system was accurately reconstructed using the continuous-discrete Kalman filter. Figures 5.18-5.22 show the theoretical (RC model) versus the estimated (Kalman filter) values of the states of the reduced order thermal model. These plots show that the Kalman filter was able to track the dynamic thermal behavior of the board accurately.

It was shown that the 9 states of the reduced order RC thermal model were accurately estimated using the Kalman filter. However, the ultimate goal of the proposed dynamic thermal estimation technique is to reconstruct the dynamic thermal behavior of the full order RC thermal model since full order models are usually more accurate than reduced order models. Therefore, the estimated dynamic thermal behavior of the reduced order RC thermal model was compared to the dynamic thermal behavior of the full order RC thermal model. Figures 5.23-5.27 show the estimated values of the 9 states of the reduced order RC thermal model obtained from the Kalman filter versus their corresponding theoretical equivalent states in the full order model obtained from the RC model. The estimation error in these plots was less than 3^{o}C. Hence, by comparing the estimated states of the reduced order model to the states of the full order model, the estimation error was slightly higher than when they were compared to the

theoretical states of the reduced order thermal model. However, this result was expected since there is originally a small error between the states of the reduced order model and the states of the full order model.

All these results are theoretical, i.e. obtained from the RC thermal model and the Kalman filter. The experimental validation of the reduced order RC thermal model will be presented in the next section.

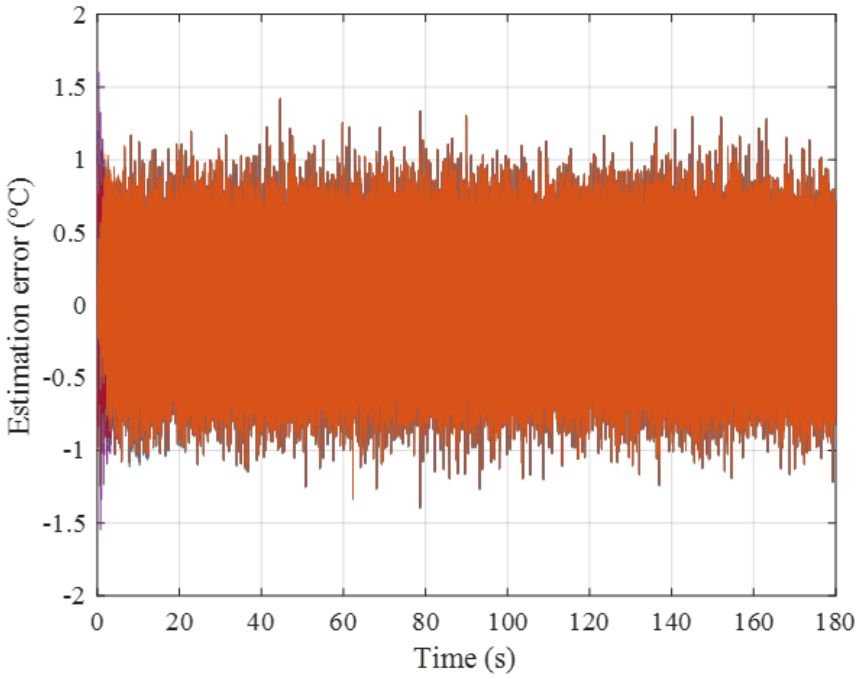

Figure 5.15 Estimation error of the 9-state reduced order RC model using the trace of observability Gramian to place 5 temperature sensors at the optimal locations.

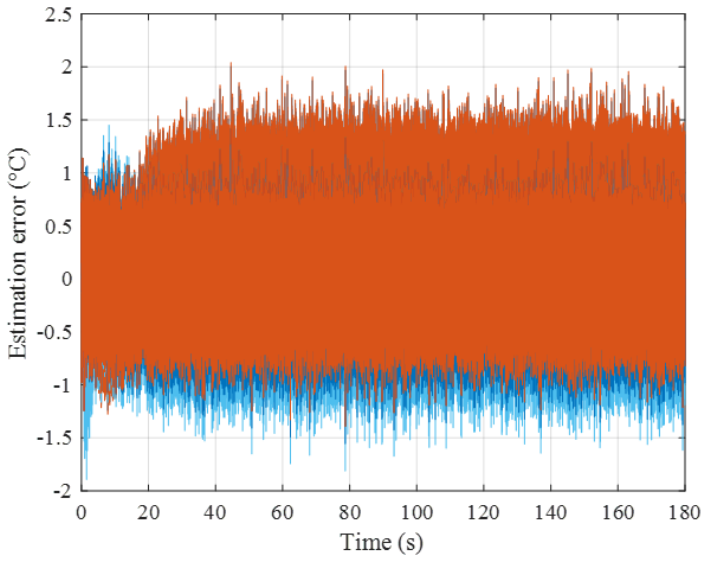

Figure 5.16 Estimation error of the 9-state reduced order RC model using the condition number of observability Gramian to place 5 temperature sensors at the optimal locations.

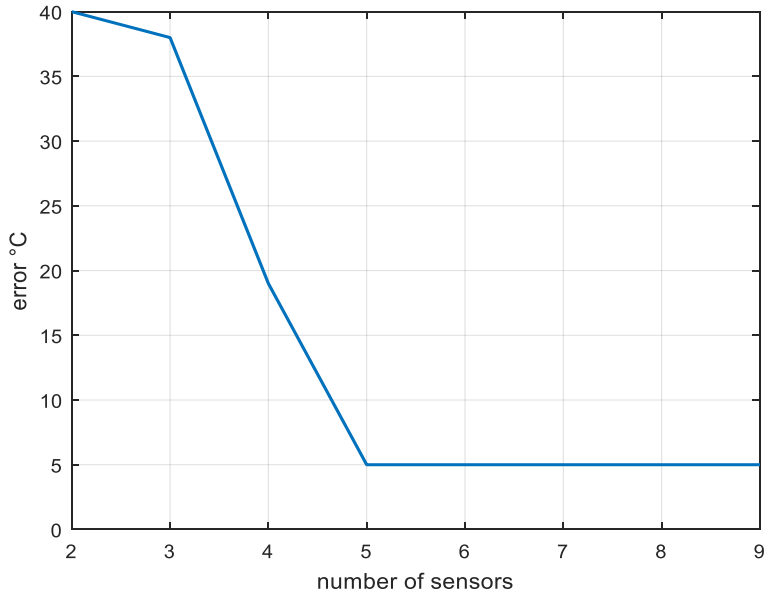

Figure 5.17 Sum of the absolute value of the state estimation error of the reduced order thermal model vs the number of temperature sensors used.

Table 5.6 Optimal sensor locations for the full order RC thermal model using the trace of the observability Gramian matrix as trade-off.

Number of sensors	Sensor Locations
1	3
2	5,38
3	5,20,22
4	3,4,20,22
5	4,5,20,37,38
6	3,5,22,36,37,38
7	3,4,5,16,20,22,36
8	2,7,13,20,22,29,36,37
9	1,4,13,16,22,29,35-37
10	1,3-5,13,20,22,26,36,37
11	2-5,16,20,22,29,36-38
12	2,5,13,16,19,20,22,26,35-39
13	3-6,13,16,20,22,26,36-39
14	2-5,7,13,20,22,26,29,35-38
15	1-6,13,16,20,22,26,35-38
16	1-6,8,13,19,20,22,35-39
17	1-7,13,16,20,22,26,29,36-39
18	1-5,8,11,13,16,20,22,26,29,35-39
19	1-6,13,16,19,20,22,26,29,31,35-39
20	1-5,7,8,12,16,20,22,23,25,26,29,35-39
21	1-8,12,13,16,20,22-24,26,29,35,37-39
22	1-7,11,13,16,19,20,22,23,26,29,34-39
23	1-8,13,16,19,20,22,23,26,29,31,32,35-39
24	1-8,11-13,16,17,19,20,22,26,29,32,35-39
25	1-7,11,13,16,20-23,25,26,29-32,35-39
26	1-8,11-14,16,19,20,22,23,25,26,2932,35-39
27	1-8,11-13,16,19,20,22-26,29,31,32,35-39

Table 5.6 (cont.)

28	1-9,12,13,16,17,19,20,22-26,29,32,34-39
29	1-8,11-13,15,16,19,20,22,23,25,26,29,30,32-39
30	1-8,11-13,16,19-23,25,26,29-39
31	1-8,11-14,16,19,20,22-26,29-39
32	1-8,11-13,15,16,19-32,35-39
33	1-8,11-13,16,18-32,34-39
34	1-9,11-13,15-17,19,20,22-27,29-39
35	1-39 (except 10,15,17,33)
36	1-39 (except 10,15,18)
37	1-39 (except 14 & 17)
38	1-39 (except 10)
39	1-39

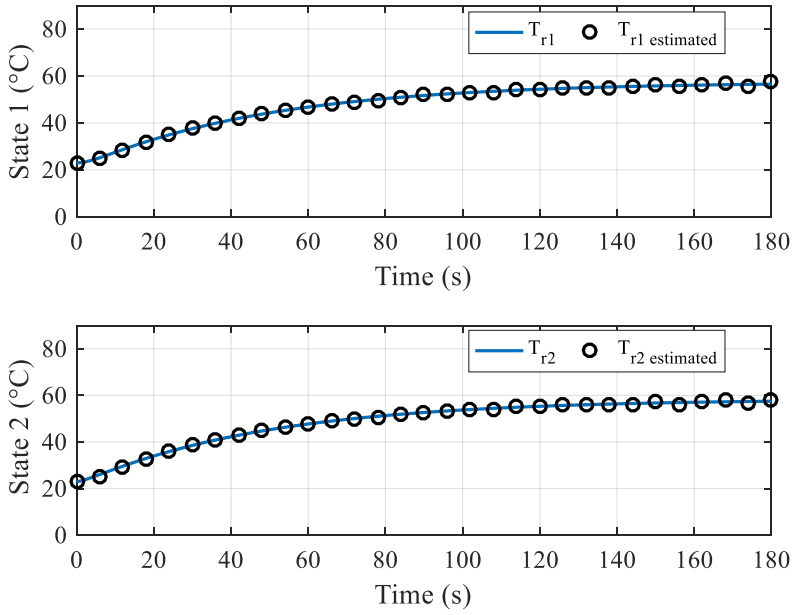

Figure 5.18 Theoretical (RC model) vs estimated (Kalman filter) values of the first and second states of the reduced order model.

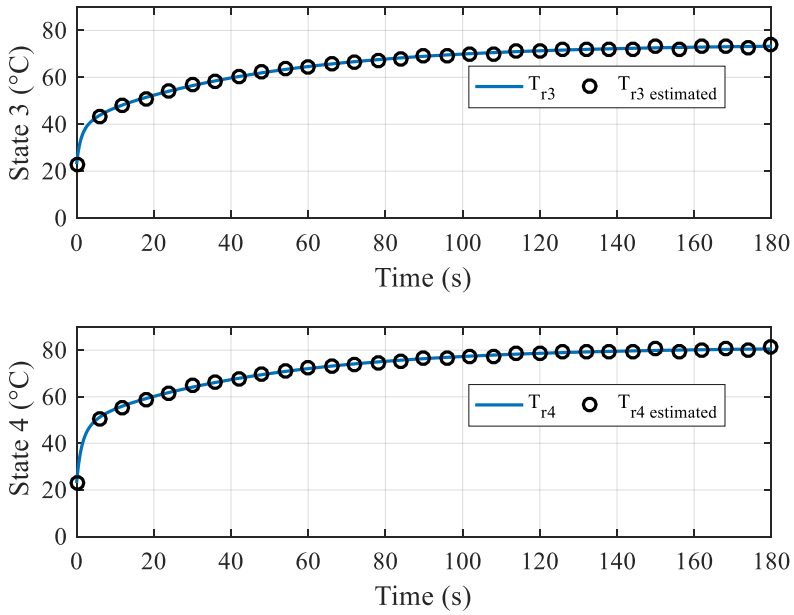

Figure 5.19 Theoretical (RC model) vs estimated (Kalman filter) values of the third and fourth states of the reduced order model.

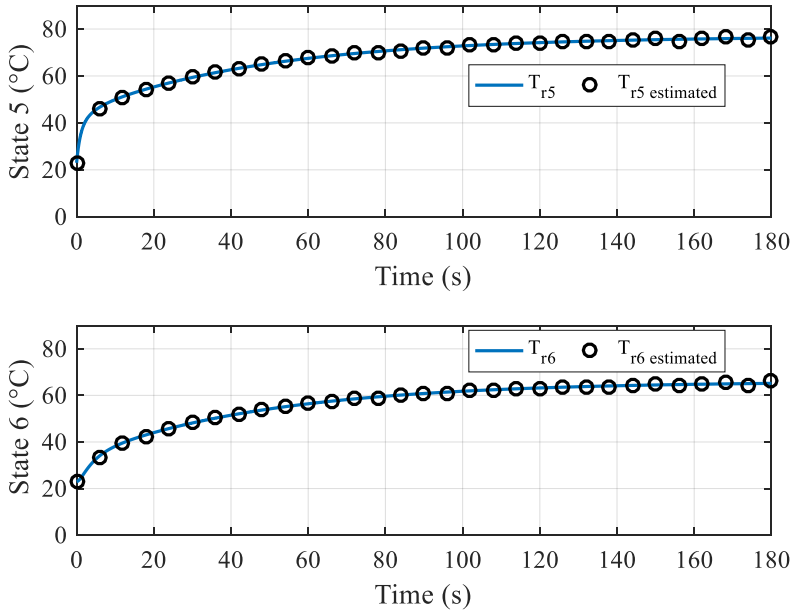

Figure 5.20 Theoretical (RC model) vs estimated (Kalman filter) values of the fifth and sixth states of the reduced order model.

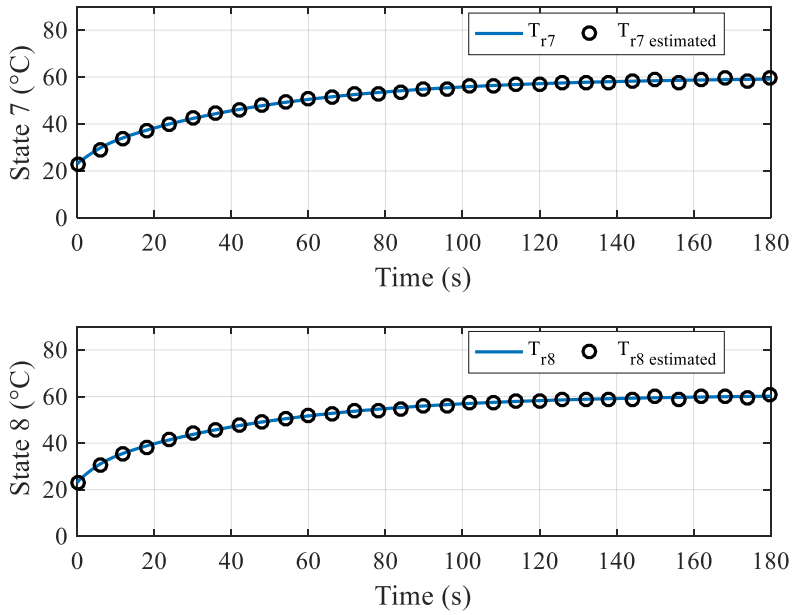

Figure 5.21 Theoretical (RC model) vs estimated (Kalman filter) values of the seventh and eighth states of the reduced order model.

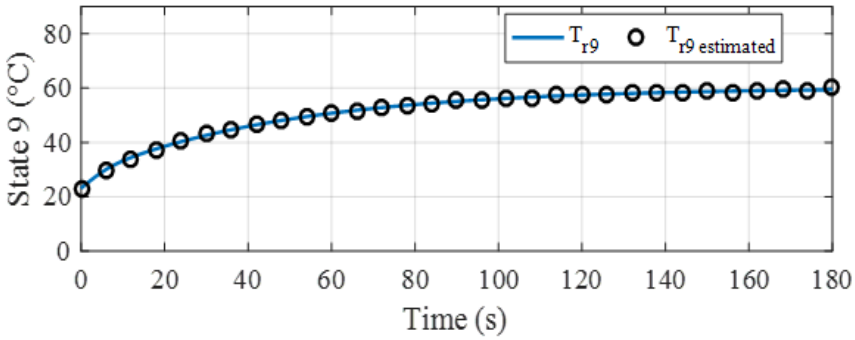

Figure 5.22 Theoretical (RC model) vs estimated (Kalman filter) values of the ninth state of the reduced order model.

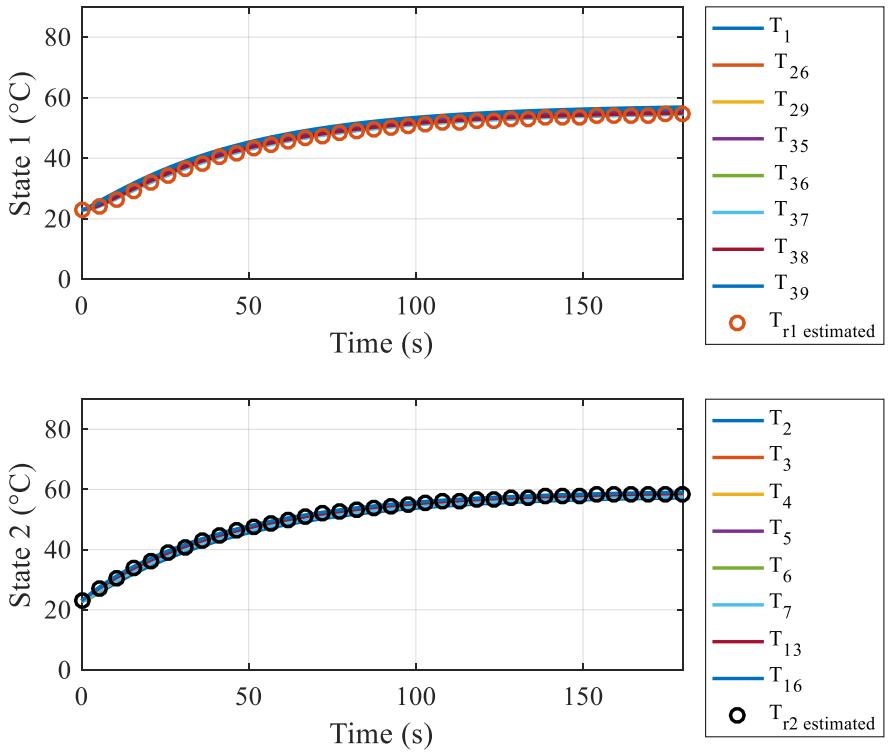

Figure 5.23 Estimated values of the first and second states of the reduced order model (Kalman filter) vs their corresponding theoretical equivalent states in the full order model (RC model).

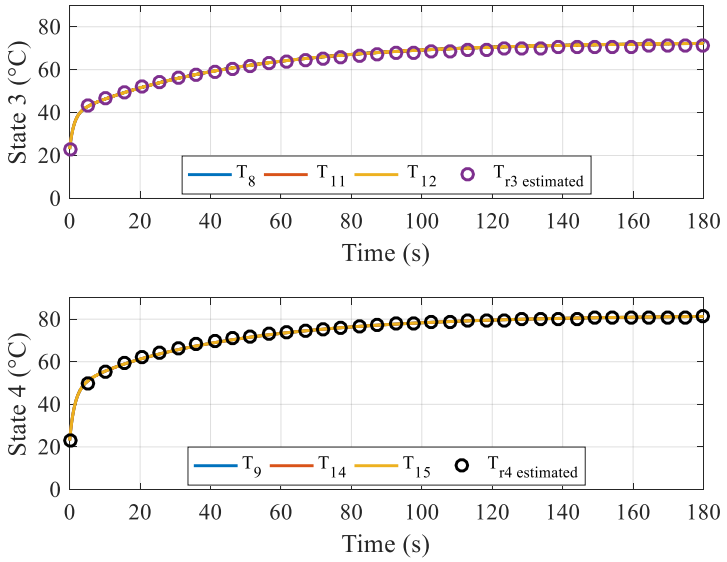

Figure 5.24 Estimated values of the third and fourth states of the reduced order model (Kalman filter) vs their corresponding theoretical equivalent states in the full order model (RC model).

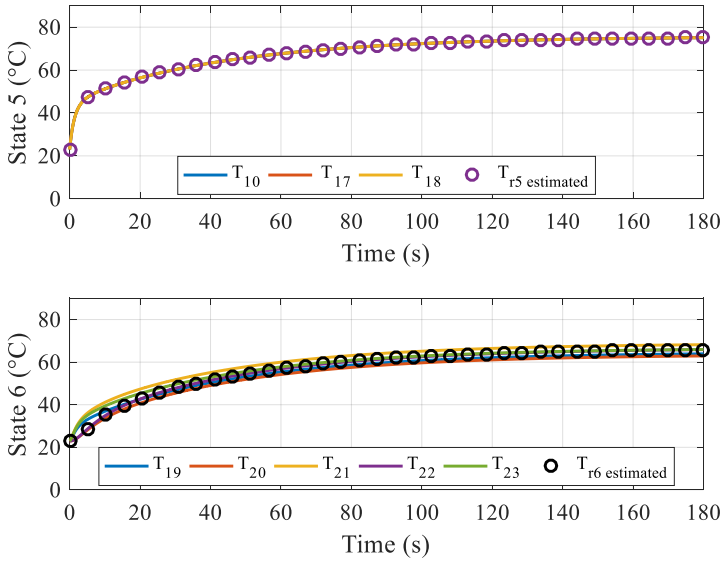

Figure 5.25 Estimated values of the fifth and sixth states of the reduced order model (Kalman filter) vs their corresponding theoretical equivalent states in the full order model (RC model).

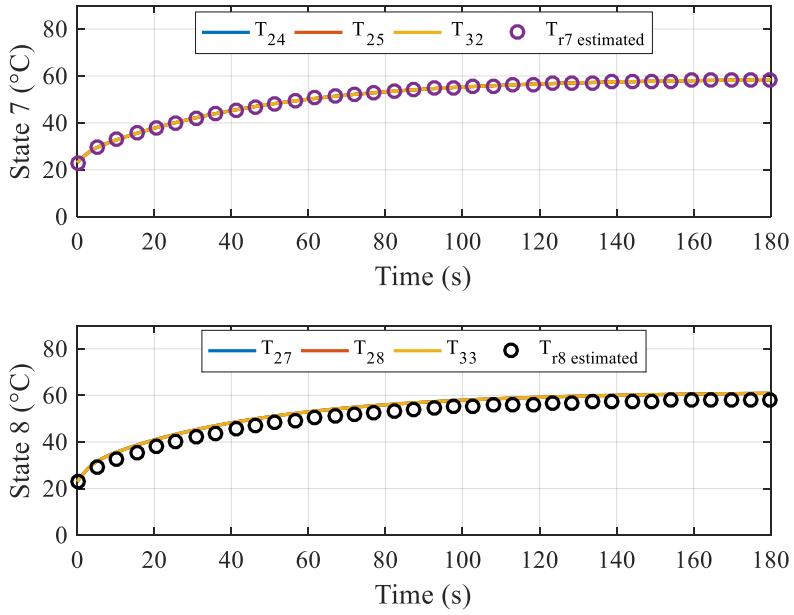

Figure 5.26 Estimated values of the seventh and eighth states of the reduced order model (Kalman filter) vs their corresponding theoretical equivalent states in the full order model (RC model).

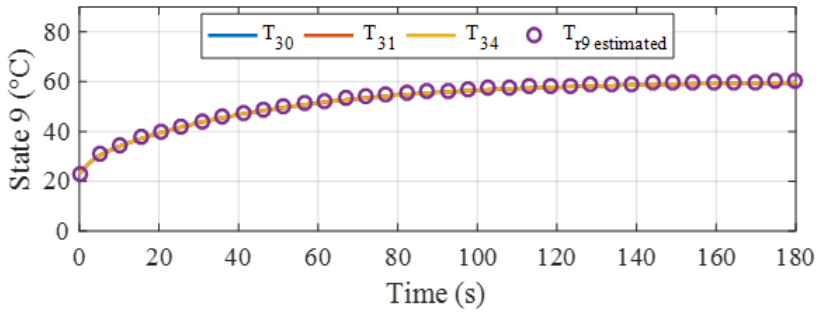

Figure 5.27 Estimated values of the ninth state of the reduced order model (Kalman filter) vs its corresponding theoretical equivalent states in the full order model (RC model).

5.6 Experimental validation

The dynamic thermal behavior of the 2-dimensional RC thermal model was validated experimentally using an IR thermal video of the multilevel inverter. The thermal video was

taken using a FLIR T420 IR camera. Figure 5.28 represents a snapshot from the thermal video at 2 minutes and 58 seconds after a voltage of 200 V was applied to the inverter. The temperature scale in Figure 5.28 is in ^{o}C. The ambient temperature was 23^{o}C. Figures 5.29-5.33 show the theoretical results versus the experimental results of the 9 states of the reduced order RC thermal model. Experimental results are within an error of +/- 5^{o}C. It can be seen that theoretical results match with the experimental results. Hence, the proposed dynamic thermal estimation technique can be used to estimate the dynamic temperature profile of the power electronics system using a small number of temperature sensors placed at some specific locations in the system.

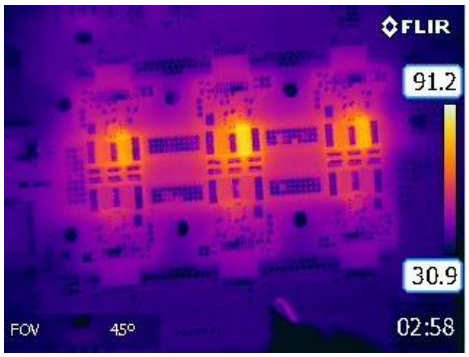

Figure 5.28 Snapshot from IR measurement of operating multilevel inverter.

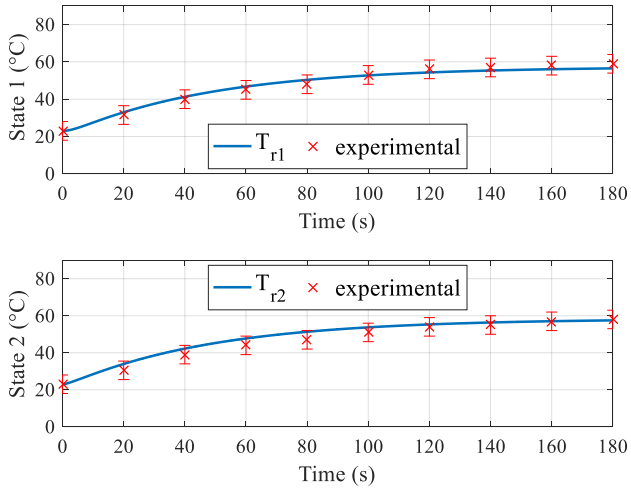

Figure 5.29 Theoretical results (RC model) vs experimental results (IR thermal video) of the first and second states of the reduced order thermal model.

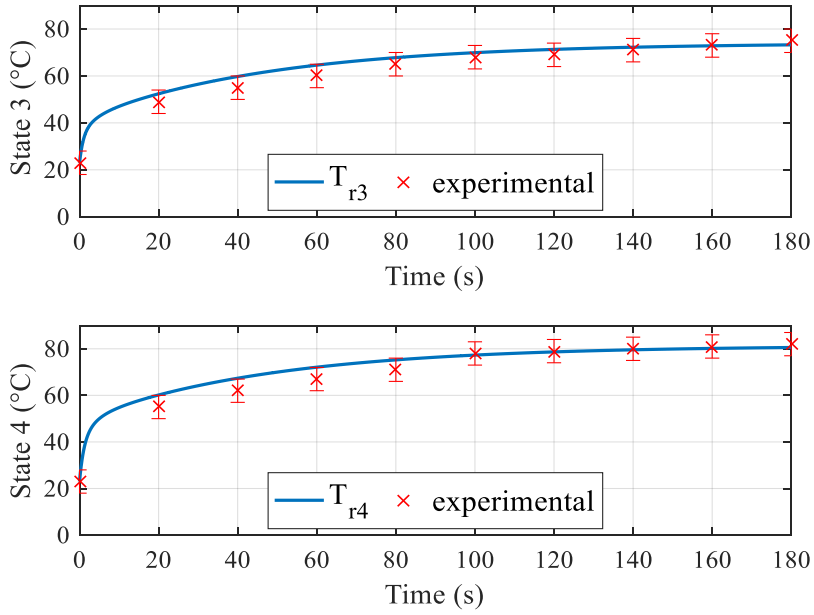

Figure 5.30 Theoretical results (RC model) vs experimental results (IR thermal video) of the third and fourth states of the reduced order thermal model.

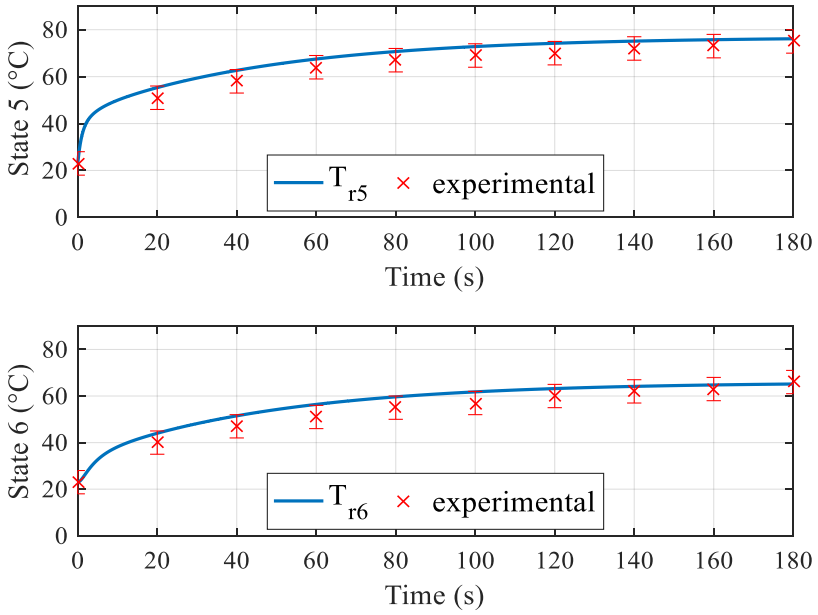

Figure 5.31 Theoretical results (RC model) vs experimental results (IR thermal video) of the fifth and sixth states of the reduced order thermal model.

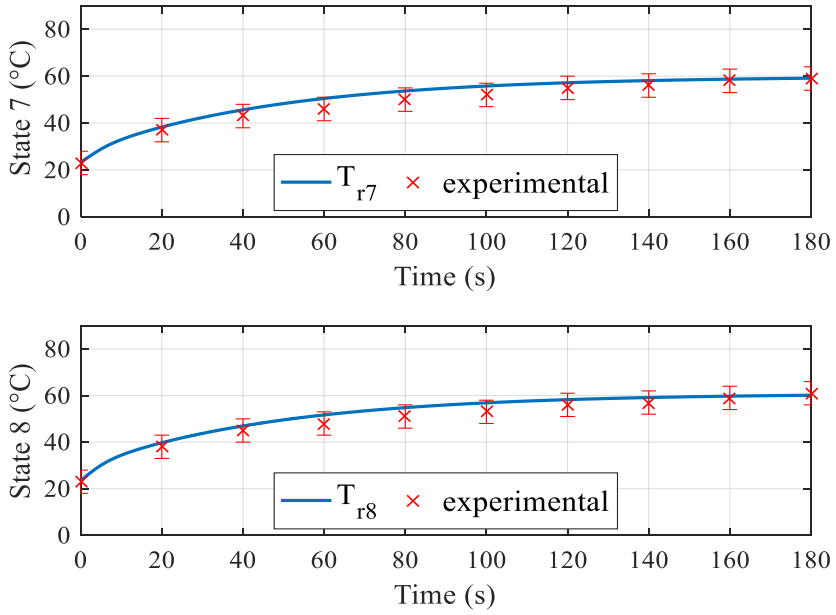

Figure 5.32 Theoretical results (RC model) vs experimental results (IR thermal video) of the seventh and eighth states of the reduced order thermal model.

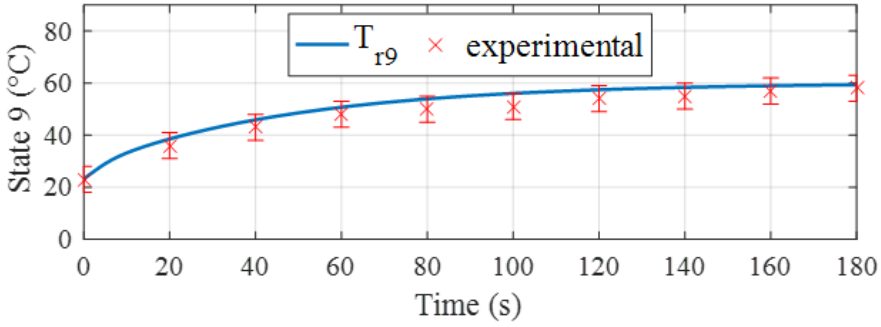

Figure 5.33 Theoretical results (RC model) vs experimental results (IR thermal video) of the ninth state of the reduced order thermal model.

Chapter 6
Dynamic Thermal Estimation of a 3-D Power Electronics System

6.1 System description

In the previous chapter, the dynamic thermal estimation technique was applied on a 2kW, dc-ac, single phase, 7-Level flying capacitor multilevel inverter. The multilevel inverter was open to the environment. Heat was transferred from the components of the inverter to the environment through convective heat transfer. However, this setting does not allow enough heat loss from the inverter to the environment. Hence, the power levels reached in the power electronics system are constrained by thermal limitations of the system.

Increasing the power density of power electronics systems is a desirable objective. One strategy that can help achieve this goal is increasing the heat lost from the power electronics systems to the environment. Enhancing heat transfer from the inverter allows the user to reach higher power levels without reaching crtitical temperatures that can cause the failure of its components.

Convective heat transfer is given by

$$Q_{conv} = hA_s(T_s - T_a), \tag{6.1}$$

where h is the convective heat transfer coefficient, A_s is the surface area from which heat is transferred, T_s is the surface area temperature, and T_a is the ambient temperature. Hence, to increase the convective heat transfer, the user can either increase the surface area from which

heat is transferred or increase the heat transfer coefficient. The latter can be increased by including a fan into the system for example. On the other hand, increasing the surface area from which heat is transferred by convection to the environment can be achieved by attaching to that surface an extended surface made of a highly conductive material. This extended surface is known as a heat sink. Heat sinks usually contain fins.

When the power electronics system is enclosed by a heat sink, there will be no convective heat transfer from its components to the environment. Instead, there will be conductive heat transfer from the components of the system to the extended surface. Convective heat transfer will happen between the heat sink and the environement.

Conductive heat transfer between the components of the power electronics system and the extended surface happens in the z-direction. Furthermore, similar to the 2-dimensional case, there is conductive heat transfer between the components of the power electronics system along the x and y directions. Hence, in the case of enclosed power electronics systems, there is conductive heat transfer along 3 directions. In this case, the dynamic thermal estimation problem should be solved as a 3-dimensional system.

In this chapter, the previous 2 KW multilevel inverter will be enclosed by a heat sink. The proposed dynamic thermal estimation technique will be used to estimate the dynamic thermal behavior of the inverter using a small number of sensors. Figure 6.1 shows the 2 Kw inverter with the extended surface, i.e. the heat sink, attached to it. The heat sink is made of Aluminium which is a highly conductive material (K_{al} 205 W/mK). A 0.02'' fiberglass-reinforced filler and polymer thermal gap pad (Gap Pad 5000S35) is placed on top of the active components of the inverter. The thermal gap pad has a relatively high thermal conductivity. It is useful in filling the air gaps between the active components of the inverter and the base of the Aluminum heat sink. Hence, it enhances the conductive heat transfer in the z direction from the components of the inverter to the heat sink. Consequently, it enhances the overall thermal performance of the enclosed inverter. From an electrical perspective, the thermal gap pad is useful in adding an electrical insulation between the active components of the inverter and the base of the heat sink.

The dynamic thermal behavior of the enclosed inverter will be presented in the next section using a 3-dimensional full order RC thermal model of the system. It will be shown that

including the heat sink increases significantly the complexity of the thermal model, i.e. the number of states of the linear state space thermal model of the system. Hence, it is essential to apply an appropriate model order reduction technique that reduces the complexity of the thermal model while preserving its structure as a RC model.

Figure 6.1 Multilevel dc-ac converter enclosed with a heat sink. The heat sink is made of Aluminum. A thermal gap pad (Gap Pad 5000S35) is placed on top of the active components between the inverter and the base of the heat sink.

6.2 3-D full order RC thermal model

In the enclosed multilevel inverter shown in Figure 6.1, there is conductive heat transfer in 3 directions in the system. In this section, a 3-dimensional RC thermal model that accounts for conductive heat transfer along the x, y, and z directions in the power electronics system will be modeled. Furthermore, the RC thermal model will account for convective heat transfer from the heat sink to the environment.

Similar to the 2-D RC thermal model, the first step in designing a 3-D RC thermal model is to discretize the system into voxels and assign a capacitance value to every voxel. However, in the 2-D RC thermal model, the power electronics system included the inverter only. Hence, the discretization process was applied to the inverter only. In the 3-D RC thermal

model, the power electronics system includes a heat sink in addition to the inverter. Therefore, the discretization process should be applied on the inverter and the heat sink.

The discretization of the inverter for the 3-D full order RC thermal model was made at the level of the functional elements. Each active component in the inverter was assigned a single capacitor. Therefore, the discretization of the inverter in the enclosed system resulted in the same 39 capacitors that were obtained in the 2-D full order RC thermal model of the inverter. It should be noted that the thermal capacitance of the thermal gap pads was neglected. Furthermore, the heat sink was discretized into 39 pixels that have the same geometric properties as the pixels of the inverter. Therefore, the full order RC thermal model of the enclosed inverter has 78 capacitors: 39 capacitors for the inverter and 39 capacitors for the heat sink.

Since the 3-D RC thermal model accounts for conduction in the x and y directions along the plane of the inverter, the 39 capacitors that represent the thermal capacitance of the inverter will be connected through resistances that represent conduction resistances along the x and y directions. Similarly, there is conductive heat transfer in the x and y directions along the base of the heat sink. Therefore, the 39 capacitors that represent the thermal capacitance of the heat sink will be connected through resistances that represent conduction resistances along the x and y directions. The capacitors of the inverter thermal model and the capacitors of the heat sink thermal model will be connected through resistances that represent conduction resistance along the z direction from the inverter to heat sink. These resistances account for the additional conduction resistance in the z direction created by the thermal gap pads. Furthermore, there will convection resistances from every voxel of the heat sink to a voltage source that represents the ambient temperature. The main heat sources in the enclosed inverter are still the 12 GaN transistors. Therefore, the 3-D RC thermal model has 12 current sources connected to the capacitors that represent the thermal capacitances of the GaN transistors. The 3-D graph-based thermal model of the system will be shown in the next subsection.

The thermal capacitances, conduction resistances, and convection resistances are calculated according to the formulas presented in chapter 2. Also, similar to the 2-D RC thermal model, the dynamic thermal behavior of the enclosed inverter can be obtained by modeling a circuit of resistors and capacitors in Simscape in SIMULINK, or by applying the

conservation of energy principle on a 3-D graph-based thermal model of the system that results in a linear state space model. However, since the 3-D RC thermal model has 78 capacitors and accounts for conduction in 3 directions in the system, modeling a RC circuit in SIMULINK is a very complicated task. Hence, the dynamic temperature profile of the enclosed inverter will be obtained through a linear state space model. This strategy will be presented in the next subsection.

6.2.1 3-D full order RC thermal model results

In this section, the dynamic thermal behavior of the enclosed inverter will be obtained by applying the conservation of energy principle on the 3-dimensional graph-based thermal model of the system. The full order graph-based thermal model of the enclosed inverter is composed of 3 layers. The first layer represents the thermal model of the inverter only. Hence, it is composed of 39 vertices connected in the x and y directions through edges that represent the conduction resistances in these directions. The second layer represents the thermal model of the heat sink. Hence, it is also composed of 39 vertices connected in the x and y directions through edges that represent conduction resistances in these directions. The third layer represents the ambient temperature and is composed of a single vertex with an infinite capacitance. The inverter layer and the heat sink layer are connected in the z direction through edges that represents the conduction resistance between the inverter and the heat sink. The heat sink layer and the third layer (the ambient temperature) are connected through edges that represent the convection resistances between the fins and the environment. Figures 6.2 and 6.3 show the first layer and the second layer of the 3-D graph-based thermal model of the enclosed inverter. The edges that represent the resistances in the z direction are not shown in the figures for simplicity. Furthermore, similar to the 2-D RC thermal model, the 12 GaN transistors are the main heat sources in the 3-D RC thermal model. Hence, they will be modeled as current sources connected to the vertices that represent the thermal capacitance of the GaN transistors. The power cycle tested in each current source is shown in Figure 6.4. The linear state space model for this graph-based thermal model is obtained by applying the conservation of energy principle on every vertex of the 78 vertices. Equation (6.2) shows the first order differential equation for state 2.

$$C_2\dot{T}_2 = \frac{T_1 - T_2}{R_{1,2}} - \frac{T_2 - T_3}{R_{2,3}} - \frac{T_2 - T_8}{R_{2,8}} - \frac{T_2 - T_{41}}{R_{2,41}}. \quad (6.2)$$

The last term in the equation represent the conduction resistance in the z direction between vertex 2 of the inverter and vertex 41 of the heat sink. Also, it should be noted that the equation does not include a convective heat transfer term since the inverter is not open to the environment. By applying the conservation of energy principle on the 78 vertices, a system of coupled first order differential equations can be obtained. By rearranging the terms in these equations, a linear state space model of 78 states can be obtained. The 78 states of the full order 3-D RC thermal model are shown in Figure 6.5. The hottest spot in the system experienced an increase of 5^{o}C above the ambient temperature. Furthermore, it can be seen the temperature gradient in the heat sink is negligible.

The dynamic thermal behavior of the enclosed inverter shown in this section is theoretical, i.e. obtained from the full order 3-D RC thermal model. Before proceeding with the next steps of the proposed dynamic thermal estimation technique, the dynamic thermal behavior of the enclosed inverter will be tested experimentally using the same power cycles used in the 3-D RC thermal model. It will be shown that, besides providing an accurate dynamic thermal estimation of power electronics systems, the proposed method can be used for fault detection in power electronics systems. The experimental validation of the enclosed inverter was performed by placing thermocouples at various locations in the system.

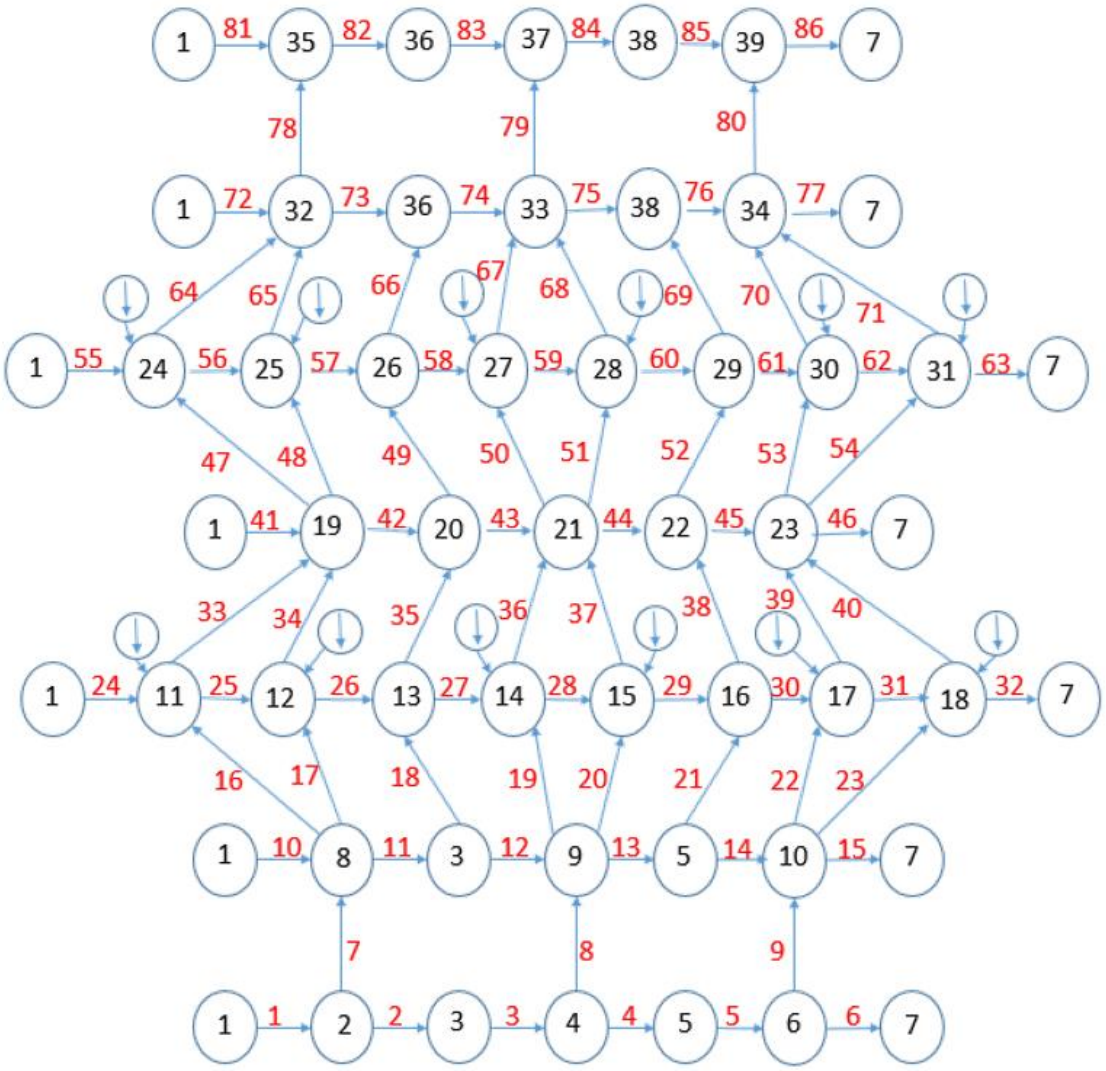

Figure 6.2 First layer of the 3-D graph-based thermal model, i.e. thermal model of the inverter only. The edges that connect the inverter to the heat sink are not shown in the figure for simplicity.

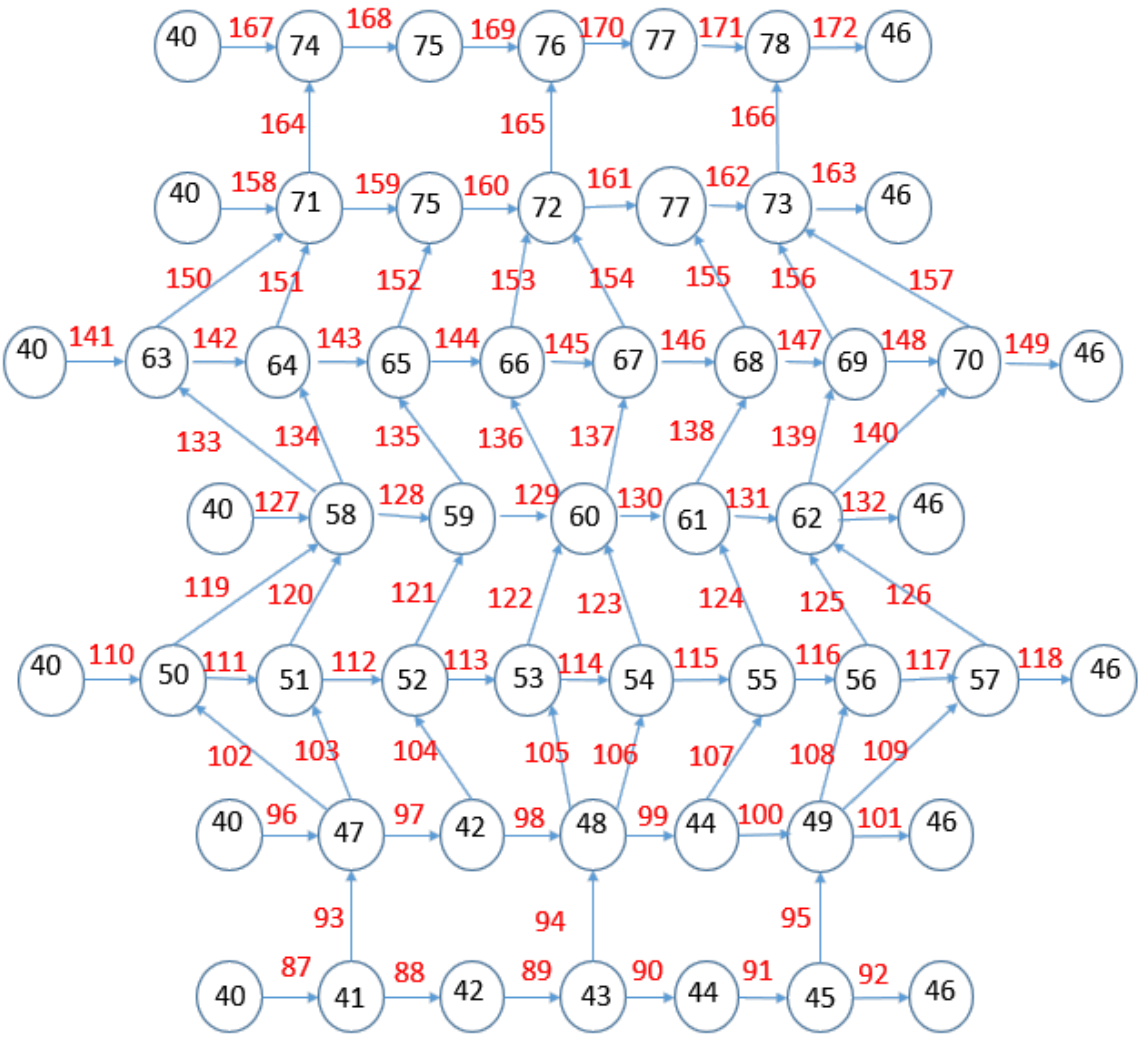

Figure 6.3 Second layer of the 3-dimensional graph-based thermal model of the enclosed inverter, i.e. thermal model of the heat sink. The heat sink was discretized into 39 voxels (with the same geometric properties as the voxels of the inverter) represented by 39 vertices. The edges that connect the inverter to the heat sink are not shown in the figure for simplicity.

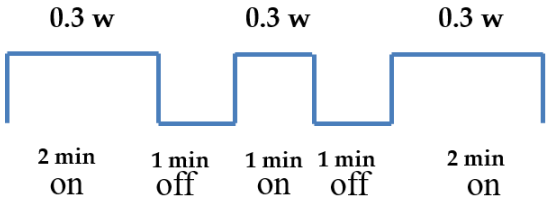

Figure 6.4 Power cycle for each of the 12 current sources of the 3-D RC thermal model.

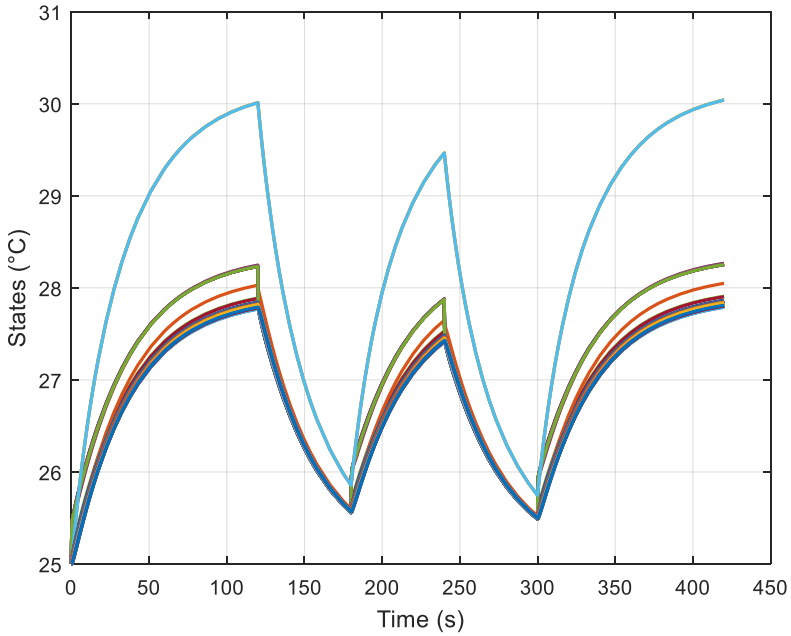

Figure 6.5 The 78 states of the full order 3-D RC thermal model (39 states for the inverter and 39 states for the heat sink).

6.2.2 Experimental validation of the 3-D RC thermal model

Since the inverter is enclosed, IR thermal imaging is not a candidate measuring tool for the dynamic thermal behavior of the system. To measure the dynamic thermal behavior of the 3-D power electronics system, 13 thermocouples were placed at various locations on the inverter. The thermocouples were fixed using Kapton tape. The locations of the 13

thermocouples are shown in Figure 6.6. Thermal gap pads were placed on top of the active components in the system as shown in Figure 6.7. Finally, the heat sink was fixed on top of the thermal gap pads. The enclosed inverter is shown in Figure 6.8.

The readings of the 13 thermocouples are shown in Figure 6.9. The sensor readings implied the existence of an additional heat source other than the anticipated heat sources for the inverter, i.e. the GaN transistors. Furthermore, the drift in the sensor readings shown in Figure 6.9 implies the existence of a faulty component that is heating up continuously throughout the cycle and is causing additional heating to the components in its neighborhood. Using an IR camera on the open inverter, it was found that the component marked with the red circle in Figure 6.6 is the faulty component generating additional heat in the circuit.

In the next subsection, the previous 3-D RC thermal model will be modified in order to include the additional heating from the faulty component. The dynamic thermal behavior of the full order 3-D RC thermal model that includes the heat generated from the faulty component will be compared to the experimental results.

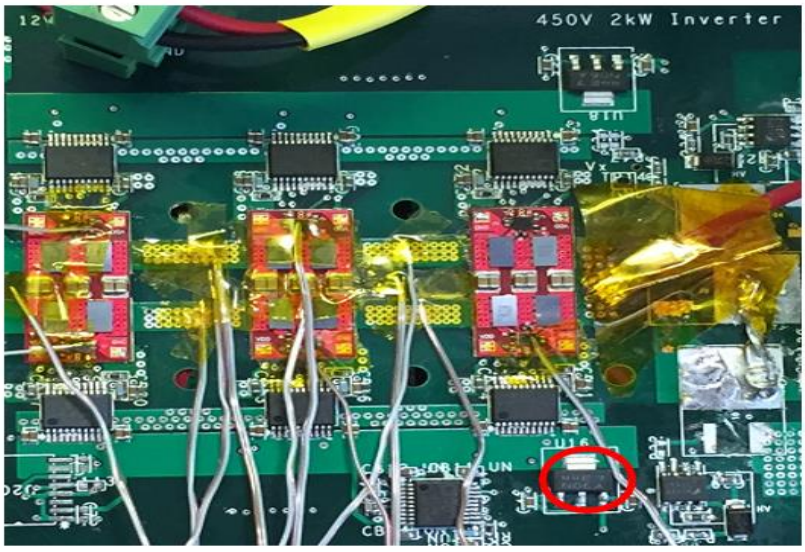

Figure 6.6 The locations of the 13 thermocouples placed on the inverter. The encircled component is the faulty component causing additional heating in the circuit.

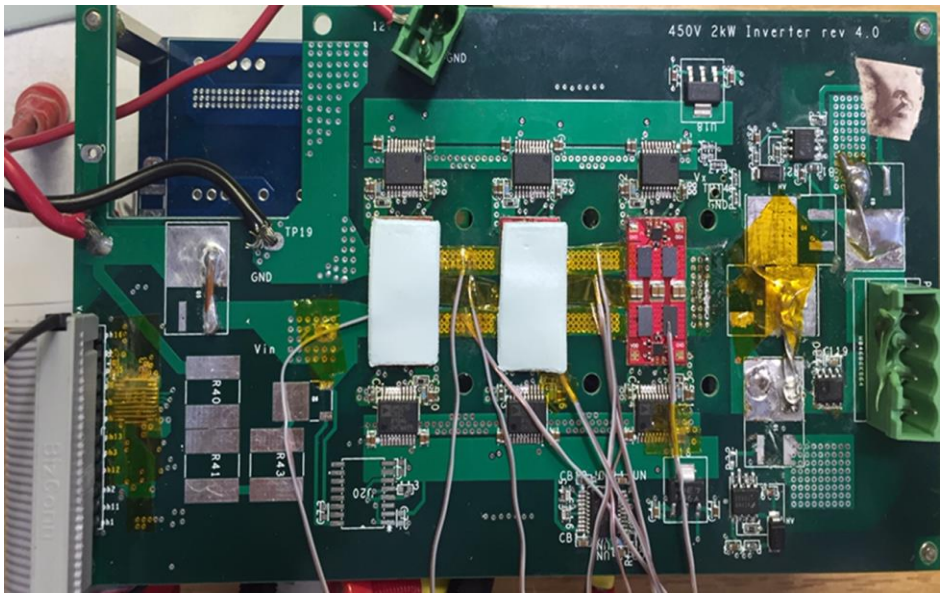

Figure 6.7 Placing thermal gap pads on top of the active components in the circuit.

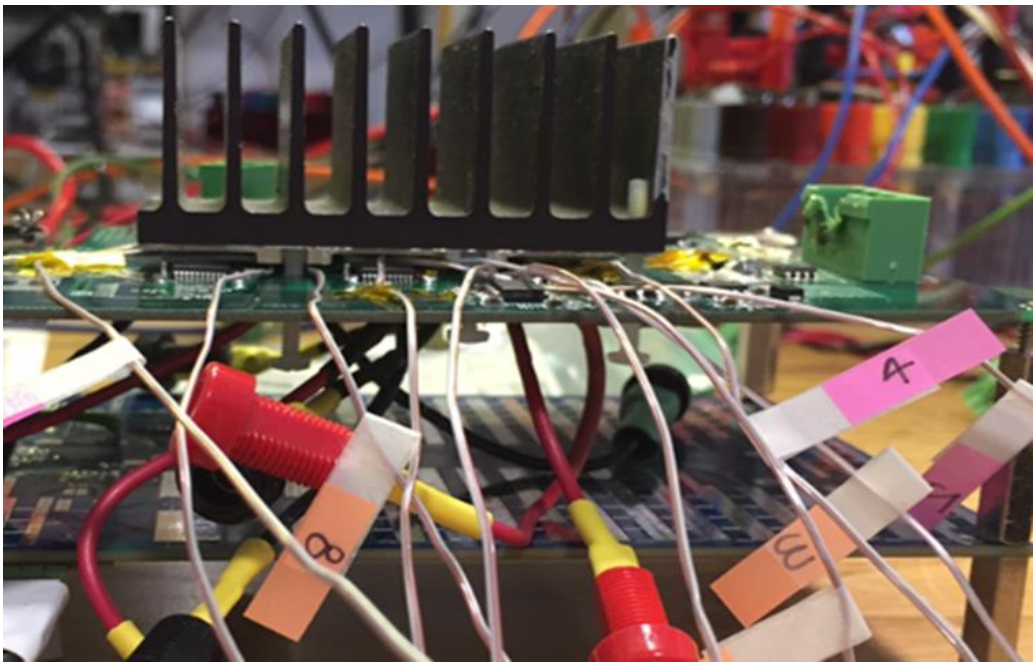

Figure 6.8 Placing the Aluminum heat sink on top of the thermal gap pads.

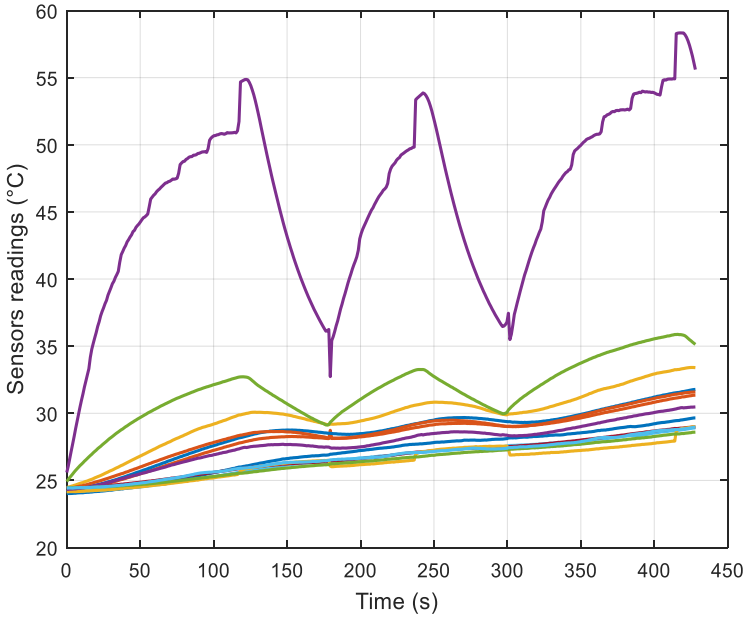

Figure 6.9 The measurements of the 13 sensors.

6.2.3 3-D RC thermal model for the enclosed inverter with faulty component

To account for the additional heat generated in the circuit, an additional current source was added to the full order 3-D RC thermal model of the enclosed inverter. The additional current source is connected to node 6. The input to the current source is a continuously increasing signal.

The 78 states of the full order 3-D RC thermal model that account for the heat generated from the faulty component are shown in Figure 6.10. It can be seen that by adding the additional heat source in the 3-D RC thermal model, the theoretical dynamic thermal behavior of the system matched with the sensor readings shown in Figure 6.9. The circles shown in Figure 6.10 represent the measurement of sensor 5 which is reading state 16 of the 3-D full order RC thermal model. Therefore, by comparing the sensor readings to the expected dynamic thermal behavior of the power electronics system obtained from the RC model of the system, the user can identify the existence of faulty components in the system since such components become additional heat sources.

In the next section, the complexity of the 3-D RC thermal model, i.e. the number of states of the linear state space, will be reduce by applying the aggregation-based model order reduction technique presented in chapter 3.

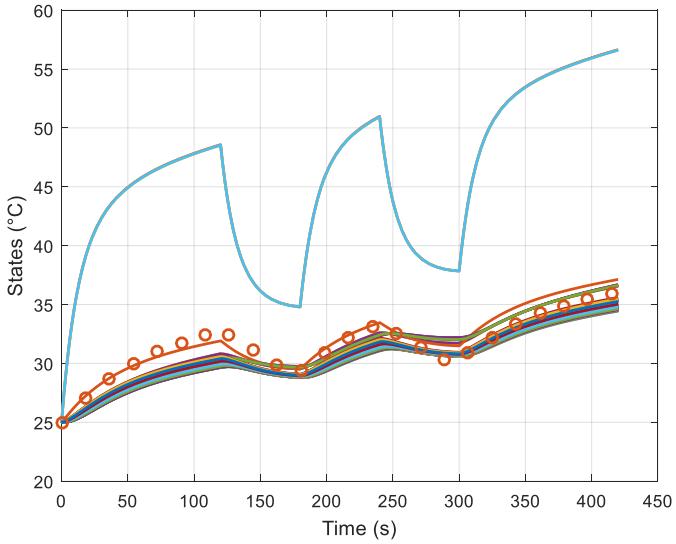

Figure 6.10 The 78 states of the full order 3-D RC thermal model that accounts for the faulty component in the enclosed inverter. The circles represent the measurement of sensor 5 reading state 16.

6.3 3-D reduced order RC thermal model

The full order 3-D RC thermal model of the enclosed inverter is composed of 78 capacitors: 39 capacitors representing the thermal capacitance of the inverter and 39 capacitors representing the thermal capacitance of the heat sink. Therefore, the linear state space thermal model has 78 states which is a large number of states if that system is used for estimation purposes. Therefore, the aggregation-based structure-preserving model order reduction technique will be used to reduce the complexity of the 3-D RC thermal model.

It was mentioned in the previous section that the discretization of the inverter in the 2-D and 3-D RC thermal models is exactly the same. Therefore, the first layer of the 3-D graph-based thermal model of the enclosed inverter is similar to the 2-D graph-based thermal model of the inverter, i.e. the resistance and capacitance values are the same. Hence, applying the model order reduction technique on the first layer of the 3-D graph-based thermal model results

in the same sign structure for the second eigenvector the $\hat{P}$ matrix obtained in the previous chapter. This implies that the inverter in the 3-D system can be aggregated into the same 9 super-nodes that were obtained in the 2-D reduced order RC thermal model. Furthermore, the homogeneity of the material of the heat sink allowed an even distribution of heat along the base of the heat sink. The conduction resistances in the x and y directions in the heat sink layer of the 3-D graph-based thermal model were negligible compared with the z direction. Hence, the 39 nodes of the heat sink can be aggregated into a single super-node.

The overall 3-D reduced order RC thermal model resulted in 10 super-nodes: 9 super-nodes for the inverter and 1 super-node for the heat sink. The 10 super-nodes of the 3-D reduced order RC thermal model are shown in Figure 6.11. It can be seen that the 3-D reduced order RC thermal model can simulate accurately the dynamic thermal behavior of the enclosed inverter using only 10 super-nodes with an error of less than 3^{o}C between the 78 states of the 3-D full order RC thermal model and their corresponding super-nodes in the 3-D reduced order RC thermal model.

The 3-D reduced order RC thermal model will be used in a continuous-discrete Kalman filter to estimate the dynamic thermal behavior of the enclosed inverter using a small number of sensors. Therefore, the next step is to find the optimal number and optimal locations of the temperature sensors that should be used in the system.

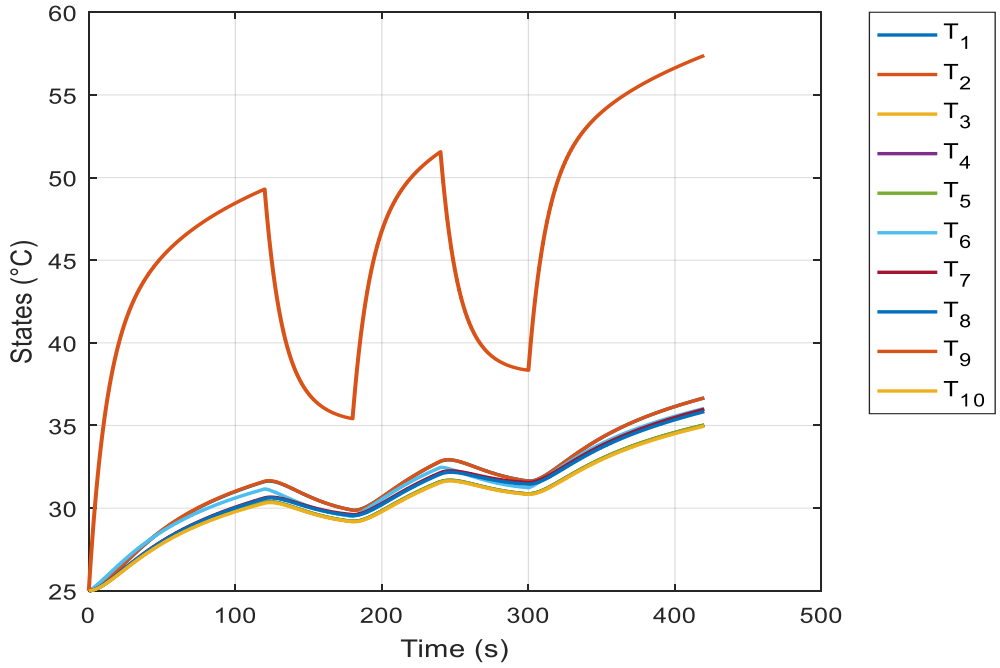

Figure 6.11 The 10 super-nodes of the reduced order 3-D RC thermal model.

6.4 Sensor placement optimization

In the 2-dimensional system, the state estimation errors obtained by placing the temperature sensors according to the condition number of observability Gramian and according to the trace of observability Gramian were compared. It was found that for a specific number of temperature sensors, using the trace of observability Gramian as a performance metric for optimal sensor locations results in smaller state estimation errors compared to when the condition number of observability Gramian is used as a performance metric. Therefore, for the 3-dimensional system, the temperature sensors will be placed by maximizing the trace of observability Gramian.

Table 6.1 shows the optimal sensor locations in the 3-D reduced order RC thermal model. Also, since the super-nodes of the reduced order thermal model represent large areas of the physical system, the optimization of the locations of the temperature sensors was also performed for the 3-D full order RC thermal model. Table 6.2 shows optimal sensor locations in the 3-D full order RC thermal model.

Table 6.1 Optimal sensor locations for the 3-D reduced order RC thermal model using the trace of observability Gramian matrix as trade-off.

Number of sensors	Sensor location (State number)	Trace of Obs. Grammian Matrix
1	2	8.6627
2	1,2	17.3255
3	1,2,6	25.9836
4	1,2,4,6	34.6370
5	1,2,4,6,10	43.2900
6	1,2,4,6,8,10	51.9420
7	1,2,4,5,6,8,10	60.5934
8	1,2,4,5,6,7,8,10	69.2448
9	1,2,4,5,6,7,8,9,10	77.8963
10	1,2,3,45,6,7,8,9,10	86.5477

Table 6.2 Optimal sensor locations for the 3-D full order RC thermal model using the trace of observability Gramian matrix as trade-off.

# sensor	Sensor locations (State number)	Trace of obs. Gramian
1	75	0.6733
2	42,75	1.3466
3	44,75,77	2.0198
4	42,44,75,77	2.6931
5	3,40,42,46,75	3.3469
6	40,42,44,46,75,77	4.0275
7	36,40,42,44,46,75,77	4.6935
8	3,5,36,42, 44,46,75,77	5.3583
9	5,38,40-42, 44,46,75,77	6.0219
10	1,3,36,38,40,42,44,46,75,77	6.6892

Table 6.2 (cont.)

11	1,3,5,36,38,40,42,44,46,75,77	7.3552
12	1,3,5,36,40,41,42,44,46,74,75,77	8.0139
13	1,3,5,7,36,38,40-42,44,46,75,77	8.6813
14	1,3,5,7,36,38,40-42,44,46,74,75,77	9.3437
15	1,3,5,7,36,38-42,44,46,74,75,77	9.9953
16	1,3,5,7,35,36,38-42,44,74,75,77,78	10.6422
17	1-3,5,7,35,36,38,40-42,44-46,74,77,78	11.2985
18	1-3,5,7,35,36,38,40-42,44-46,74,75,77,78	11.9718
19	1-3,5-7,35,36,38,40-42,44-46,74,75,77,78	12.6128
20	2,3,5-7,35,36,38-46,74,75,77,78	13.2456
21	1-3,5-7,35,36,38-46, 74,75,77,78	13.9093
22	1-3,5-7,35,36,38-46, 74-78	14.5434
23	1-7,35,36,38-46, 74-78	15.1671
24	2-7,20,35-46, 74-78	15.6918
25	1-5,7,20, 35-46, 52,74-78	16.2391
26	1-7,20,22, 35-46,74-78	16.9201
27	1-7,20,22, 35-46,71,74-78	17.4693
28	1-7,20,22, 35-46,49,71,74-78	18.0185
29	1-7,20,22, 35-46,49,71,73-78	18.5677
30	1-7,20,22, 35-46,49,52,65,71,73-78	19.1031
31	1-7,20,22, 35-47,49,52,71,73-78	19.6523
32	1-7,20,22, 35-47,49,52,65,71,73-78	20.1876
33	1-7,13,20,35-47,49,52,65,68,71,73-78	20.6895
34	1-7,16,20,22,35-47,49,55,65,68,71,73-78	21.2542
35	1-7,13,20,22,35-47,49,52,55,65,68,71,73-78	21.7895
36	1-7,13,16,20,22,26,35-47,49,52,55,68,71,73-78	22.3167
37	1-7,13,16,22,26,29,35-47,49,52,55,65,68,71,73-78	22.8186
38	1-8.16,20,22,26,29,35-47,49,52,55,65,68,71,73-78	23.3644
39	1-7,13,16,19,20,22,26,29,35-47,49,52,55,63,65,71,73-78	23.9012

Table 6.2 (cont.)

40	1-7,13,16,20,22,26,29,35-47,49,50,55,57,5863,70,71,73-78	24.4135
41	1-7,13,16,19,20,22,23,29,35-47,49,50,52,55,57,68,70,71,73-78	24.9520
42	1-7,13,19,20,22,26,29,35-47,49,50,52,55,57,63,65,68,70,71,73-78	25.4917
43	1-7,13,20,22,23,25,29,35-47,49,52,55,57,58,62,63,65,68,70,71,73-78	26.0049
44	1-7,13,16,19,20,22,26,29,35-47,49,50,52,55,57,59,63,65,68,70,71,73-78	26.5415
45	1-7,13,16,19,20,22,23,26,29,35-47,49,50,52,55,57,62,63,65,68,70,71,73-78	27.0684
46	1-7,13,16,19,20,22,23,26,29,35-47,49,50,52,55,57,58,62,63,65,68,70,71,73-78	27.5894
47	1-7,13,16,19,20,22-24,26,29,35-47,49,50,52,55,57,58,62,63,65,68,70,71,73-78	28.1018
48	1-7,13,18-20,22,23,26,29,35-47,49-52,55,57,58,1-,63,65,68,70,71,73-78	28.6129
49	1-78, except 9-12,14,15,17,18,21,24,25,27,28,30-33,48,51,53,54,56,60,64,66,67,69,72	29.1313
50	1-78, except 9-12,14,15,17,18,21,24,25,27,28,30-34,48,53,54,60,64,66,67,69,72	29.6515
51	1-78, except 8,9,12,14,15,17,18,21,24,25,27,28,30,31,33,34,48,53,54,60-62,66,67,69,72	30.1660
52	1-78, except 8,9,12,14,15,17,18,21,24,25,27,28,30,31,33,34,48,53,54,60-62,66,67,69,72	30.6647
53	1-78, except 9,11,12,14,15,17,18,21,24,25,27,28,30,31,33,34,48,53,54,56,60,66,67,69,72	31.1909
54	1-78, except 8-11,14,15,17,18,21,24,25,27,28,30,31,33,34,48,53,54,60,66,67,69	31.6724
55	1-78, except 8,9,11,14,15,17,18,21,24,25,27,28,30-33,48,53,54,60,66,67,72	32.2176
56	1-78, except 9,11,14,15,17,18,21,24,27,28,30,31,33,34,48,51,53,54,60,66,67,72	32.7289
57	1-78, except 9,11,14,15,17,21,24,25,27,28,30,31,33,34,48,53,54,60,66,67,72	33.2425
58	1-78, except 9,12,14,15,17,18,21,25,27,28,30,31,33,48,53,54,60,66,67,72	33.7549
59	1-78, except 9,12,14,15,17,21,25,27,28,30,31,33,48,53,54,60,66,67,72	34.2675
60	1-78, except 9,12,14,15,17,21,25,27,28,31,33,48,53,54,60,66,67,72	34.7797
61	1-78, except 9,12,14,15,21,25,27,28,30,33,48,53,54,60,66,67,72	35.2921

Table 6.2 (cont.)

62	1-78, except 9,14,15,17,21,27,28,30,33,48,53,54,60,66,67,72	35.8044
63	1-78, except 9,14,15,21,27,28,30,33,48,53,54,60,66,67,72	36.3166
64	1-78, except 14,15,21,25,27,28,33,48,53,54,60,66,67,72	36.7524
65	1-78, except 9,14,15,21,27,28,33,53,54,60,66,67,72	37.3096
66	1-78, except 9,15,21,27,28,33,53,54,60,66,67,72	37.7452
67	1-78, except 9,14,15,21,27,28,33,53,54,60,67	38.2310
68	1-78, except 9,14,15,21,27,28,33,60,66,67	38.6717
69	1-78, except 9,14,15,21,27,28,33,60,67	39.1125
70	1-78, except 9,14,15,21,27,33,60,67	39.5841
71	1-78, except 9,14,15,27,28,33,60	39.9924
72	1-78, except 9,15,27,28,33,60	40.4280
73	1-78, except 9,15,27,28,33	40.8642
74	1-78, except 14,15,27,28	41.3001
75	1-78, except 14,15,28	41.7357
76	1-78, except 14,15	42.1713
77	1-78, except 15	42.6069
78	1-78	43.0425

As it can be seen in Tables 6.1 and 6.2, maximizing the trace of observability Gramian results in optimal sensor placement for a specific number of sensors. In the next section, the optimal number of temperature sensors will be found based on the state estimation error obtained from the continuous-discrete Kalman filter. Also, the estimated dynamic thermal behavior of the 3-D RC thermal model will be presented.

6.5 Continuous-discrete Kalman filter

It was shown that applying the conservation of energy principle on the 3-D graph-based thermal model results in a linear state space model. Hence, the optimal filter for this system, assuming the system has Gaussian noise, is the Kalman filter. In this section, a continuous-

discrete Kalman filter will be used, along with an optimal number and optimal placement of temperature sensors, to reconstruct the dynamic thermal behavior of the enclosed inverter.

First, the continuous-discrete Kalman filter was used to find the optimal number of temperature sensors that should be placed at optimal locations in the enclosed inverter. Figure 6.12 shows the sum of the absolute value of the state estimation error of the reduced order thermal model vs the number of temperature sensors used. It can be seen that adding more than 6 temperature sensors in the system does not reduce the state estimation error significantly and only increases the cost and complexity of the system. Hence, according to Figure 6.12 it can be deduced that 6 is the optimal number of temperature sensors for this system. Based on Table 6.1, the 6 sensors should be placed on super-nodes 1, 2, 4, 6, 8, and 10.

Figures 6.13-6.17 show the theoretical (obtained from RC model) versus the estimated (obtained from Kalman filter) values of the 10 super-nodes of the reduced order thermal model. It can be seen that the dynamic thermal behavior of the 3-D reduced order thermal model was accurately estimated using only 6 sensors in the enclosed inverter. However, similar to the 2-D dynamic thermal estimation problem, the ultimate goal for the 3-D dynamic thermal estimation problem is to estimate the thermal behavior of the full order RC thermal model using a small number of temperature sensors. Therefore, the 3-D full order RC thermal model was used in a reduced order continuous-discrete Kalman filter. This will allow the user to recreate the dynamic thermal behavior of the full order thermal model using the reduced order RC thermal model. Figures 6.18-6.22 show the estimated states of the reduced order model obtained from the Kalman filter versus their corresponding theoretical equivalent states in the full order model obtained from the full order RC thermal model. It should be noted that, in Figure 6.22 the tenth estimated state of the reduced order model is compared to states 40-78 that represent the heat sink in the full order RC thermal model.

Therefore, it was shown that the proposed dynamic thermal estimation technique can accurately reconstruct the 3-D dynamic thermal behavior of power electronics systems using a small number of temperature sensors placed at optimal locations in the system.

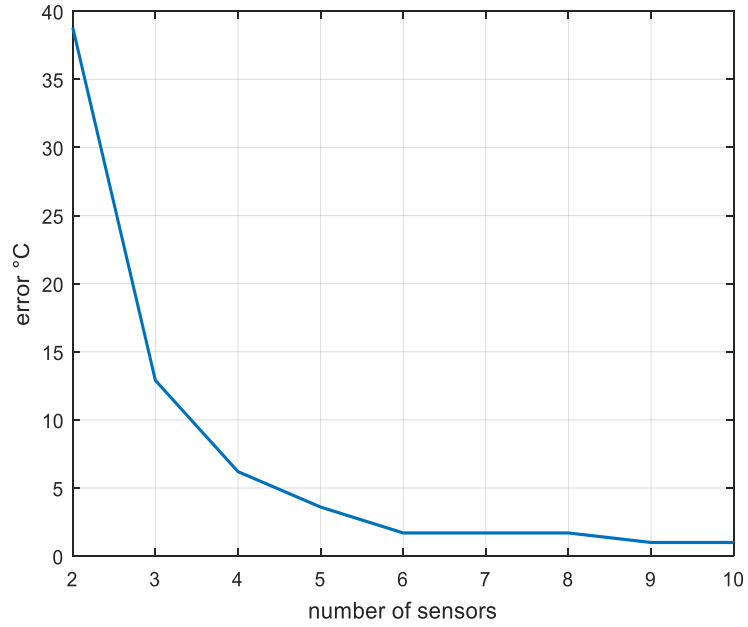

Figure 6.12 Sum of the absolute value of the state estimation error of the reduced order thermal model vs the number of temperature sensors used.

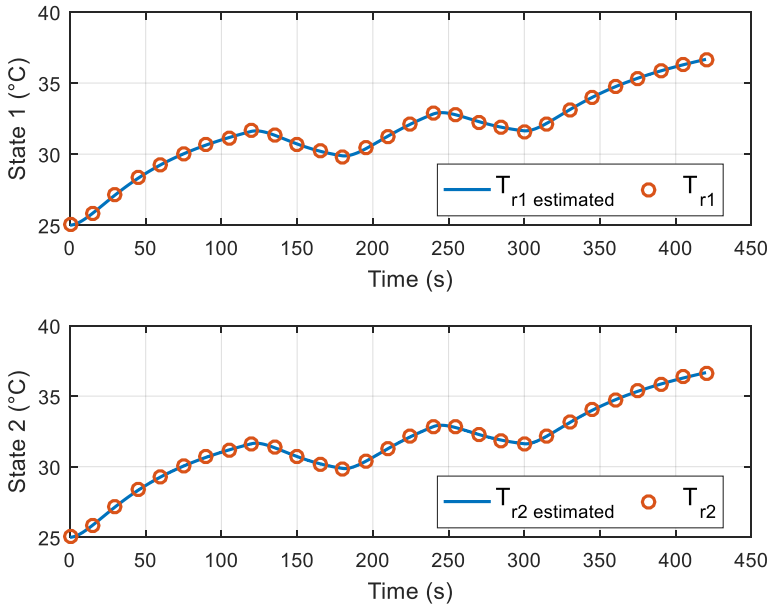

Figure 6.13 Theoretical (RC model) vs estimated (Kalman filter) values of the first and second states of the 3-D reduced order thermal model.

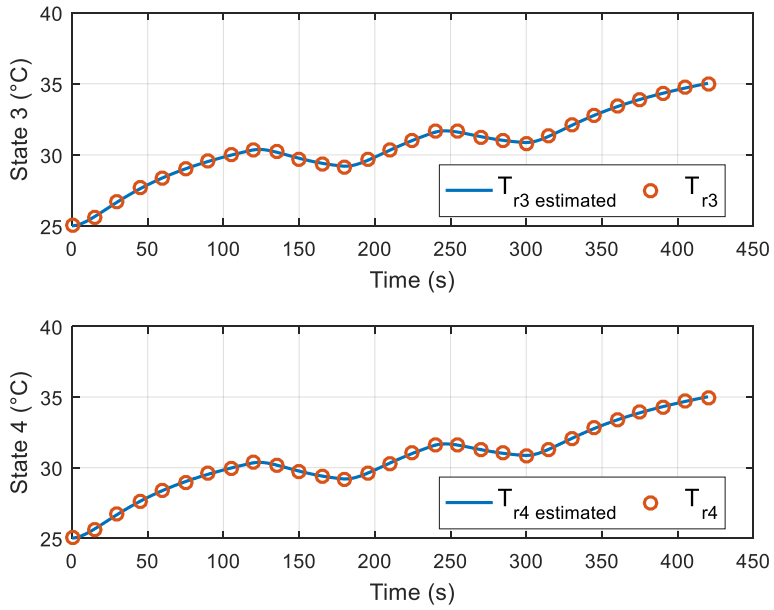

Figure 6.14 Theoretical (RC model) vs estimated (Kalman filter) values of the third and fourth states of the 3-D reduced order thermal model.

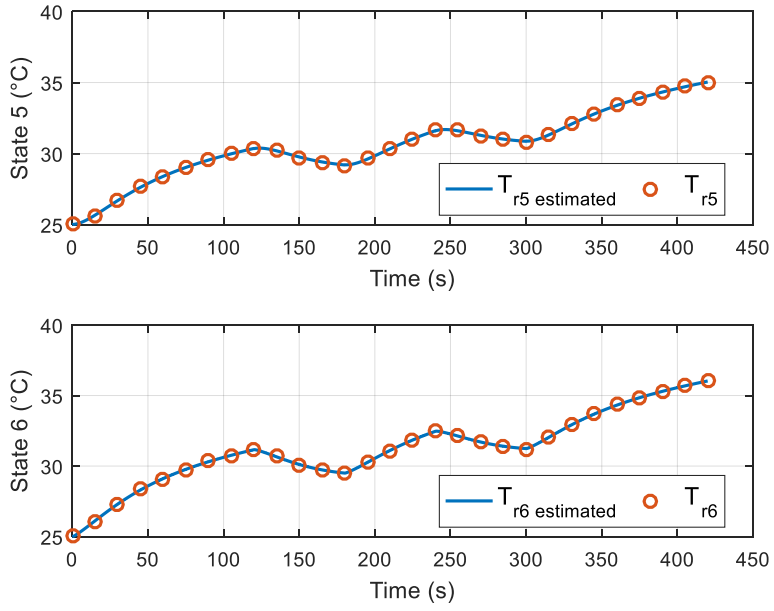

Figure 6.15 Theoretical (RC model) vs estimated (Kalman filter) values of the fifth and sixth states of the 3-D reduced order thermal model.

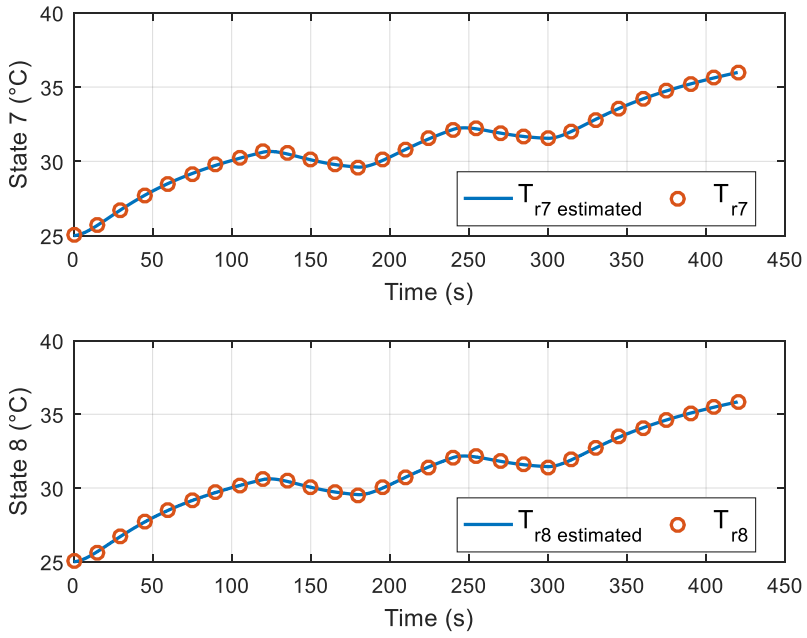

Figure 6.16 Theoretical (RC model) vs estimated (Kalman filter) values of the seventh and eighth states of the 3-D reduced order thermal model.

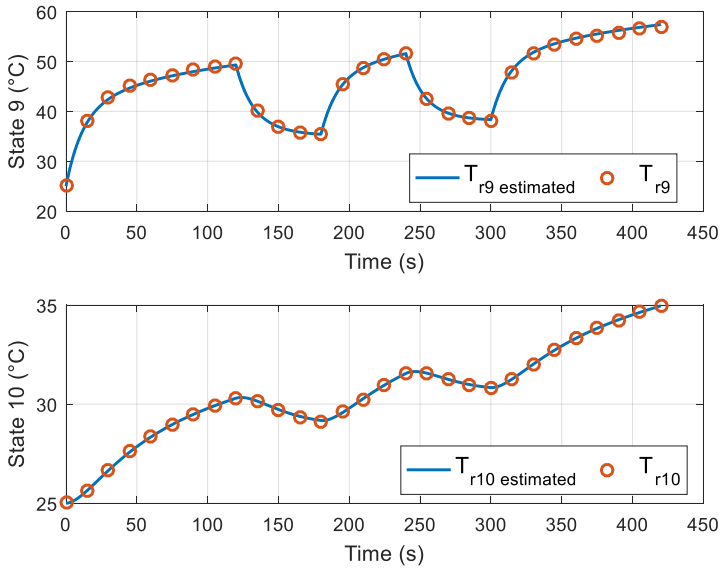

Figure 6.17 Theoretical (RC model) vs estimated (Kalman filter) values of the ninth and tenth states of the 3-D reduced order thermal model.

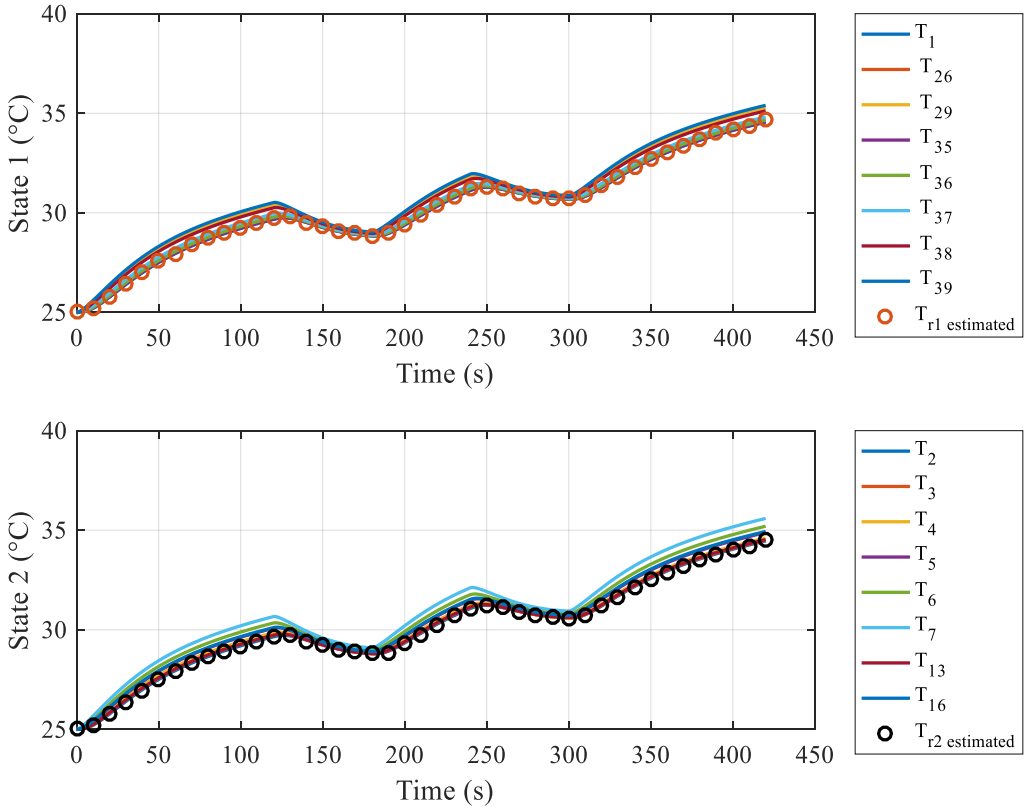

Figure 6.18 Estimated first and second states of the reduced order model (Kalman filter) vs their corresponding theoretical equivalent states in the full order model (RC model).

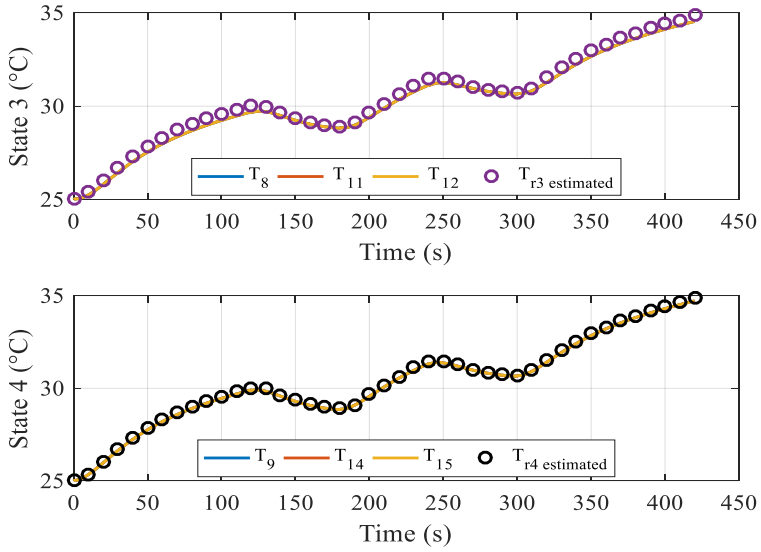

Figure 6.19 Estimated third and fourth states of the reduced order model (Kalman filter) vs their corresponding theoretical equivalent states in the full order model (RC model).

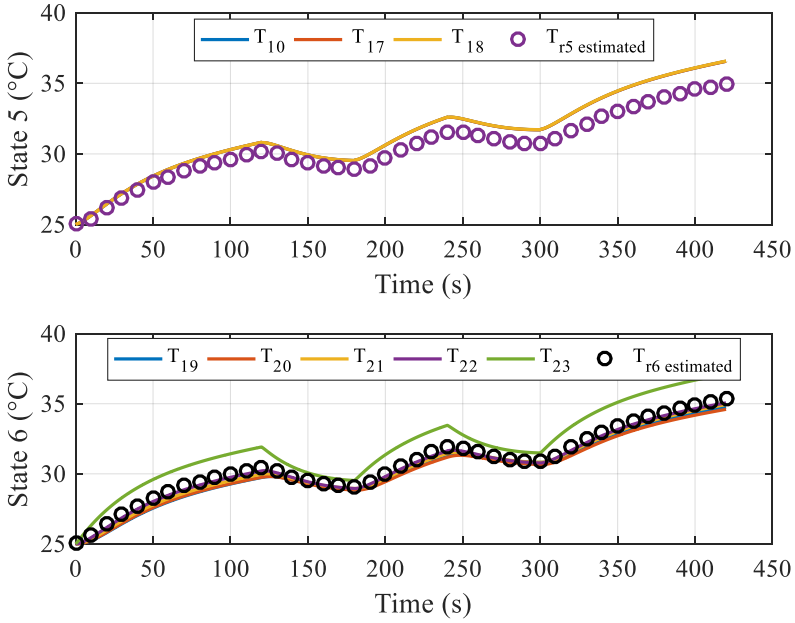

Figure 6.20 Estimated fifth and sixth states of the reduced order model (Kalman filter) vs their corresponding theoretical equivalent states in the full order model (RC model).

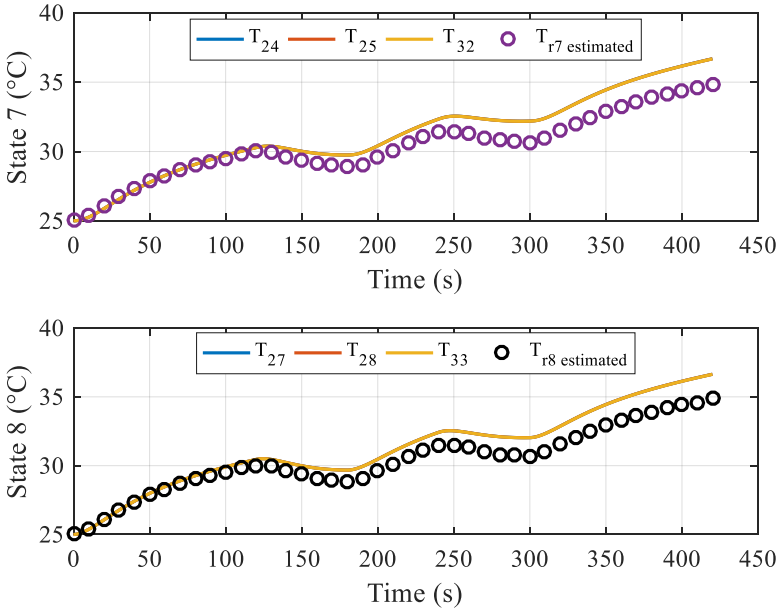

Figure 6.21 Estimated seventh and eighth states of the reduced order model (Kalman filter) vs their corresponding theoretical equivalent states in the full order model (RC model).

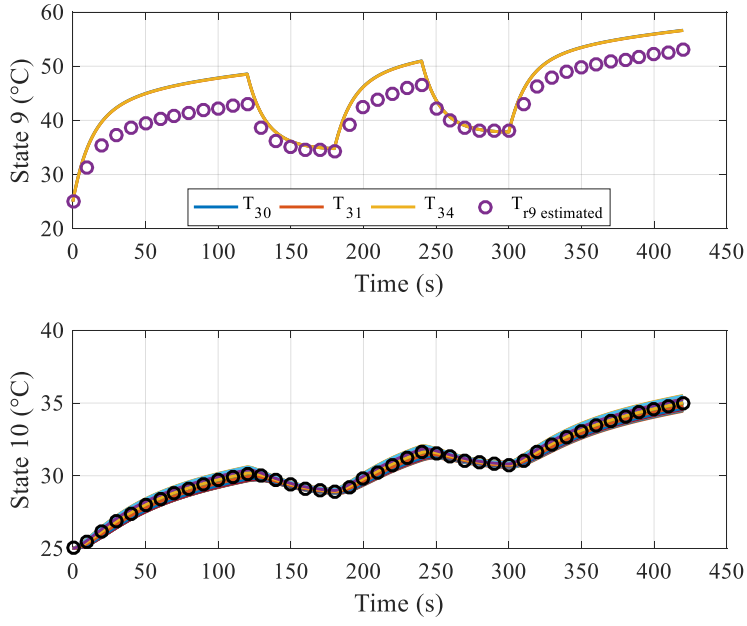

Figure 6.22 Estimated ninth and tenth states of the reduced order model (Kalman filter) vs their corresponding theoretical equivalent states in the full order model (RC model).

Chapter 7
Conclusion

7.1 Summary of research contributions

This thesis proposes a method for accurate dynamic thermal estimation of power electronics systems. Accurate state estimates are essential for dynamic thermal management techniques and high-power density systems. The availability of accurate dynamic temperature estimates play a key role in increasing the power density of power electronics systems by allowing the components of the system to be pushed closer to their failure. When there is confidence in the estimates, the safety factor can be decreased.

A set of tools that can be used for temperature estimation and fault detection in highly complex and interconnected thermal systems was provided. The proposed dynamic thermal estimation scheme is composed of dynamic thermal modeling, model order reduction, optimization of the number and locations of the temperature sensors, and filtering.

The dynamic thermal modeling technique used is based on the analogy between electrical systems and thermal systems. A RC thermal model was used to simulate the spatially and temporally dependent temperature profile of the power electronics systems. It was shown that this technique can simulate the dynamic thermal behavior of power electronics with good accuracy and reasonable complexity which is desired if the thermal model is used for control or estimation purposes.

A structure-preserving aggregation-based model order reduction technique based on Markov chain aggregation was used to further reduce the complexity of the RC thermal models while preserving their accuracy. The reduced order models obtained were RC models also but

with a fewer number of capacitors. Therefore, there was a physical correspondence between the reduced order model and the physical system. Preserving the physical meaning of the states of the reduced order model is important for sensor placement.

Sensors were placed based on state observability. Optimal sensor placement was obtained by using the trace of observability Gramian as an information-based performance metric. Maximizing the trace of observability Gramian leads to improved observability. However, this optimization problem does not provide information about the optimal number of temperature sensors that should be used. The optimal number of temperature sensors was found based on the state estimation error obtained from the Kalman filter. It was found that after using a certain number of sensors in the system, adding additional sensors does not significantly improve the accuracy of the estimates. It only adds cost and complexity in the system.

It was shown that by applying the conservation of energy principle on the thermal model of the system, a linear state space model can be derived. Assuming Gaussian noise, it is well-known that the Kalman filter is an optimal estimator in this case. Using an optimal number and optimal placement of temperature sensors, it was shown that the dynamic thermal profile of the power electronics system can be accurately reconstructed using a continuously-discrete Kalman filter.

The proposed method was applied on a 2-D system in which an inverter was open to the ambient atmosphere. The full order thermal model was reduced from 39 states to 9 states using the structure preserving model order reduction technique. Also, it was shown that the dynamic thermal behavior of the inverter can be accurately estimated using only 5 sensors placed at specific locations in the system. An IR thermal camera was used to experimentally validate theoretical results.

Furthermore, the proposed method was applied on a 3-D system in which the inverter was enclosed with a heat sink in order to increase the heat transfer from the system to the ambient atmosphere. The dynamic thermal model of the system was reduced from 78 states in the full order model to 10 states in the reduced order model. Also, it was shown that the dynamic thermal behavior of the enclosed inverter can be accurately reconstructed using only 6 sensors placed at specific locations in the system. Theoretical results were validated

experimentally by placing 13 thermocouples in the system since thermal imaging is not a valid measuring technique in the case of enclosed inverters.

7.2 Future work

The method proposed in this thesis is related to thermal modeling and estimation of power electronics. The amount of electric power loss or the amount of heat dissipation in the power electronics system was obtained from an independent electric model of the system. Therefore, the power loss calculation did not include the thermal effect on the electric behavior of the system.

Future work will be based on the electro-thermal modeling and control of power electronics. The electric and thermal models of power electronics systems will be coupled and controlled to manage electric and thermal objectives.

Coupling between the thermal model and the electric model will be achieved through electro-thermal models of the semiconductor devices and parasitics modeling of the power electronics systems. Using this approach, the interdependency between the thermal behavior and the electric behavior of the power electronics systems will be modeled. The parameters of the electric model will be temperature dependent. Hence, the temperature which is an output of the dynamic thermal model will be an input to the temperature dependent electric model. Currents and voltages values in the electric model will be based on the temperature calculated in the thermal model. On the other hand, the temperature obtained in the thermal model will be based on the electric behavior or the amount of power dissipated in the form of heat in the electric model.

Controllers will be used to maintain the temperature of the system below a certain critical temperature and to regulate the electric behavior of the system, i.e. specific output voltage, by controlling the switching frequency or the voltage input to the system. This investigation provides a foundation and framework for dynamic fault detection and diagnosis.

References

[1] R. W. Erickson, *Fundamentals of Power Electronics Fundamentals of Power Electronics*. 2002.

[2] M. Pedram and S. Nazarian, "Thermal Modeling, Analysis, and Management in VLSI Circuits: Principles and Methods," *Proc. IEEE*, vol. 94, no. 8, pp. 1487–1501, 2006.

[3] W. Huang, S. Ghosh, S. Velusamy, K. Sankaranarayanan, K. Skadron, and M. R. Stan, "HotSpot: A compact thermal modeling methodology for early-stage VLSI design," *IEEE Trans. Very Large Scale Integr. Syst.*, vol. 14, no. 5, pp. 501–513, 2006.

[4] A. K. Coskun, T. S. Rosing, and K. Whisnant, "Temperature aware task scheduling in MPSoCs," *Proc. -Design, Autom. Test Eur. DATE*, pp. 1659–1664, 2007.

[5] F. Zanini, D. Atienza, C. N. Jones, and G. De Micheli, "Temperature sensor placement in thermal management systems for MPSoCs," *Circuits Syst. (ISCAS), Proc. 2010 IEEE Int. Symp.*, pp. 1065–1068, 2010.

[6] C. H. Lim, W. R. Daasch, and G. Cai, "A thermal-aware superscalar microprocessor," *Proc. - Int. Symp. Qual. Electron. Des. ISQED*, vol. 2002–Janua, pp. 517–522, 2002.

[7] M. Iachello, G. S. Member, V. De Luca, G. Petrone, N. Testa, L. Fortuna, G. Cammarata, and S. Graziani, "Lumped Parameter Modeling for Thermal Characterization of High-Power Modules," vol. 4, no. 10, pp. 1613–1623, 2014.

[8] S. Sharifi and T. S. Rosing, "Accurate Direct and Indirect On-Chip Temperature Sensing for Efficient Dynamic Thermal Management," *IEEE Trans. Comput. Des. Integr. Circuits Syst.*, vol. 29, no. 10, pp. 1586–1599, 2010.

[9] Y. Zhang, A. Srivastava, and M. Zahran, "Chip level thermal profile estimation using On-chip temperature sensors," *26th IEEE Int. Conf. Comput. Des. 2008, ICCD*, no. 1, pp. 432–437, 2008.

[10] Y. Zhang and A. Srivastava, “Adaptive and autonomous thermal tracking for high performance computing systems,” *Proc. 47th Des. Autom. Conf. - DAC ’10*, p. 68, 2010.

[11] Derek P.Atherton, *Nonlinear Control Engineering*. Van Nostrand Reinhold, 1982.

[12] S. Sharifi, C. C. Liu, and T. S. Rosing, “Accurate temperature estimation for efficient thermal management,” *Proc. 9th Int. Symp. Qual. Electron. Des. ISQED 2008*, pp. 137–142, 2008.

[13] G. Swift, T. S. Molinski, and W. Lehn, “A fundamental approach to transformer thermal modeling - Part I: Theory and equivalent circuit,” *IEEE Trans. Power Deliv.*, vol. 16, no. 2, pp. 171–175, 2001.

[14] K. Skadron, T. Abdelzaher, and M. R. Stan, “Control-theoretic techniques and thermal-RC modeling for accurate and localized dynamic thermal management,” *Proc. Eighth Int. Symp. High Perform. Comput. Archit.*, 2002.

[15] C. Jena, N. Sarbhai, R. Mulaveesala, and S. Tuli, “Pulsed Thermography Simulation : 1D , 2D and 3D Electro-Thermal Model Based Evaluation,” *Simulation*, no. 1, 2006.

[16] A. S. L. Frank P. Incropera, David P. DeWitt, Theodore L. Bergman, *Fundamentals of Heat and Mass Transfer*, 6th ed. .

[17] E. Rodriguez, “powerelectronics.com,” *Proper Cooling Of LED Arrays and Power Converters Improves Performance, Reliability*, 2014. .

[18] H. Behjati, A. Davoudi, and F. Lewis, “Modular DC #x2013;DC Converters on Graphs: Cooperative Control,” *IEEE Trans. Power Electron.*, vol. 29, no. 12, pp. 6725–6741, 2014.

[19] V. Chandan, “Decentralized thermal control of building systems,” 2013.

[20] K. L. Moore, T. L. Vincent, F. Lashhab, and C. Liu, *Dynamic Consensus Networks with Application to the Analysis of Building Thermal Processes**, vol. 44, no. 1. IFAC, 2011.

[21] S. Mukherjee, S. Mishra, and J. T. Wen, “Building temperature control: A passivity-based approach,” *Proc. IEEE Conf. Decis. Control*, pp. 6902–6907, 2012.

[22] J. Koeln, “Hierarchical power management in vehicle systems,” University of Illinois at Urbana-Champaign, 2016.

[23] A. Messac, *Optimization in Practice with MATLAB*. 2015.

[24] R. R. Schaller, "Moore's law: past, present and future," *Spectrum, IEEE*, vol. 34, no. 6, pp. 52–59, 1997.

[25] "barett-group.mcgill.ca," *Nanotechnology: A Brief Overview*. .

[26] A. C. Antoulas, "A survey of model reduction methods for large-scale systems," *Am. Math. Soc.*, vol. 280, pp. 1–28, 2006.

[27] W. Schilders, "Introduction to Model Order Reduction," *Model order Reduct. theory, reasearch Asp. Appl.*, 2008.

[28] K. Glover, "All optimal Hankel-norm approximations of linear multivariable systems and their L, ∞ -error bounds," *Int. J. Control*, vol. 39, no. 6, pp. 1115–1193, 1984.

[29] I. W. Paper, "A Tutorial on Hankel-Norm Approximations," no. October, 1989.

[30] S. Gugercin and A. C. Antoulas, "A Survey of Model Reduction by Balanced Truncation and Some New Results," *Int. J. Control*, vol. 77, no. 8, pp. 748–766, 2004.

[31] B. Moore, "Principal component analysis in linear systems: Controllability, observability, and model reduction," *IEEE Trans. Automat. Contr.*, vol. 26, no. 1, pp. 17–32, 1981.

[32] Y. Liu and B. D. O. Anderson, "Singular perturbation approximation of balanced systems," *Int. J. Control*, vol. 50, no. 4, pp. 1379–1405, 1989.

[33] R. W. Freund, "Model reduction methods based on Krylov subspaces," *Acta Numer.*, vol. 12, no. July 2003, pp. 267–319, 2003.

[34] P. Feldmann and R. W. Freund, "Efficient Linear Circuit Analysis by Pad?? Approximation via the Lanczos Process," *IEEE Trans. Comput. Des. Integr. Circuits Syst.*, vol. 14, no. 5, pp. 639–649, 1995.

[35] D. Bonvin and D. A. Mellichamp, "Unified Derivation and Critical Review of Modal Approaches to Model Reduction," *Int. J. Control*, vol. 35, no. 5, pp. 829–848, 1982.

[36] U. Baur, P. Benner, and L. Feng, "Model order reduction for linear and nonlinear systems : a system-theoretic perspective," *Max Planck Inst. Magdebg. Prepr.*, vol. 21, no. 4, pp. 331–358, 2014.

[37] A. Chatterjee, "An introduction to the proper orthogonal decomposition," *Curr. Sci.*, vol. 78, no. 7, pp. 808–817, 2000.

[38] M. Rewienski and J. White, “A trajectory piecewise-linear approach to model order reduction and fast simulation of nonlinear circuits and micromachined devices,” *IEEE Trans. Comput. Des. Integr. Circuits Syst.*, vol. 22, no. 2, pp. 155–170, 2003.

[39] B. Besselink, N. Van De Wouw, J. M. A. Scherpen, and H. Nijmeijer, “Generalized incremental balanced truncation for nonlinear systems,” pp. 5552–5557, 2013.

[40] K. Fujimoto and J. M. A. Scherpen, *Nonlinear input-normal realizations based on the differential eigenstructure of Hankel operators*. 2003.

[41] K. Fujimoto and J. M. A. Scherpen, “BALANCED REALIZATION AND MODEL ORDER REDUCTION FOR NONLINEAR SYSTEMS BASED ON SINGULAR VALUE Copyright © by SIAM . Unauthorized reproduction of this article is prohibited . Copyright © by SIAM . Unauthorized reproduction of this article is prohibited .,” vol. 48, no. 7, pp. 4591–4623, 2010.

[42] “Balancing for nonlinear systems,” vol. 21, pp. 143–153, 1993.

[43] B. N. Sheehan, “ENOR : Model Order Reduction of RLC Circuits Using Nodal Equations for Efficient Factorization,” no. c, 1999.

[44] L. M. Silveira, M. Kamon, I. Elfadel, and J. White, “A coordinate-transformed Arnoldi algorithm for generating guaranteed stable reduced-order models of RLC circuits,” vol. 7825, no. 98, 1999.

[45] A. Odabasioglu, M. Celik, and L. T. Pileggi, “PRIMA : Passive Reduced-order Interconnect Macromodeling Algorithm *,” pp. 58–65, 1997.

[46] Y. Liu, L. T. Pileggi, and A. J. Strojwas, “Model Order-Reduction of RC (L) Interconnect including Variational Analysis †,” no. L, 1999.

[47] R. W. Freund, “Recent Advances in Structure-Preserving Model Order Reduction,” pp. 1–29.

[48] K. Deng, P. Barooah, P. G. Mehta, and S. P. Meyn, “Building Thermal Model Reduction via Aggregation of States,” *Am. Control Conf.*, pp. 5118–5123, 2010.

[49] K. Deng, Y. Sun, P. G. Mehta, and S. P. Meyn, “An Information-Theoretic Framework to Aggregate a Markov Chain,” pp. 731–736, 2009.

[50] K. Deng, S. Goyal, P. Barooah, and P. G. Mehta, “Structure-preserving model reduction of nonlinear building thermal models,” *Automatica*, vol. 50, no. 4, pp. 1188–

1195, 2014.

[51] J. Mohd, N. H. Hoang, M. A. Hussain, and D. Dochain, “Review and classification of recent observers applied in chemical process systems,” *Comput. Chem. Eng.*, vol. 76, pp. 27–41, 2015.

[52] D. G. Luenberger, “An Introduction to Observers,” 1971.

[53] D. G. Luenberger and S. Member, “Observing the State of Linear System,” pp. 74–80.

[54] A. Radke and Z. Gao, “A Survey of State and Disturbance Observers for Practitioners,” no. 3.

[55] A. E.-N. Gene F. Franklin, J. David Powell, *Feedback Control of Dynamic Systems*, Fourth edi. .

[56] F. Bakhshande and D. S, “ScienceDirect Proportional-Integral-Observer : A brief actual methods using ACC Benchmark methods methods using ACC Benchmark,” *IFAC-PapersOnLine*, vol. 48, no. 1, pp. 532–537, 2015.

[57] G. Ciccarella, M. D. Mora, and A. Germani, “A Luenberger-like observer for nonlinear systems,” vol. 7179, no. June, 2017.

[58] P. D. B. Kovacevic and P. D. Z. Durovic, *Fundamentals of Stochastic Signals, Systems and Estimation Theory with Worked Examples*, Second. 2008.

[59] H. ed. Sorenson, *Kalman Filtering: Theory and Application.* 1985.

[60] E. A. Wan, R. Van Der Merwe, and N. W. W. Rd, “The Unscented Kalman Filter for Nonlinear Estimation.”

[61] S. Gillijns, O. B. Mendoza, J. Chandrasekar, B. L. R. De Moor, D. S. Bernstein, and A. Ridley, “What Is the Ensemble Kalman Filter and How Well Does it Work ?,” pp. 4448–4453, 2006.

[62] G. Evensen, “The Ensemble Kalman Filter : theoretical formulation and practical implementation,” pp. 343–367, 2003.

[63] A. K. Singh and J. Hahn, “Determining Optimal Sensor Locations for State and Parameter Estimation for Stable Nonlinear Systems,” *Ind. Eng. Chem. Res.*, vol. 44, no. 15, pp. 5645–5659, 2005.

[64] S. R. T. Peddada, P. J. Tannous, A. G. Alleyne, and J. T. Allison, “DETC2017-68253 Optimal Sensor Placement Methods For Active Power Electronic Systems,” in

Proceedings of the ASME 2017 International Design Engineering Technical Conferences & Computers and Information in Engineering Conference, 2017.

[65] A. K. Singh and J. Hahn, "On the use of empirical gramians for controllability and observability analysis," pp. 140–146, 2005.

[66] J. Brewer, Z. Huang, A. K. Singh, M. Misra, and J. Hahn, "Sensor Network Design via Observability Analysis and Principal Component Analysis," *Ind. Eng. Chem. Res.*, vol. 46, pp. 8026–8032, 2007.

[67] F. W. J. Van Den Berg, H. C. J. Hoefsloot, H. F. M. Boelens, and A. K. Smilde, "Selection of optimal sensor position in a tubular reactor using robust degree of observability criteria," *Chem. Eng. Sci.*, vol. 55, no. 4, pp. 827–837, 2000.

[68] P. C. Müller and H. I. Weber, "Analysis and Optimization of Certain Quantities of Controllability and Observability," *Automatica*, vol. 8, pp. 237–246, 1972.

[69] F. Zanini, D. Atienza, and G. De Micheli, "A combined sensor placement and convex optimization approach for thermal management in 3D-MPSoC with liquid cooling," *Integr. VLSI J.*, vol. 46, no. 1, pp. 33–43, 2013.

[70] N. A. Samad, J. B. Siegel, A. G. Stefanopoulou, and A. Knobloch, "Observability analysis for surface sensor location in encased battery cells," *Proc. Am. Control Conf.*, vol. 2015–July, pp. 299–304, 2015.

[71] J. A. Wilson and S. Y. Guhe, "Observability matrix condition number in design of measurement strategies," *Comput. Aided Chem. Eng.*, vol. 20, no. C, pp. 397–402, 2005.

[72] Y. Lei, C. Barth, S. Qin, W.-C. Liu, I. Moon, A. Stillwell, D. Chou, T. Foulkes, Z. Ye, Z. Liao, and R. Pilawa-Podgurski, "A 2 kW, Single-Phase, 7-Level Flying Capacitor Multilevel Inverter with an Active Energy Buffer," *IEEE Trans. Power Electron.*, vol. 8993, no. c, pp. 1–1, 2017.

Appendix

State space model of the 2-D dynamic thermal model

$$C_1\dot{T}_1 = \frac{T_2 - T_1}{R_{1,2}} + \frac{T_8 - T_1}{R_{1,8}} + \frac{T_{11} - T_1}{R_{1,11}} + \frac{T_{19} - T_1}{R_{1,19}} + \frac{T_{24} - T_1}{R_{1,24}} + \frac{T_{32} - T_1}{R_{1,32}} + \frac{T_{35} - T_1}{R_{1,35}} - \frac{T_1 - T_a}{R_{c1}} \tag{7.1}$$

$$C_2\dot{T}_2 = \frac{T_1 - T_2}{R_{1,2}} - \frac{T_2 - T_3}{R_{2,3}} - \frac{T_2 - T_8}{R_{2,8}} - \frac{T_2 - T_a}{R_{c2}} \tag{7.2}$$

$$C_3\dot{T}_3 = \frac{T_2 - T_3}{R_{2,3}} + \frac{T_8 - T_3}{R_{3,8}} - \frac{T_3 - T_4}{R_{3,4}} - \frac{T_3 - T_9}{R_{3,9}} - \frac{T_3 - T_{13}}{R_{3,13}} - \frac{T_3 - T_a}{R_{c3}} \tag{7.3}$$

$$C_4\dot{T}_4 = \frac{T_3 - T_4}{R_{3,4}} - \frac{T_4 - T_9}{R_{4,9}} - \frac{T_4 - T_5}{R_{4,5}} - \frac{T_4 - T_a}{R_{c4}} \tag{7.4}$$

$$C_5\dot{T}_5 = \frac{T_4 - T_5}{R_{4,5}} + \frac{T_9 - T_5}{R_{9,5}} - \frac{T_5 - T_6}{R_{5,6}} - \frac{T_5 - T_{10}}{R_{5,10}} - \frac{T_5 - T_{16}}{R_{5,16}} - \frac{T_5 - T_a}{R_{c5}} \tag{7.5}$$

$$C_6\dot{T}_6 = \frac{T_5 - T_6}{R_{5,6}} - \frac{T_6 - T_{10}}{R_{6,10}} - \frac{T_6 - T_7}{R_{6,7}} - \frac{T_6 - T_a}{R_{c6}} \tag{7.6}$$

$$C_7\dot{T}_7 = \frac{T_6 - T_7}{R_{6,7}} + \frac{T_{10} - T_7}{R_{7,10}} + \frac{T_{18} - T_7}{R_{7,18}} + \frac{T_{23} - T_7}{R_{7,23}} + \frac{T_{31} - T_7}{R_{7,31}} + \frac{T_{34} - T_7}{R_{7,34}} + \frac{T_{39} - T_7}{R_{7,39}} - \frac{T_7 - T_a}{R_{c7}} \tag{7.7}$$

$$C_8\dot{T}_8 = \frac{T_1 - T_8}{R_{1,8}} + \frac{T_2 - T_8}{R_{2,8}} - \frac{T_8 - T_3}{R_{3,8}} - \frac{T_8 - T_{11}}{R_{8,11}} - \frac{T_8 - T_{12}}{R_{8,12}} - \frac{T_8 - T_a}{R_{c8}} \tag{7.8}$$

$$C_9\dot{T}_9 = \frac{T_3 - T_9}{R_{3,9}} + \frac{T_4 - T_9}{R_{4,9}} - \frac{T_9 - T_5}{R_{9,5}} - \frac{T_9 - T_{14}}{R_{9,14}} - \frac{T_9 - T_{15}}{R_{9,15}} - \frac{T_9 - T_a}{R_{c9}} \tag{7.9}$$

$$C_{10}\dot{T}_{10} = \frac{T_5 - T_{10}}{R_{5,10}} + \frac{T_6 - T_{10}}{R_{6,10}} - \frac{T_{10} - T_7}{R_{7,10}} - \frac{T_{10} - T_{17}}{R_{10,17}} - \frac{T_{10} - T_{18}}{R_{10,18}} - \frac{T_{10} - T_a}{R_{c10}} \tag{7.10}$$

$$C_{11}\dot{T}_{11} = Q_{s1} + \frac{T_1 - T_{11}}{R_{1,11}} + \frac{T_8 - T_{11}}{R_{8,11}} - \frac{T_{11} - T_{12}}{R_{11,12}} - \frac{T_{11} - T_{19}}{R_{11,19}} - \frac{T_{11} - T_a}{R_{c11}} \tag{7.11}$$

$$C_{12}\dot{T}_{12} = Q_{s2} + \frac{T_{11} - T_{12}}{R_{11,12}} + \frac{T_8 - T_{12}}{R_{8,12}} - \frac{T_{12} - T_{13}}{R_{12,13}} - \frac{T_{12} - T_{19}}{R_{12,19}} - \frac{T_{12} - T_a}{R_{c12}} \tag{7.12}$$

$$C_{13}\dot{T}_{13} = \frac{T_{12} - T_{13}}{R_{12,13}} + \frac{T_3 - T_{13}}{R_{3,13}} - \frac{T_{13} - T_{14}}{R_{13,14}} - \frac{T_{13} - T_{20}}{R_{13,20}} - \frac{T_{13} - T_a}{R_{c,13}} \tag{7.13}$$

$$C_{14}\dot{T}_{14} = Q_{s3} + \frac{T_{13} - T_{14}}{R_{13,14}} + \frac{T_9 - T_{14}}{R_{9,14}} - \frac{T_{14} - T_{15}}{R_{14,15}} - \frac{T_{14} - T_{21}}{R_{14,21}} - \frac{T_{14} - T_a}{R_{c,14}} \tag{7.14}$$

$$C_{15}\dot{T}_{15} = Q_{s4} + \frac{T_{14} - T_{15}}{R_{14,15}} + \frac{T_9 - T_{15}}{R_{9,15}} - \frac{T_{15} - T_{16}}{R_{15,16}} - \frac{T_{15} - T_{21}}{R_{15,21}} - \frac{T_{15} - T_a}{R_{c15}} \tag{7.15}$$

$$C_{16}\dot{T}_{16} = \frac{T_5 - T_{16}}{R_{5,16}} + \frac{T_{15} - T_{16}}{R_{15,16}} - \frac{T_{16} - T_{17}}{R_{16,17}} - \frac{T_{16} - T_{22}}{R_{16,22}} - \frac{T_{16} - T_a}{R_{c16}} \tag{7.16}$$

$$C_{17}\dot{T}_{17} = Q_{s5} + \frac{T_{10} - T_{17}}{R_{10,17}} + \frac{T_{16} - T_{17}}{R_{16,17}} - \frac{T_{17} - T_{18}}{R_{17,18}} - \frac{T_{17} - T_{23}}{R_{17,23}} - \frac{T_{17} - T_a}{R_{c,17}} \tag{7.17}$$

$$C_{18}\dot{T}_{18} = Q_{s6} + \frac{T_{10} - T_{18}}{R_{10,18}} + \frac{T_{17} - T_{18}}{R_{17,18}} - \frac{T_{18} - T_7}{R_{7,18}} - \frac{T_{18} - T_{23}}{R_{18,23}} - \frac{T_{18} - T_a}{R_{c18}} \tag{7.18}$$

$$C_{19}\dot{T}_{19} = \frac{T_{11} - T_{19}}{R_{11,19}} + \frac{T_{12} - T_{19}}{R_{12,19}} + \frac{T_1 - T_{19}}{R_{1,19}} - \frac{T_{19} - T_{20}}{R_{19,20}} - \frac{T_{19} - T_{24}}{R_{19,24}} - \frac{T_{19} - T_{25}}{R_{19,25}} - \frac{T_{19} - T_a}{R_{c19}}$$

(7.19)

$$C_{20}\dot{T}_{20} = \frac{T_{13} - T_{20}}{R_{13,20}} + \frac{T_{19} - T_{20}}{R_{19,20}} - \frac{T_{20} - T_{21}}{R_{20,21}} - \frac{T_{20} - T_{26}}{R_{20,26}} - \frac{T_{20} - T_a}{R_{c20}} \tag{7.20}$$

$$C_{21}\dot{T}_{21} = \frac{T_{14}-T_{21}}{R_{14,21}} + \frac{T_{15}-T_{21}}{R_{15,21}} + \frac{T_{20}-T_{21}}{R_{20,21}} - \frac{T_{21}-T_{22}}{R_{21,22}} - \frac{T_{21}-T_{27}}{R_{21,27}} - \frac{T_{21}-T_{28}}{R_{21,28}} - \frac{T_{21}-T_a}{R_{c21}}$$

(7.21)

$$C_{22}\dot{T}_{22} = \frac{T_{16}-T_{22}}{R_{16,22}} + \frac{T_{21}-T_{22}}{R_{21,22}} - \frac{T_{22}-T_{23}}{R_{22,23}} - \frac{T_{22}-T_{29}}{R_{22,29}} - \frac{T_{22}-T_a}{R_{c22}} \tag{7.22}$$

$$C_{23}\dot{T}_{23} = \frac{T_{17}-T_{23}}{R_{17,23}} + \frac{T_{18}-T_{23}}{R_{18,23}} + \frac{T_{22}-T_{23}}{R_{22,23}} - \frac{T_{23}-T_7}{R_{7,23}} - \frac{T_{23}-T_{30}}{R_{23,30}} - \frac{T_{23}-T_{31}}{R_{23,31}} - \frac{T_{23}-T_a}{R_{c23}}$$

(7.23)

$$C_{24}\dot{T}_{24} = Q_{s7} + \frac{T_1-T_{24}}{R_{1,24}} + \frac{T_{19}-T_{24}}{R_{19,24}} - \frac{T_{24}-T_{25}}{R_{24,25}} - \frac{T_{24}-T_{32}}{R_{24,32}} - \frac{T_{24}-T_a}{R_{c24}} \tag{7.24}$$

$$C_{25}\dot{T}_{25} = Q_{s8} + \frac{T_{24}-T_{25}}{R_{24,25}} + \frac{T_{19}-T_{25}}{R_{19,25}} - \frac{T_{25}-T_{26}}{R_{25,26}} - \frac{T_{25}-T_{32}}{R_{25,32}} - \frac{T_{25}-T_a}{R_{c25}} \tag{7.25}$$

$$C_{26}\dot{T}_{26} = \frac{T_{25}-T_{26}}{R_{25,26}} + \frac{T_{20}-T_{26}}{R_{20,26}} - \frac{T_{26}-T_{27}}{R_{26,27}} - \frac{T_{26}-T_{36}}{R_{26,36}} - \frac{T_{26}-T_a}{R_{c26}} \tag{7.26}$$

$$C_{27}\dot{T}_{27} = Q_{s9} + \frac{T_{26}-T_{27}}{R_{26,27}} + \frac{T_{21}-T_{27}}{R_{21,27}} - \frac{T_{27}-T_{28}}{R_{27,28}} - \frac{T_{27}-T_{33}}{R_{27,33}} - \frac{T_{27}-T_a}{R_{c27}} \tag{7.27}$$

$$C_{28}\dot{T}_{28} = Q_{s10} + \frac{T_{27}-T_{28}}{R_{27,28}} + \frac{T_{21}-T_{28}}{R_{21,28}} - \frac{T_{28}-T_{29}}{R_{28,29}} - \frac{T_{28}-T_{33}}{R_{28,33}} - \frac{T_{28}-T_a}{R_{c28}} \tag{7.28}$$

$$C_{29}\dot{T}_{29} = \frac{T_{22}-T_{29}}{R_{22,29}} + \frac{T_{28}-T_{29}}{R_{28,29}} - \frac{T_{29}-T_{30}}{R_{29,30}} - \frac{T_{29}-T_{38}}{R_{29,38}} - \frac{T_{29}-T_a}{R_{c29}} \tag{7.29}$$

$$C_{30}\dot{T}_{30} = Q_{s11} + \frac{T_{29}-T_{30}}{R_{29,30}} + \frac{T_{23}-T_{30}}{R_{23,30}} - \frac{T_{30}-T_{31}}{R_{30,31}} - \frac{T_{30}-T_{34}}{R_{30,34}} - \frac{T_{30}-T_a}{R_{c30}} \tag{7.30}$$

$$C_{31}\dot{T}_{31} = Q_{s12} + \frac{T_{30}-T_{31}}{R_{30,31}} + \frac{T_{23}-T_{31}}{R_{23,31}} - \frac{T_{31}-T_7}{R_{7,31}} - \frac{T_{31}-T_{34}}{R_{31,34}} - \frac{T_{31}-T_a}{R_{c31}} \tag{7.31}$$

$$C_{32}\dot{T}_{32} = \frac{T_{24}-T_{32}}{R_{24,32}} + \frac{T_{25}-T_{32}}{R_{25,32}} + \frac{T_1-T_{32}}{R_{1,32}} - \frac{T_{32}-T_{36}}{R_{32,36}} - \frac{T_{32}-T_{35}}{R_{32,35}} - \frac{T_{32}-T_a}{R_{c32}} \tag{7.32}$$

$$C_{33}\dot{T}_{33} = \frac{T_{27}-T_{33}}{R_{27,33}} + \frac{T_{28}-T_{33}}{R_{28,33}} + \frac{T_{36}-T_{33}}{R_{33,36}} - \frac{T_{33}-T_{38}}{R_{33,38}} - \frac{T_{33}-T_{37}}{R_{33,37}} - \frac{T_{33}-T_a}{R_{c33}} \quad (7.33)$$

$$C_{34}\dot{T}_{34} = \frac{T_{30}-T_{34}}{R_{30,34}} + \frac{T_{31}-T_{34}}{R_{31,34}} + \frac{T_{38}-T_{34}}{R_{38,34}} - \frac{T_{34}-T_7}{R_{7,34}} - \frac{T_{34}-T_{39}}{R_{34,39}} - \frac{T_{34}-T_a}{R_{c34}} \quad (7.34)$$

$$C_{35}\dot{T}_{35} = \frac{T_{32}-T_{35}}{R_{32,35}} + \frac{T_1-T_{35}}{R_{1,35}} - \frac{T_{35}-T_{36}}{R_{35,36}} - \frac{T_{35}-T_a}{R_{c35}} \quad (7.35)$$

$$C_{36}\dot{T}_{36} = \frac{T_{32}-T_{36}}{R_{32,36}} + \frac{T_{35}-T_{36}}{R_{35,36}} + \frac{T_{26}-T_{36}}{R_{26,36}} - \frac{T_{36}-T_{33}}{R_{33,36}} - \frac{T_{36}-T_{37}}{R_{36,37}} - \frac{T_{36}-T_a}{R_{c36}} \quad (7.36)$$

$$C_{37}\dot{T}_{37} = \frac{T_{33}-T_{37}}{R_{33,37}} + \frac{T_{36}-T_{37}}{R_{36,37}} - \frac{T_{37}-T_{38}}{R_{37,38}} - \frac{T_{37}-T_a}{R_{c37}} \quad (7.37)$$

$$C_{38}\dot{T}_{38} = \frac{T_{33}-T_{38}}{R_{33,38}} + \frac{T_{37}-T_{38}}{R_{37,38}} + \frac{T_{29}-T_{38}}{R_{29,38}} - \frac{T_{38}-T_{34}}{R_{34,38}} - \frac{T_{38}-T_{39}}{R_{38,39}} - \frac{T_{38}-T_a}{R_{c38}} \quad (7.38)$$

$$C_{39}\dot{T}_{39} = \frac{T_{34}-T_{39}}{R_{34,39}} + \frac{T_{38}-T_{39}}{R_{38,39}} - \frac{T_{39}-T_7}{R_{7,39}} - \frac{T_{39}-T_a}{R_{c39}} \quad (7.39)$$